MECHANICAL BEHAVIOR OF A SILICONE ELASTOMER, ELASTOMER COMPOSITES, AND A NATURAL COMPOSITE

A Dissertation

by

SEUNGHYUN LEE

Submitted to the Office of Graduate and Professional Studies of
Texas A&M University
in partial fulfillment of the requirements for the degree of

DOCTOR OF PHILOSOPHY

Chair of Committee,	Matt Pharr
Committee Members,	Hong Liang
	Terry Creasy
	Bruce Tai
Head of Department,	Andreas A. Polycarpou

May 2020

Major Subject: Mechanical Engineering

ABSTRACT

This dissertation studies mechanical behavior, damage, and fracture of a silicone elastomer, elastomer composites, and a natural composite (bioenergy sweet sorghum). First, we identify and investigate a peculiar form of fracture that occurs in a highly stretchable silicone elastomer. We find that under certain conditions, cracks propagate in a direction perpendicular to the initial precut and in the direction of the applied load. Due to the crack tip deflection, the material ahead of the crack front continues to sustain load, thereby enabling enormous stretchabilities.

This dissertation then investigates fracture behavior in a new type of elastomer composite. Unlike in standard reinforced composite systems, we dispersed voids into a silicone elastomer matrix. One design implements interconnected rectangular prisms of voids and another incorporates randomly distributed spherical voids. This work demonstrates that the void-embedded silicone elastomer provides increased rupture resistance, flaw tolerance, and stretchability, while simultaneously decreasing the overall weight.

We also conduct finite element analysis (FEA) of flexible and stretchable electronics that have complex composite structures. First, we perform FEA simulations of stretchable ultrasound sensor arrays. This simulation provides stress distributions of these devices under biaxial tension and provides insights into limitations in terms of stretchability. Next we perform simulations of flexible photovoltaic devices to design optimal thicknesses of the composite, as to maximize its flexibility. Finally, we study a

topic in optoelectronics aimed at controlling the activity of subsets of neurons and nerve fibers in vivo. These three simulations provide visualized stress distribution of complex composite structures and their limitations in terms of stretchabilities and flexibilities.

Finally, this dissertation investigates the mechanical response of a natural composite: a bioenergy crop (Sorghum bicolor (L.) Moench). The goal is to determine whether time-dependent effects are prevalent in this material, and if so, to provide insight into potential ramifications in terms of structural stability during growth. To do so, we implemented experimental measurements of time/rate dependency of piths and stems of sorghum under compression. These measurements demonstrate that sorghum is not a simple reversible elastic material and provide fundamental information to understand structural failure and mechanical stability of grass stems.

Mechanical and fracture behaviors of elastomers, elastomer composites, and natural composites are complex and often even unintuitive due to their unique properties stemming from their complicated micro- and macro-scale geometries. This dissertation provides experimental data and FEA simulations that offer fundamental insight into mechanical and fracture behavior of elastomers, elastomer composites, and natural composites.

ACKNOWLEDGEMENTS

I would like to thank my committee chair, Dr. Pharr, and my committee members, Dr. Liang, Dr. Tai, and Dr. Creasy, for their guidance and support throughout the course of this research.

Thanks also go to my friends and colleagues and the department faculty and staff for making my time at Texas A&M University a great experience.

Finally, thanks to my mother and father for their encouragement and unconditional support.

CONTRIBUTORS AND FUNDING SOURCES

Contributors

This work was supervised by a dissertation committee consisting of Professor Matt Pharr, Professor Hong Liang, and Professor Bruce Tai of the Department of Mechanical Engineering and Professor Terry Creasy of the Department of Material Science and Engineering.

The experiments for Chapter 3 were performed in part by Russell Rowe of the Department of Mechanical Engineering at Lamar University, Cole Fincher, Arber Shasivari, and Edwin Torres of the Department of Mechanical Engineering at Texas A&M University, and Michael Ecker-Randolph of the Department of Mechanical and Aerospace Engineering at West Virginia University. The experiments results and its data analysis for Chapter 4 in Section 4.1 were provided by Dr. Sheng Xu and his research group of the Materials Science and Engineering Program at University of California San Diego and were published in 2018. The experiments and data analysis were conducted for Chapter 4 in Section 4.2 by Dr. Salvatore and his research group of Electronics Laboratory at ETH Zurich and were published in 2019. Mechanical testing and data analysis for Chapter 4 in Section 4.3 were provided by Dr. Sheng Xu and his research group of the Materials Science and Engineering Program at University of California San Diego. Experiments in Chapter 5 were performed in part by Omid Zargar and Carl Reiser of the Department of Mechanical Engineering at Texas A&M University, and the data was analyzed in part by Dr. Anastasia Muliana of Department of Mechanical Engineering at Texas A&M University, Dr. Scott A. Finlayson of the Department of Soil

and Crop Science at Texas A&M University, and Francisco E. Gomez of the Department of Agronomy and Pant Genetics at University of Minnesota. All other work conducted for the dissertation was completed by the student independently.

Funding Sources

The graduate study was supported by funding from the Department of Mechanical Engineering at Texas A&M University and the Texas A&M Engineering Experiment Station.

TABLE OF CONTENTS

Page

LIST OF FIGURES

Page

LIST OF TABLES

Page

1. INTRODUCTION

This dissertation investigates the mechanical and fracture behavior of soft materials: specifically a silicone elastomer, elastomer composites, and a natural composite (sweet sorghum). Soft materials are a class of materials that includes polymers, gels, liquid crystals, and biological tissues. Soft materials are compliant and highly deformable before failure, largely due to weak intermolecular forces, e.g., between polymer chains. These features lead to complex and interesting mechanical properties, including pronounced viscoelasticity, strain-induced crystallization, and large crack tip blunting before crack propagation, which distinguishes them from traditional hard materials (e.g., metals and ceramics). To understand mechanics of soft materials and their composites, it is critical to investigate microstructure-property relationships and interactions between hard and soft materials in composite systems. The remainder of this chapter provides an introduction to elastomer fracture, the mechanical behavior of elastomer composites (including stretchable and flexible electronics), and the mechanical behavior of a natural composite – bioenergy feedstock sorghum.

1.1. Fracture behavior of silicone elastomers

Polymers and polymer composites are replacing the roles of traditional engineering materials (e.g., metals) in many applications due to their relatively low cost, easy fabrication methods, corrosion resistance, stretchability, and readily tunable chemistries. Through chemical modifications and clever design of composite structures, polymers can display high strengths while still being lightweight and relatively compliant and stretchable. Specifically, elastomers have relatively low elastic moduli high failure strain due to their low cross-link densities and weak intermolecular forces among chains. As a result, elastomers often exhibit large reversible deformation prior to material failure. Moreover, elastomers can display intriguing mechanical behavior such as hyperelasticity, strain-induced crystallization, and different material failure mechanisms compared to conventional structured material such as metals.

Indeed, theories and experimental characterization of fracture mechanisms in elastomers are not nearly as well-developed as in traditional engineering materials (metals and ceramics) due to the complicated microstructural configurations and resulting properties of elastomers. For instance, under certain conditions in carbon-black filled rubber, researchers have observed that the cracks deviated from the 'standard' direction by either curving or bifurcating into two cracks. However, upon further loading, a new crack emanated from this region, again in the 'standard' direction. This behavior is often referred to as 'stick-slip' or 'knotty' tearing (1, 2). This behavior has also been observed (including observations by us as shown in Figure 1.1) in other types of elastomer such as ethylene propylene diene monomer (EPDM) rubber.

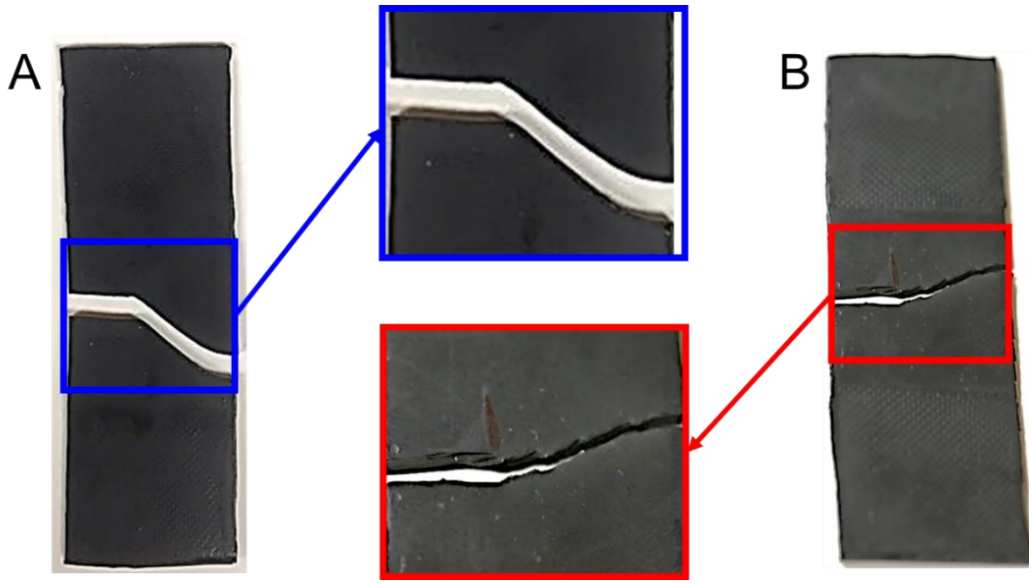

Figure 1.1 Fatigue crack path in EPDM rubber under cyclic tensile loading. (A) Amorphous EPDM. (B) Semi-crystalline EPDM.

As motivation for one part of this thesis, Figure 1.1 shows crack propagation patterns of EPDM rubber. The materials in Figure 1.1A and B are amorphous and semi-crystalline EPDM rubber, respectively. The amorphous structure consists of randomly entangled polymer chains, which can become aligned in the direction parallel to applied load. Combined with chain rearrangement and filler effects (we surmise), the crack tip deflects from the initial flaw but produces a comparatively smooth surface (blue box in Figure 1.1A). By comparison, the semi-crystalline EPDM shows a more stochastic crack pattern (red box in Figure 1.1B). In general, interfacial bonding between the filler particles and matrix and the shape and the distribution of the particles (among other factors) can affect the mechanical behavior and fracture mechanism of a particulate-reinforced composite system (3). This result demonstrates that polymer

microstructure/constitution can be one of the dominant factors in determining the fracture behavior of elastomers.

With this motivation in mind, Chapter 2 of this thesis investigates fracture behavior of a highly stretchable silicone elastomer (Ecoflex 00-30). This silicone elastomer is widely used in many research area due to its stretchability, flexibility, and biocompatibility, particularly in the field of stretchable/flexible/wearable electronics. In this material, we have observed a remarkable form of crack propagation. Under certain conditions, upon loading Ecoflex in the direction perpendicular to an initial crack, the crack propagates in the direction of the applied load. In other words, the crack propagates in a direction 90° relative to the direction that we would normally expect. We name this phenomenon "sideways crack propagation" (Figure 1.2). Unlike cracking in carbon black-filled or EPDM rubber, this material shows stable crack propagation without any bifurcation for stochastic patterns.

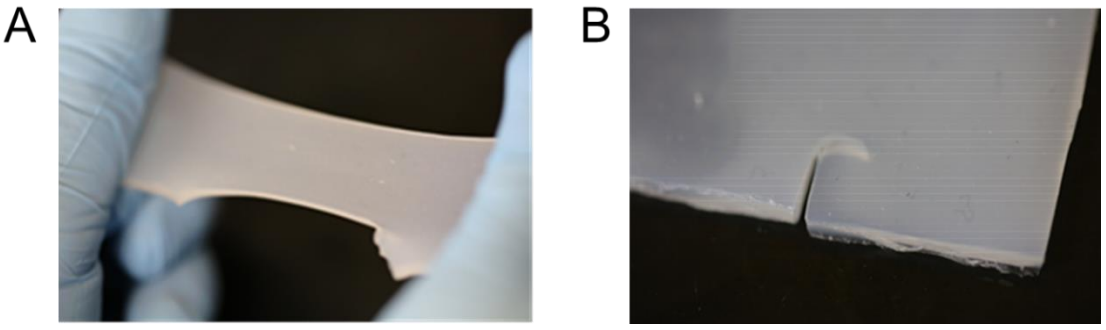

Figure 1.2 Photos of sideways crack propagation from a pre-cut specimen. (A) During uniaxial stretching, a crack propagates in the direction of the applied load. (B) Image of the crack after unloading, showing the stable propagation of a sideways crack.

Beyond being scientifically intriguing, this feature of fracture also suggests the new possibility of increasing the rupture resistance of elastomers by guiding the crack propagation path. In Chapter 2, we investigate sideways and stable crack propagation in this silicone elastomer. Crack tip blunting and microstructural effects are studied to provide insight into the crack tip deflection mechanism. In Chapter 3, we fabricate and investigate a new types of elastomer composite, which consists of voids embedded into elastomers. Different types of voids and different elastomer-void volume ratio are considered to understand how cracks interact with these voids and ultimately lead to different macroscopic fracture properties.

1.2. Mechanical behavior of flexible and stretchable electronics

Flexible and stretchable electronic devices have widespread applications such as surgical tools, rollable touch displays, biomonitoring, electronic skins, structural health monitors, wearable communication devices, and paper-like displays (4-14). Flexible electronic devices consist of thin film material layers because even stiff materials become flexible upon reducing their thickness. As such, flexible devices maintain their functional performance and reliability only under bending deformation. However, applications such as skin-mountable devices and bio-integrated electronics (15-17) require large stretchability, flexibility, durability, and biocompatibility due to their exposure to repeated stretching, bending, and twisting. For this reason, elastomers are commonly selected as substrates and encapsulations in device applications. Both flexible and stretchable devices integrate hard components (e.g., conductive interconnects and

circuits) and soft components (e.g., substrates and encapsulation materials). To enable overall stretchability of these systems, the rigid circuits or sensors are often arranged in an island-format, and these islands are interconnected by wavy or serpentine shaped thin conductive materials. This types of devices consists of multiple layers, complex geometries, and significant variations in mechanical properties (e.g., from soft substrates to rigid chips) and thus require careful mechanical analysis. Indeed, to provide insight into designs and conditions that enable functionality and reliability of stretchable devices, finite element analysis (FEA) is often necessary. In Chapter 4, we have provided insight into appropriate design for reliable mechanical performance of three different types of flexible and stretchable devices: flexible photovoltaics, flexible optoelectronics, and stretchable ultrasound sensor arrays using the commercial FEA software ABAQUS. These simulations provide stress and strain distribution of devices and predict limitations of the mechanical performances of devices during operation.

1.3. Biomechanical properties of bioenergy sorghum

Plant biomechanics is an emerging research area aimed at examining the effects of mechanical forces in biological system. As one interesting example, mechanical forces during growth have been shown to affect the growth morphology of plants. Furthermore, many plants are susceptible to mechanical/structural failure during growth. As such, multiscale mechanical testing from the micro scale level (e.g. cell walls, fibrils, and macromolecule) to the macroscale (e.g., stems) have been performed for phenotyping and crop improvement. Overall, plants biomechanics have provided

fundamental information not only of botany but also of physical structure and mechanical behavior of living beings from a mechanics of materials perspective.

Sorghum (sorghum bicolor (L.) Moench) is a widely grown cereal crop, which key use a sustainable food source, particularly for animal feeding, and has found other uses such as in paper and as a bioenergy feedstock (18, 19). Indeed, its huge diversity in terms of genetics, phenotypes, and morphologies make sorghum a nice candidate as a biofuel feedstock. Sorghum bicolor can be divided into four groups: grain sorghum, forage sorghum, energy sorghum, and sweet sorghum. Among these groups, sweet sorghum have emerged as perhaps the most promising feedstock for biofuel due to the large number of cultivars (more than 4000), high sugar content, and ease of juice extraction compared to other groups of sorghum (20). Like all cereal corps, however, sweet sorghum often experiences mechanical failure due to wind pressure on the stem during growth. Stem lodging frequently occurs at the internode of the stem, and it brings significant loss of yield in large-scale planting. A strategy to decrease stem lodging is to design lodging-resistant varieties, which requires a full understanding of the mechanical properties of stalks and the identification of genes responsible for superior mechanical properties. To understand the lodging mechanism and preventing lodging in the field, quantitative methods including bending, axial tension and compression have been applied (21-23). However, all measurements have been performed only in the elastic region, which is insufficient to understand stem mechanical behavior, particularly during stem failure via lodging, which intrinsically involves large deformation. Failure in living stems likely depends not only on the magnitude of loading but also on the rate and

duration of loading due to viscoelastic effects. As a result, fully characterizing biomechanical properties of sorghum stems and understanding the failure mechanisms of sorghum stems are key areas of research to mitigate lodging and increase yield.

To this end, the biomechanical behavior of sorghum, focusing on time-dependent behavior of the stems, is investigated in Chapter 5. Linear ramp tests with different strain rate and creep tests under axial compression were performed to determine whether sorghum piths and stems exhibit rate/time-dependent effects and to characterize their full (beyond the linear regime) biomechanical responses. Measuring viscoelastic and time-dependent properties provides important information for future research such as modeling studies (e.g., of lodging) and designing bio-inspired structures.

2. ‘SIDEWAYS’ AND STABLE CRACK PROPAGATION IN A SILICONE ELASTOMER*

2.1. Introduction

Soft materials are vital in flexible electronics, soft robotics, drug delivery, microfluidics, bioengineering, and adaptive optics, among others (4, 6, 10, 24-32). Applications in these areas often require large stretchability, flexibility, and toughness due to repeated stretching, bending, and twisting during operation. As such, elastomers have emerged as a material class of choice in these areas due to their low cost, large stretchabilities, and chemical tuneabilities. In particular, chemical modifications have enabled certain classes of elastomers to stretch from hundreds to thousands of percent prior to fracture (33-36). Owing to their large stretchabilities, fracture of elastomers largely differs from other material classes. For instance, elastomers often exhibit crack-tip blunting and/or rate-dependent fracture toughnesses (37-40). Likewise, the fracture toughness of elastomers highly depends on the size of initial flaws (41), and the initial crack tip sharpness (42). Moreover, cracks in elastomers sometimes deviate from ‘standard’ paths, particularly in the initial stages of their growth (43). For instance, Hamed and Park (44) studied fracture of carbon-black-filled natural rubber. Near the tip of an edge crack, they observed small auxiliary cracks that initially turned in somewhat stochastic directions (including some perpendicular relative to the initial edge crack)

*Reprinted with permission from “Sideways and stable crack propagation in a silicone elastomer” by Seunghyun Lee and Matt Pharr, 2019. *Proceeding of the National Academy of Science of the United States of America*, Vol. 116, no. 19, 9251-9256, Copyright 2019 by Seunghyun Lee and Matt Pharr.

before eventually turning back to the 'standard' direction across the specimen (i.e., back to the direction of the edge crack). Additionally, Greensmith (2) studied carbon-black-filled compounds and found that under certain conditions, the cracks deviated from the 'standard' direction by either curving or bifurcating into two cracks. However, upon further loading, a new crack emanated from this region, again in the 'standard' direction. This behavior is often referred to as 'stick-slip' or 'knotty' tearing (1, 2). Overall, experimental observations suggest that fracture is fundamentally different in elastomers as compared to other materials, thus compelling further studies aimed at providing basic understanding of their fracture.

To this end, this chapter investigates fracture of a highly stretchable silicone elastomer (Smooth-On Ecoflex 00-30). Despite this specific elastomer's use in various research fields (particularly that of flexible/stretchable electronics) (45-50), its fracture characteristics and basic polymer properties have not been systematically studied. In section 2.2, we have discussed experimental observation and implication of sideways cracking. During fracture testing, we find an intriguing phenomenon: under certain conditions, cracks propagate in a direction perpendicular to the initial pre-cut and in the direction of the applied load. In other words, the crack deviates from the standard trajectory and instead propagates in a direction perpendicular to that trajectory. We call this phenomenon 'sideways' and stable cracking. Compared to previous studies from literature, the behavior we have observed does not occur intermittently (e.g., as in the case of bifurcation, 'stick-slip, or 'knotty tearing' (1, 2, 51, 52)) or solely in the initial stages of fracture (as in the Hamed and Park study (44)); instead, sideways crack growth

is fully stable in the elastomer described herein. The length of the sideways crack slowly increases with increasing load, and the crack arrests if the loading stops. The crack never turns back to the ‘standard’ direction or shows any bifurcation. Thus, as a practical ramification of this behavior, the material ahead of the crack front continues to sustain load, thereby enabling enormous stretchabilities. To explain this phenomenon, we perform finite element simulations that demonstrate the propensity for sideways cracking, which highlight the importance of crack-tip blunting in section 2.3. Section 2.4 includes a hypothesis on the origin of sideways cracking related to microstructural anisotropy that develops during stretching (in a nominally isotropic elastomer). To substantiate this hypothesis, we transversely pre-stretch samples to various extents prior to fracture testing to determine the influence of microstructural arrangement (chain alignment and strain-induced crystallization) on fracture energy. We also perform microstructural characterization that indicates that significant chain alignment and strain-induced crystallization occur in this material upon stretching. Section 2.5 shows effect of loading conditions such as sample geometry and loading rate to this phenomenon.

2.2. Description and implications of sideways cracking (experimental observations)

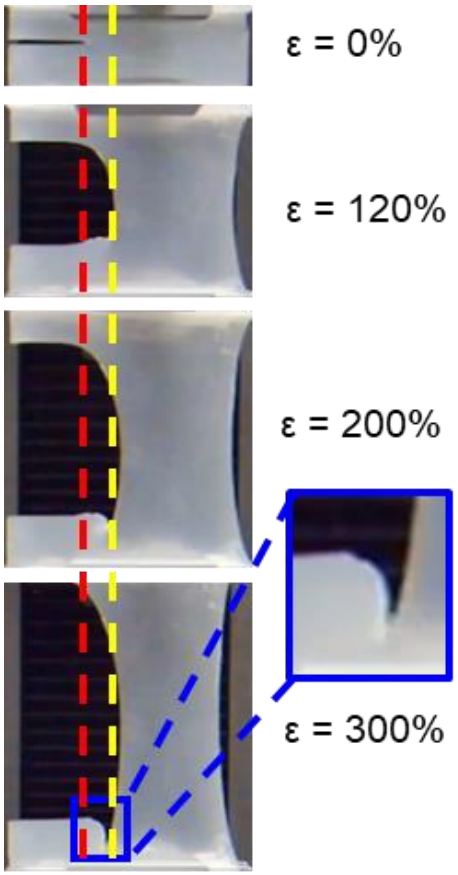

Figure 2.1 Photos of crack propagation in a silicone elastomer (Ecoflex 00-30) that demonstrates 'sideways cracking.' The specimen is pre-cut in the horizontal direction and subjected to a load in the vertical direction. During stretching, 'sideways cracking' occurs: the crack turns perpendicular to the standard (horizontal) direction. This 'sideways crack' is stable and the specimen continues to sustain load, reaching large strains prior to failure (>>300%). The red dashed line shows the initial position of the pre-cut, and the yellow dashed line shows the position of the stable sideways propagation. The blue boxed region shows a zoomed-in view of the crack tip.

We have discovered that a peculiar form of fracture occurs in particular silicone elastomers. This fracture is fundamentally distinct from typically found in other materials such as ceramics, metals, brittle polymers, and even other commonly used

elastomers. Specifically, under certain conditions, cracks propagate in a direction perpendicular to the initial pre-cut and in the direction of the applied load. The length of the sideways crack slowly increases with increasing load, and the crack arrests if the loading stops. The crack never turns back to the 'standard' direction or shows any bifurcation. Figure 2.1 shows snapshots of this phenomenon in the silicone elastomer studied herein (Smooth-On Ecoflex 00-30); we call this phenomenon 'sideways' and stable cracking (43, 53, 54).

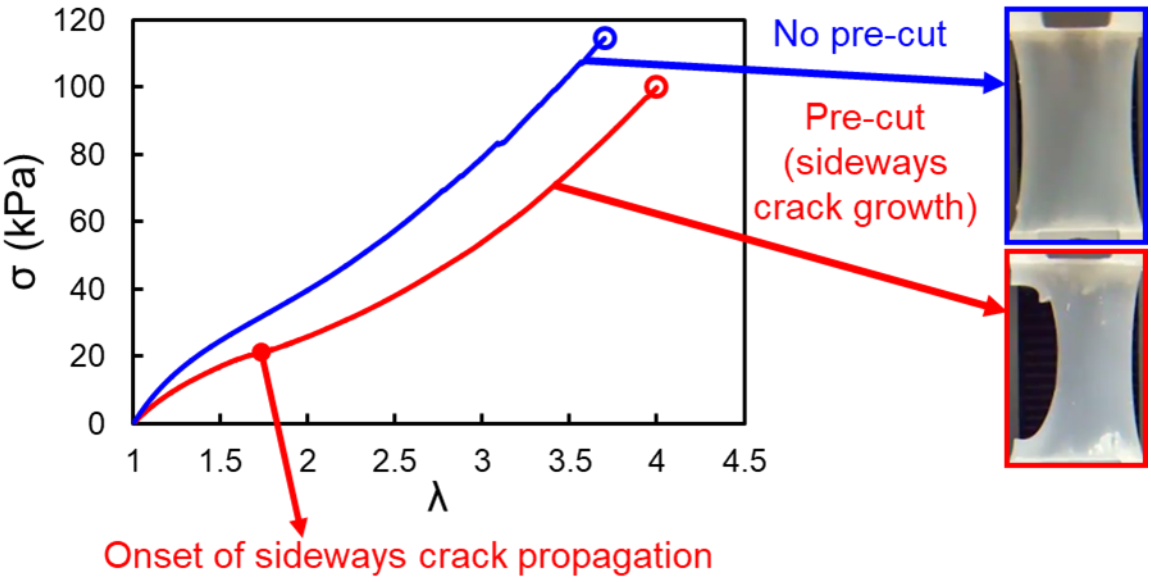

Figure 2.2 Stress-stretch curves of a silicone elastomer and corresponding fracture morphologies (thickness B = 5 mm, stretch-rate $\dot{\lambda}$ = 0.1/min).

Beyond being scientifically intriguing, these results have important ramifications from a practical perspective. Specifically, since the sideways cracks stably arrest, the un-cracked region of the material ahead of the crack front can continue to sustain load,

thereby enabling significantly larger stretchabilities. Figure 2.2 illustrates this point; despite the relatively early onset of sideways crack propagation in a pre-cut specimen (red curve at around $\lambda = 1.7$), the specimen continues to sustain loads to much larger stretches, in a manner reflective of a pristine specimen (with no pre-cut, blue curve). In fact, if the stresses in Figure 2.2 are re-plotted to account only for un-cracked areas (i.e., that of the region ahead of the crack), the red and blue curves are virtually identical. Furthermore, the un-cracked region ahead of the crack tip completely recovers after a cycle of loading/unloading, i.e., deformation continues to be elastic ahead of the crack tip (Figure 2.3).

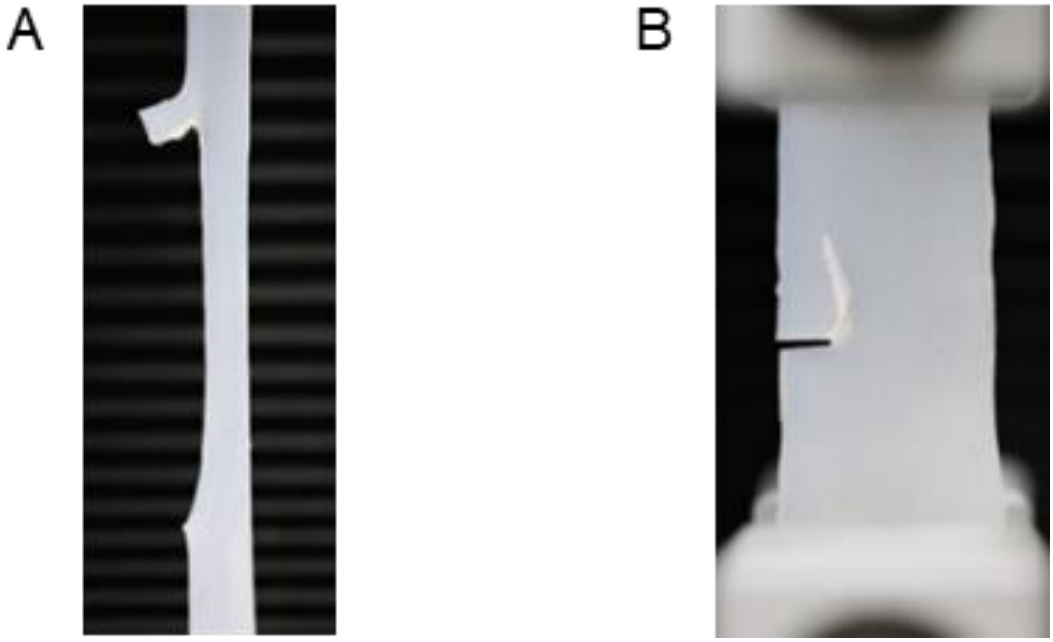

Figure 2.3 Photos of sideways crack propagation from a pre-cut specimen. (A) During uniaxial stretching (in the vertical direction), a crack propagates in the direction of the applied load. (B) An image of the crack after unloading, showing the stable propagation of a sideways crack.

2.3. Mechanics analysis of the origin of sideways cracking

The phenomenon of sideways crack growth is likely unintuitive. In particular, in most fracture mechanics analysis, a large stress concentration exists at the crack tip that drives the crack in the forward (standard) direction. However, elastomers are quite compliant and stretchable; as a result, crack-tip blunting readily occurs. Blunting reduces the stress concentration at the crack tip; correspondingly, fundamentally different fracture behavior can occur in these systems. Furthermore, crack-tip blunting in elastomers usually does not involve highly irreversible deformation and thus does not dissipate much energy in and of itself. Instead, the main mechanism for dissipating energy is through releasing elastic strain energy during crack propagation. With these effects in mind, we aim to provide a general explanation of the mechanics that can lead to sideways crack propagation.

To do so, we employed 3-dimensional finite element analysis (FEA) simulations of fracture in these systems. Specifically, we used the commercial software ABAQUS to subject a silicone elastomer with a pre-cut to a fixed level of stretch, from which the stored elastic energy, U, was computed. An 8-node linear brick, hybrid (C3D8H) was applied as the element type, and non-linear geometric effects were included to allow for finite deformation. The simulations implemented a Mooney-Rivlin constitutive model to represent a highly stretchable hyperelastic material (49). We also performed a separate analysis that implemented a linear elastic constitutive model and found similar results (both qualitatively and quantitatively) to those detailed below. Thus, the particular form of the constitutive model does not seem to affect our results. The initial crack size is c0,

and we extended a crack in steps of $\Delta c = c_0/40$ during each step. A uniform grid of elements was employed in all directions, and the size of the grid is equal to one step of the crack growth size, Δc. The energy release rate was calculated by computing the strain energy at each step of crack growth and using the relationship: $G = - \partial U/\partial A = (U_i - U_{i-1}) / (A_i - A_{i-1})$, where the U_i represent the internal energies when a crack is a certain length (at step i), and the A_i represent the area of the cracked region at the same step, i.e., the quantity $(A_i - A_{i-1})$ represents the area swept out by the crack during step i (55). To analyze the effect of blunting on the propensity for crack propagation, simulations were performed at different stretch levels: $\lambda = 1.1$ to represent a relatively sharp crack-tip and $\lambda = 2$ to represent a blunted crack tip. $\lambda = 2$ also corresponds to a strain level representative of crack initiation in our pre-cut silicone elastomer samples (see Figure 2.2). From the computed strain energy at each step, we calculate the energy release rate when the crack grows in the sideways direction, G_s, and when the crack grows in the forward direction, G_f. Figure 2.4 shows the simulations to compute the crack driving force in the forward and sideways directions at $\lambda = 2$ as a function of the newly created crack length, dc. At small crack lengths (corresponding to crack initiation), the crack driving force in the sideways direction, G_s, is around 50% that of crack driving force in the forward direction, G_f. This result suggests that the crack driving force in the forward direction is indeed larger than that in the sideways direction, as one might intuitively expect. However, the relative value of the energy release rate associated with forward cracking is not orders of magnitude larger than that of sideways cracking.

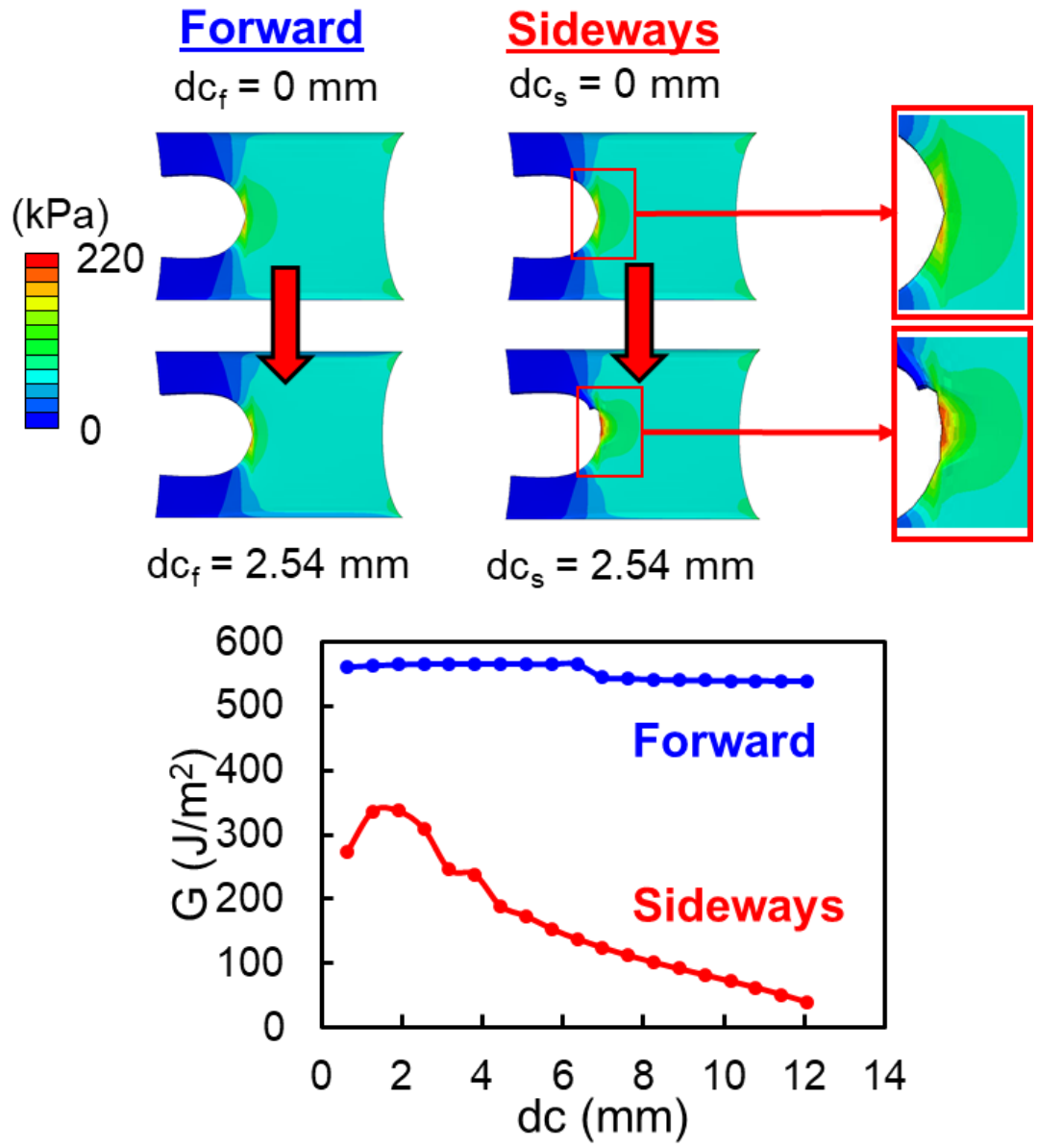

Figure 2.4 Finite element simulations comparing energy release rates for forward and sideways cracking. Top: Finite element simulations of the maximum principal stress distribution in a silicone elastomer with a pre-cut at λ = 2.0 for a crack that has propagated by dc = 0 and dc = c_0/10 (2.54 mm) in the forward direction (left images) and the sideways direction (right images). Bottom: Energy release rate, G, for forward crack growth and sideways crack growth as a function of the length of newly created crack, dc.

Correspondingly, if the resistance to crack propagation (i.e., the fracture energy) in the sideways direction is lower than ~50% of resistance to crack propagation in the forward direction, then a sideways crack should form. In short, it is not unreasonable to expect that sideways crack propagation could occur.

Additionally, Figure 2.5 shows the effect of crack-tip blunting on the propensity for sideways cracking. G_s/G_f for largely blunted specimens ($\lambda = 2$) is around 48% when c_s/c_f is small, and increases up to 60%, before eventually decreasing again. By comparison, the largely un-blunted specimen ($\lambda = 1.1$) shows smaller relative values of G_s/G_f. These results suggest that a sharp crack (e.g., in a material with low stretchability) requires a higher degree of anisotropy of the fracture energy to induce sideways crack propagation.

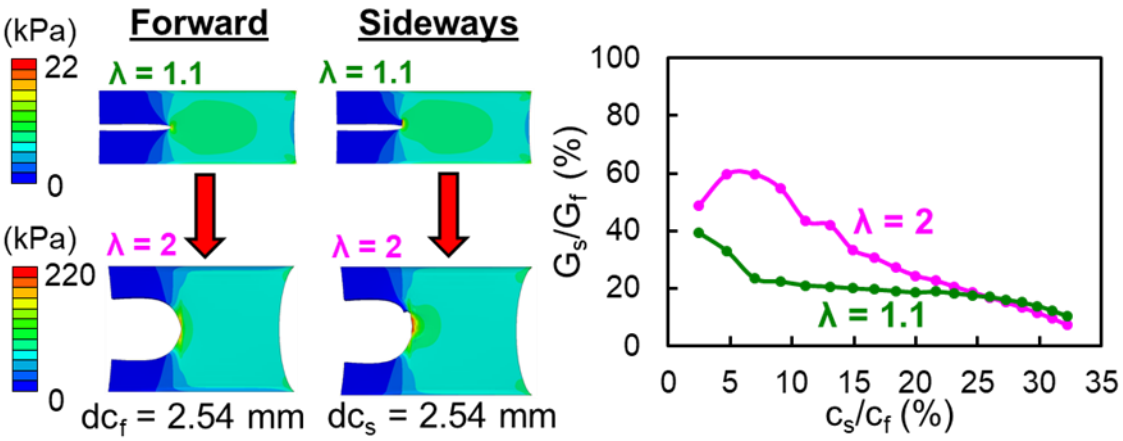

Figure 2.5 Finite element simulations showing the effects of crack tip blunting. Left: Finite element simulations of the maximum principal stress distribution in a silicone elastomer with a pre-cut at $\lambda = 1.1$ (top) and $\lambda = 2.0$ (bottom) for a crack that has propagated by $dc = c_0/10$ (2.54 mm) in the forward direction (left images) and the sideways direction (right images). Right: Energy release rate for sideways crack growth relative to that of forward crack growth as a function of the ratio of the sideways crack length c_s to the forward crack length c_f.

2.4. Anisotropic fracture energy in a nominally isotropic silicone elastomer

The finite element simulations suggest that only a mild degree of anisotropy of fracture energy is required to induce sideways cracking. To this end, we performed experiments to determine if the fracture energy of this silicone elastomer is indeed anisotropic. At first glance, it may not be obvious why its fracture energy should be anisotropic. Namely, fabrication involves a seemingly random process (with no preferred orientation) so we expect that polymer chains orient randomly, which should lead to isotropic mechanical properties. However, upon stretching of elastomers, their chains often align and can even form crystalline structures (so-called strain-induced crystallization) in the direction of stretching (Figure 2.6) (56, 57). We hypothesize that a crack aligned and propagating in a direction perpendicular to the alignment of polymer chains or crystalized domains (e.g., Figure 2.6B) has a higher resistance to propagation; simply, it would have to break more chains/domains per unit length of propagation. Correspondingly, we hypothesize that the resistance to fracture in directions parallel to the alignment (e.g., propagation of a crack between aligned chains, as in Figure 2.6C) is relatively low, e.g., consider a crack propagating horizontally in Figure 2.6B as compared to one propagating vertically in Figure 2.6C. If this were indeed the case, it would generally explain the phenomenon of sideways cracking.

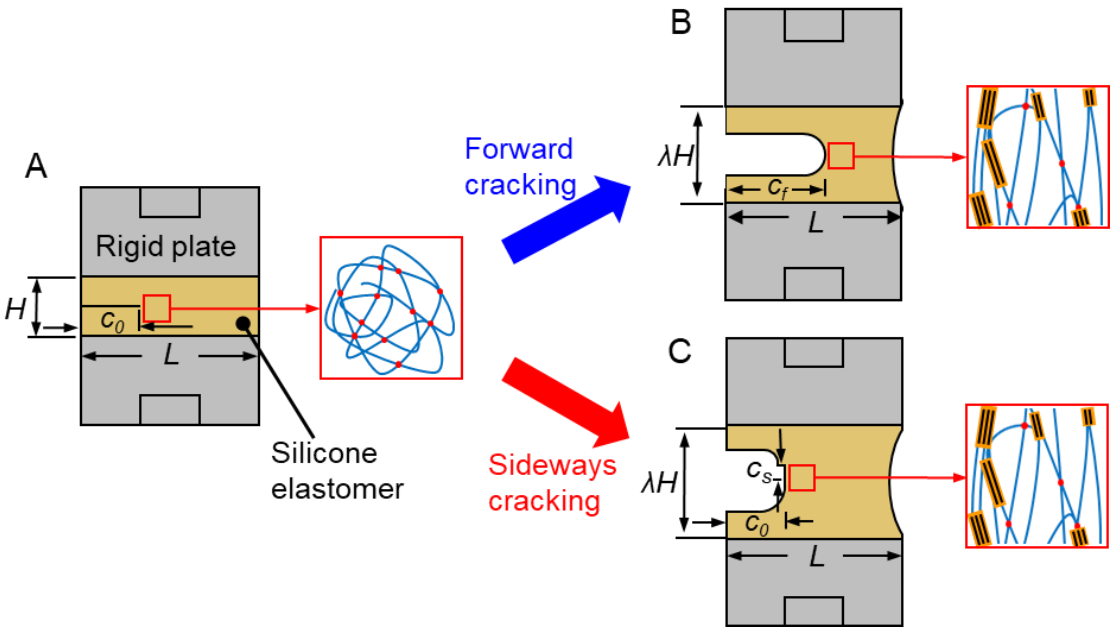

Figure 2.6 Schematics, including hypothesized microstructures, of a silicone elastomer under a pure-shear test geometry. In the microstructural schematics, the red dots denote crosslinks, and the orange boxed regions represent crystalline domains. (A) Initial configuration of a sample with a pre-cut of length c_0 (25.4 mm). (B) Sample when the crack propagates in the forward direction. c_f is the crack length in the forward direction (which includes c_0). (C) Sample when the crack propagates in the sideways direction. c_S is the newly created crack length in the sideways direction.

To this end, we performed comparative experiments of samples that were pre-stretched in the direction of the pre-cut. Figure 2.7 shows the experimental setup for these tests. Samples and loading conditions (thin samples at high strain rates; see details in Section 2.4) were implemented that only induced forward crack propagation to allow a fair comparison of the fracture energies. In these experiments, we applied different pre-stretch levels to control the degree and direction of anisotropy (due to chain alignment and/or strain-induced crystallization), Figure 2.7. We expect that pre-stretching the specimen in the direction of the pre-cut will align the polymer chains in that direction

(Figure 2.7D). As a result, when a crack in this specimen advances forward a unit length, it will break fewer polymer chains/domains as compared to a specimen that is not pre-stretched, e.g., compare Figure 2.7E to 2.7C. Correspondingly, we expect that the pre-stretched specimen will exhibit a lower value of fracture energy for forward cracking. Figure 2.7A shows the results of tests performed at three different levels of pre-stretch, λ_p. Both the strengths and the fracture strains of the samples decreased with increasing pre-stretch. In these experiments, the fracture energy of the specimen is related to the area under stress-stretch curves. The relative area under the curves for $\lambda_p = 1.5$ and $\lambda_p = 1.14$ in Figure 2.7A are 10% and 44%, respectively, of the area under the curve at $\lambda = 1$. Thus, these results indeed indicate that samples with larger alignments of polymer chains in the direction perpendicular to the crack (e.g., Figure 2.7C, $\lambda_p = 1$) demonstrate much larger values of fracture energy for forward cracking (i.e., they have much larger resistance to fracture), thereby supporting our hypothesis.

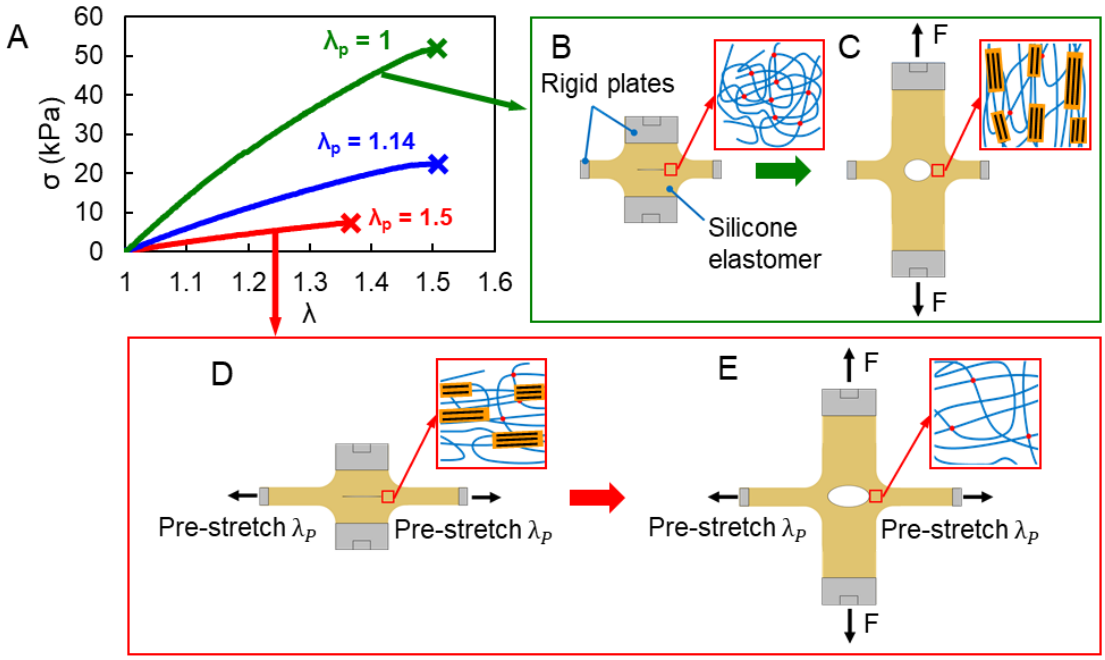

Figure 2.7 Experiments demonstrating the effects of polymer chain alignment and strain-induced crystallization on fracture energy. In the microstructural schematics, the red dots denote crosslinks, and the orange boxed regions represent crystalline domains. (A) Stress-stretch curves and (B)-(E) schematics of silicone elastomer specimens during fracture testing to examine pre-stretch effects. The insets show schematics of representative hypothesized chain orientations and crystalline domains at the given state: (B) original state of the specimen, (C) specimen with vertically applied load, (D) specimen pre-stretched in the horizontal direction before applying load, (E) specimen pre-stretched in the horizontal direction with a vertically applied load. Samples with large pre-stretches show significantly smaller areas under the stress-stretch curve, thereby indicating significantly smaller fracture energies for cracks propagating in the horizontal (forward) direction.

To provide further evidence as to whether polymer chain alignment and/or strain-induced crystallization occurred in these specimens, we performed a number of characterization studies. Frist, we implemented photoelasticity, which can provide evidence of polymer chain alignment (in a general sense) by using the alignment's

resulting influence on the optical properties of the material. Figure 2.8 shows the birefringence photos at a stretch of $\lambda = 4$. In the left panel of Figure 2.8, the polarizer and analyzer were set at angles of 0 and 90 degrees, respectively, relative to the stretching direction. In the right panel of Figure 2.8, the polarizer and analyzer were rotated to 45 and 135 degrees, respectively, relative to the stretching direction. The left image in Figure 2.8 shows a quite dark color, whereas the right image shows a bright white color, which indicates that chains do indeed align in the direction of the applied load during stretching.

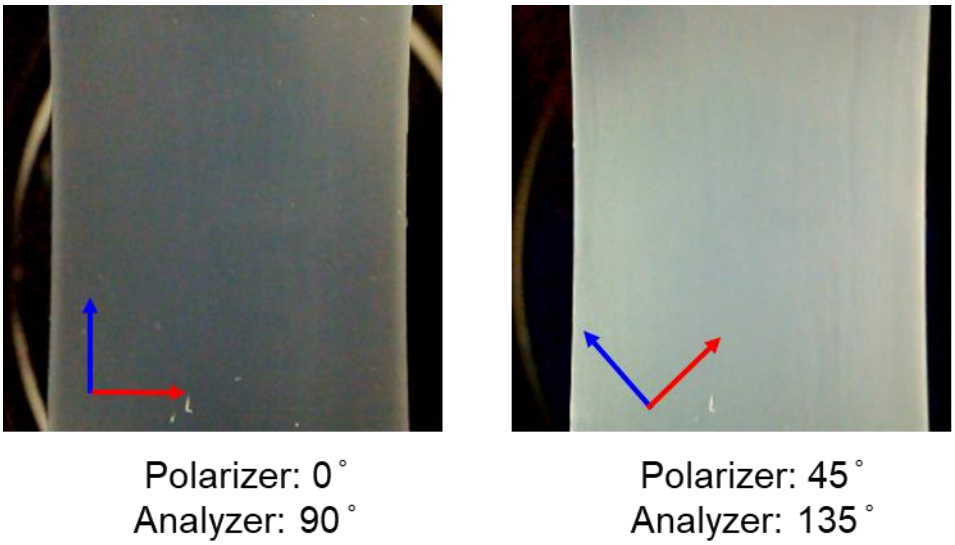

Figure 2.8 Birefringence images with different relative orientations of the polarizer and analyzer to the stretching direction at a stretch of $\lambda = 4$. The red and blue arrows indicate the filter direction of the polarizer and analyzer, respectively, relative to that of the stretching direction.

We also utilized x-ray diffraction (XRD) to probe microstructural changes during stretching of this elastomer. In Figure 2.9, the XRD patterns of Ecoflex change during stretching from that representative of an amorphous material to that representative of a semi-crystalline material. It can be seen that as the stretch increases, more crystallization occurs in the elastomer, as evidenced by the substantial increase in intensity of the peaks near $2\theta = 22.5^{o}$ and $2\theta = 34^{o}$ (Figure 2.9).

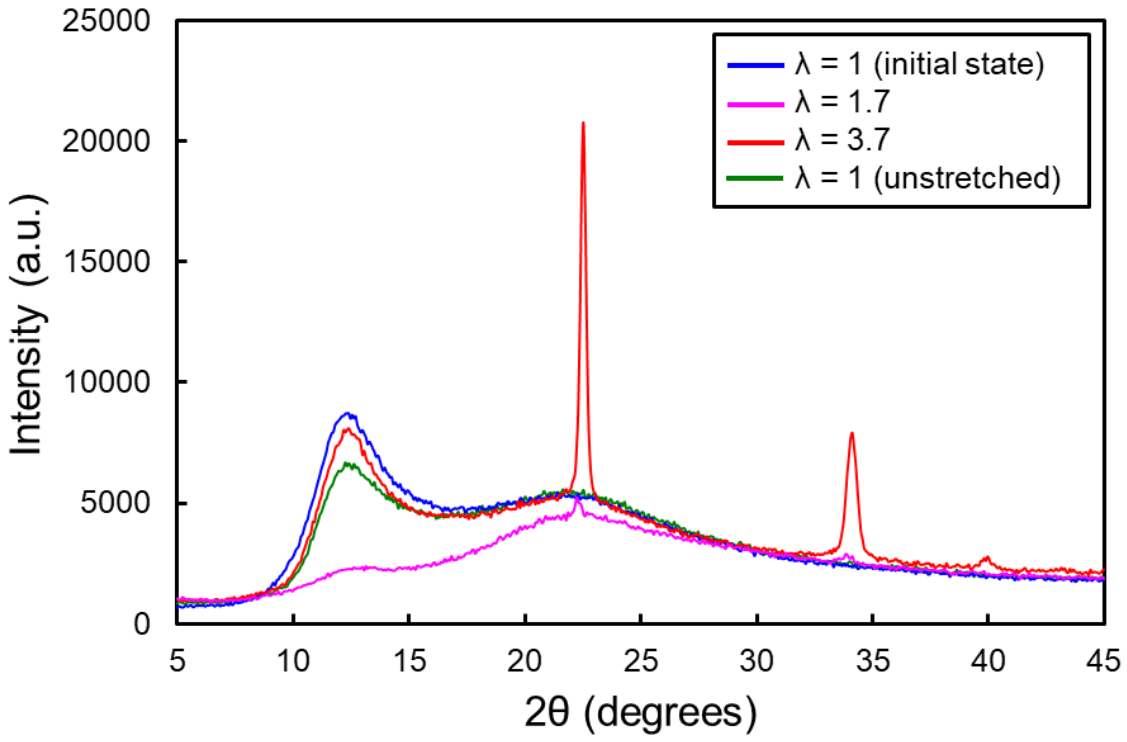

Figure 2.9 X-ray diffraction patterns of the silicone elastomer (Ecoflex 00-30) at λ = 1 (initial state), 1.7, 3.7, and 1 (unstretched).

It is also interesting to note in this figure that the elastomer apparently fully recovers back to its initial amorphous state upon release of the stretch. Differential scanning calorimetry (DSC) (in the unstretched state) also indicated an exothermic peak at -64.5°C that corresponds to the onset of crystallization during cooling, Figure 2.10. Likewise, an endothermic peak of the silicone elastomer occurs at -41.6°C during heating, thereby indicating the opposite phase transformation (amorphization), Figure 2.10. The glass transition temperature (T_g) of this silicone elastomer was not observed over a temperature range from -150°C and to 30°C which implies that T_g of this silicone elastomer is lower than -150°C.

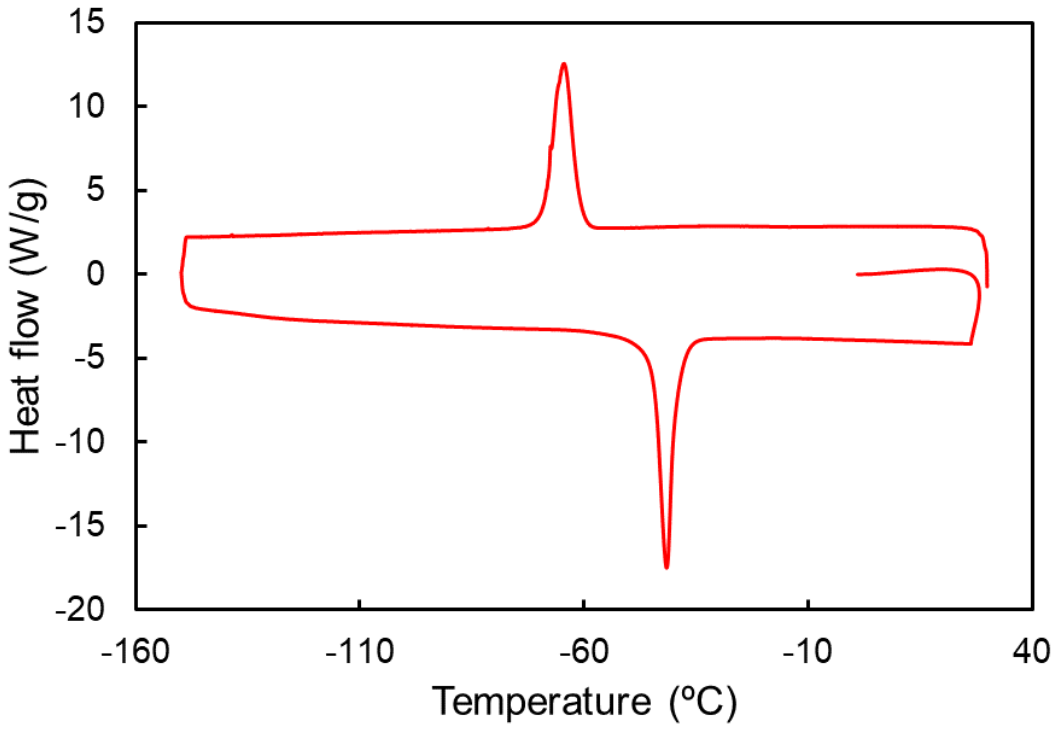

Figure 2.10 Differential scanning calorimetry curve of the cured silicone elastomer (Ecoflex 00-30).

Finally, to gain some basic information as related to polymer properties of this material, we performed matrix-assisted laser desorption ionization time-of-flight mass spectrometry (MALDI-TOF), which indicated that both precursors of the silicone elastomer ('Part A' and 'Part B') consist of the base polymer with additives (Figure 2.11). The differing patterns for Parts A and B in the low m/z (mass to charge ratio) range of the spectra indicate that each precursor contains different types and amounts of additives. The top insets in SI appendix, Figure 2.11 show the isotopic distributions with a center peak at m/z = 3006 and m/z = 3155 for Parts A and B, respectively. These values indicate the number averaged molecular weight of the polymers in the precursors in units of g/mol (since the charge of the cation in this mass spectroscopy almost always +1, the mass to charge ratio corresponds to the mass of the measured cation). Both spectra show repeat spacings of m/z = 74 (see the bottom insets of Figure 2.11). This value is equivalent to the molecular weight of the repeat unit of polydimethylsiloxane (PDMS, $(C_2H_6OSi)_n$), a well-known silicone elastomer. Combining these two results implies that each base polymer consists of ~40 and ~42 repeat units for Parts A and B, respectively (ignoring end groups).

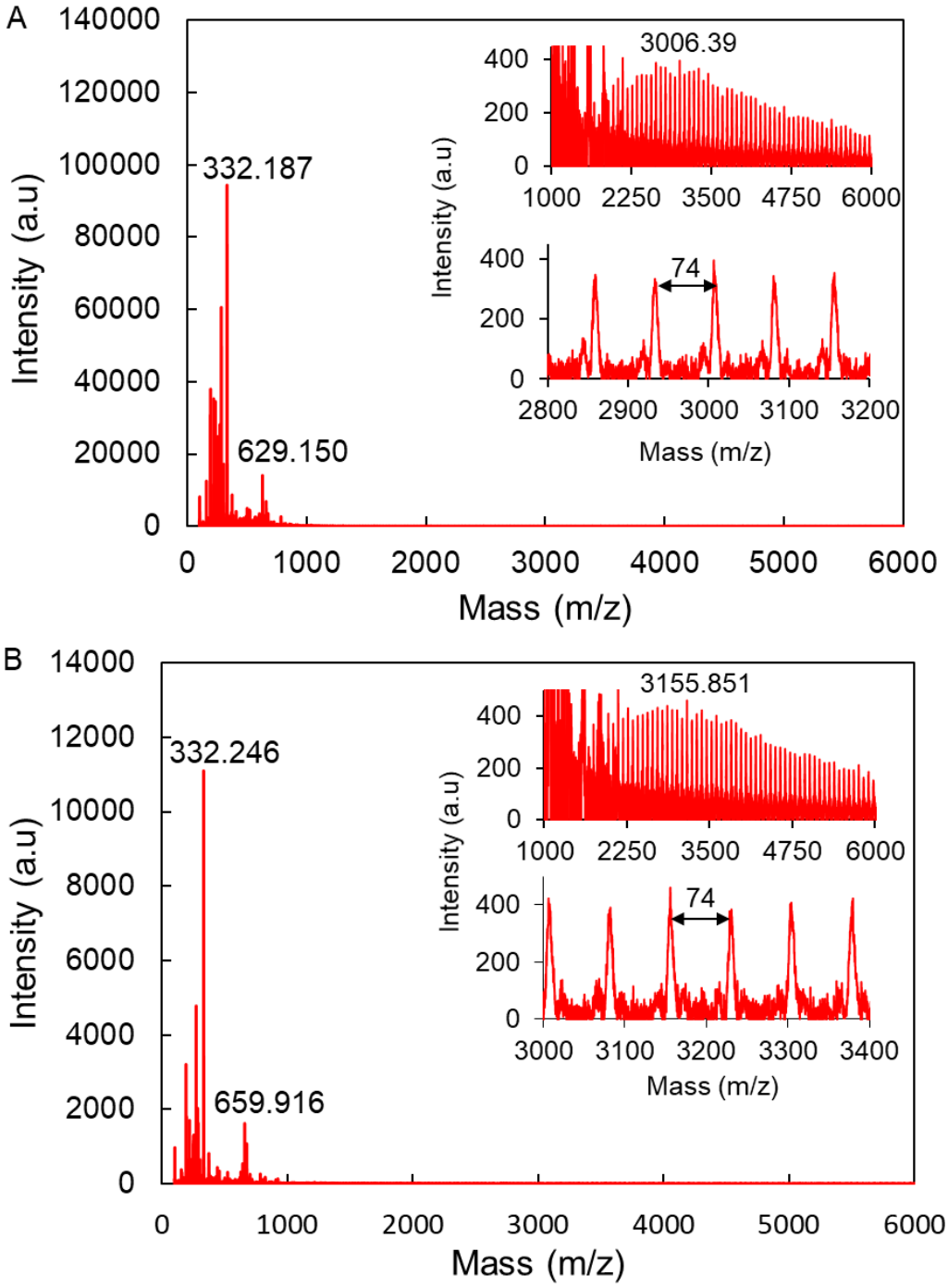

Figure 2.11 MALDI-TOF spectra of the pre-cursors of the elastomer with zoomed views in the upper right corner. (A) Part A of the silicone elastomer. (B) Part B of the silicone elastomer.

Overall, these experiments provide further credence to the proposed microstructural origins of the anisotropic fracture energy outlined in this section (Figure 2.7). In particular, due to the increasing levels of chain alignment and crystallization with increasing stretch level, it is likely that the microstructure near the crack tip is highly spatially inhomogeneous, due to the large stress gradients near the tip (Figure 2.12). Namely, a region in front of the crack tip (i.e., in the forward crack sense as depicted by the inset on the right) has relatively large stresses, which induce high levels of chain alignment and crystallinity. By comparison, a region 'above' the crack tip (i.e., in the sideways crack sense as depicted by the inset on the left) has less alignment and crystallinity. As such, the fracture toughness is highly anisotropic near the crack tip.

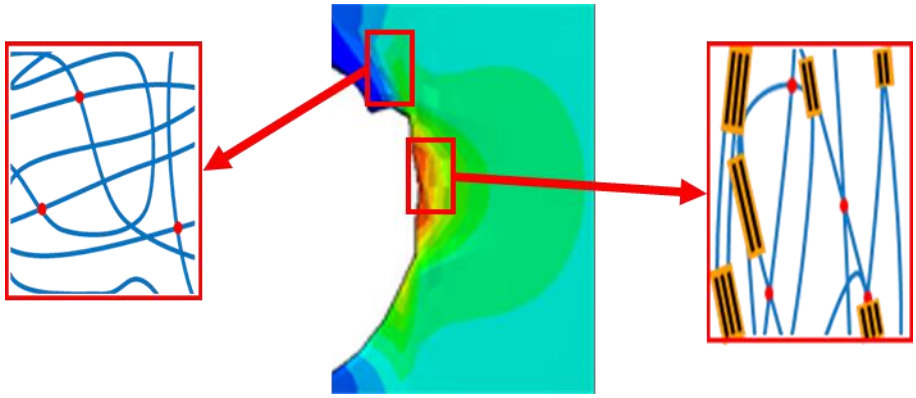

Figure 2.12 Inhomogeneous distribution of microstructure at two locations of interest near a crack tip due to large stress gradients near the tip.

2.5. Effects of sample geometry and loading rate on the propensity for sideways cracking

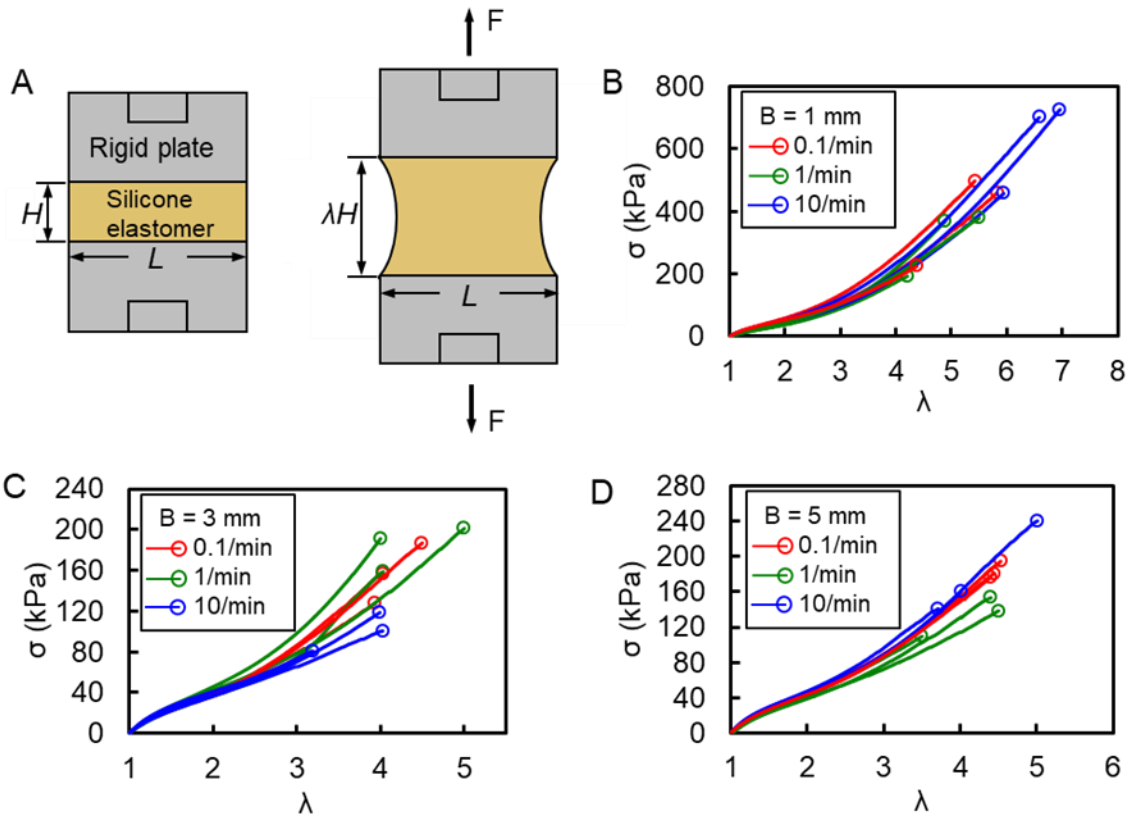

Figure 2.13 (A) Schematic of a silicone elastomer during pure-shear testing and (b-d) stress-stretch curves at various stretch-rates for pristine specimens (no pre-cut) with thicknesses of (B) B = 1 mm, (C) B = 3 mm, and (D) B = 5 mm.

To examine the propensity for sideways cracking under various sample and loading conditions, we performed tests with samples under the so-called pure-shear geometry, as shown in Figure 2.6. Specimens were stretched in the vertical direction (along H) under constant stretch-rates (0.1/min, 1/min, and 10/min) for samples of various thickness, B, (~1, 3, and 5 mm). Figure 2.13 shows that the stress-stretch

response of the as-fabricated elastomer does not demonstrate any significant rate effects over the tested range of stretch rates. By contrast, we found that the fracture behavior of pre-cut specimens strongly depends on the stretch rate (test data shown in Figure 2.14A).

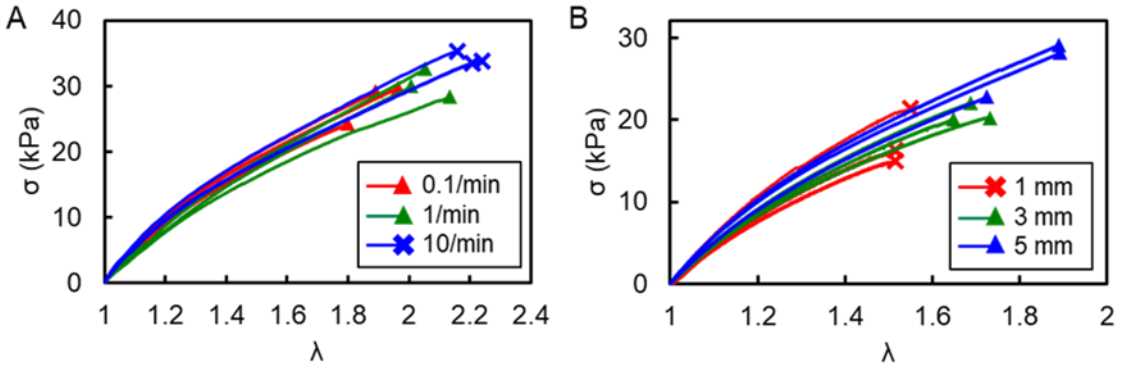

Figure 2.14 (A) Representative stress-stretch curves of fracture tests under a pure-shear geometry at different stretch-rates (thickness B = 5 mm). (B) Representative stress-stretch curves of fracture tests under a pure-shear geometry at different thicknesses (stretch-rate $\dot{\lambda}$ = 0.1/min). ▲ and X represent the location of the onset of fracture in the sideways and forward directions, respectively.

Namely, Figure 2.15 shows that forward crack propagation generally occurred at larger stretch rates, whereas sideways cracking generally occurred at smaller stretch rates. One potential explanation for this behavior is that the processes associated with forwards and sideways cracking may involve different microstructural mechanisms. For instance, forward cracking may primarily involve breaking covalently bonded polymer chains and crystalline domains, whereas sideways cracking may largely involve viscous-type separation between individual chains (e.g., as in Figure 2.12). The distinct microstructural mechanisms associated with fracture will have different time scales associated with them, which thereby may produce rate-sensitive fracture. Another

potential explanation is that strain-induced crystallization (as evidenced in Figure 2.9) takes time. As a result, developing highly anisotropic microstructures required for significant anisotropic fracture toughness takes time. As such, loading at high rates may not allow enough time for anisotropic microstructure/toughness to develop, thereby only leading to forward cracking.

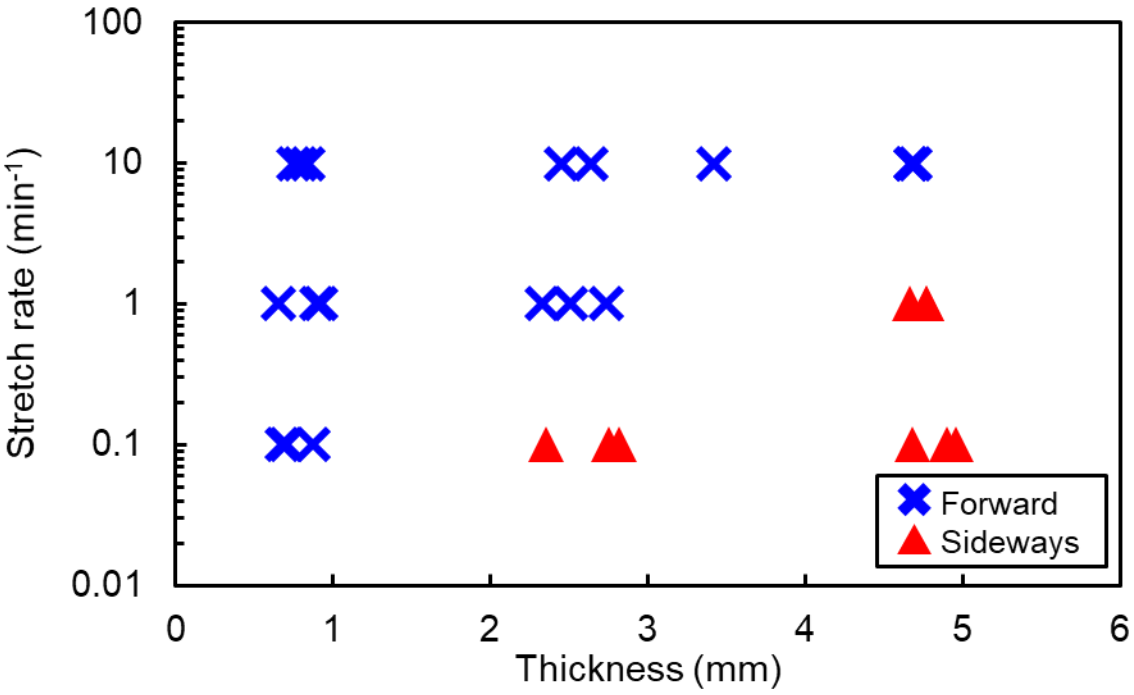

Figure 2.15 Scatter plot showing the propensity for sideways crack propagation in an elastomer of various thickness and subjected to various stretch rates. Generally, sideways crack are more prevalent in thicker samples and under lower stretch rates.

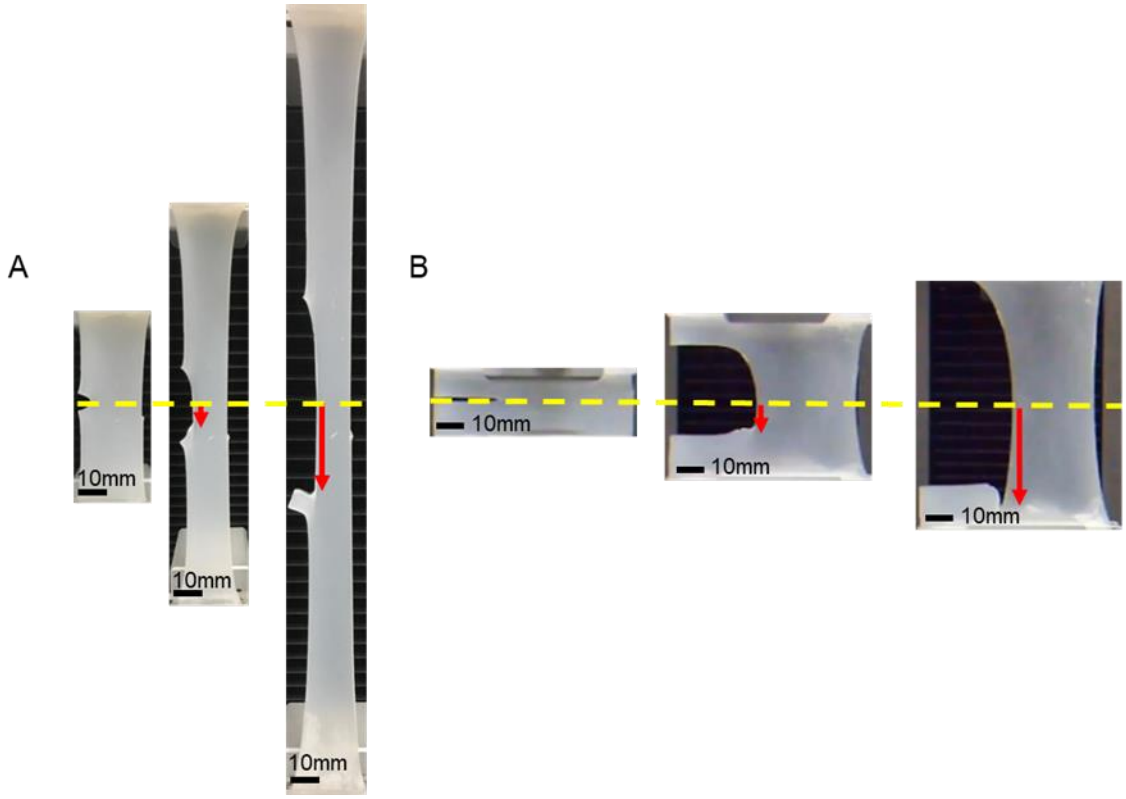

Figure 2.16 Representative images of sideways cracking in a silicone elastomer for different geometries. (A) Simple extension type geometry (H/L = 2.5) and (B) pure shear type geometry (H/L = 0.3).

Additionally, Figure 2.15 shows that forward crack propagation generally occurred in thinner specimens, whereas sideways cracking generally occurred in thicker specimens. One potential explanation for this behavior is related to the distribution of defects in the material. Thicker samples generally have more defects/heterogeneities, which could produce configurations near the crack-tip that are conducive to sideways cracking. However, we should point out that we believe 'sideways' cracking is not merely a geometric 'artifact'; that is, it does not occur solely due to boundary effects. To

substantiate this claim, we performed further experiments in an entirely different loading geometry, that of 'simple extension' (Figure 2.16). Under otherwise similar conditions, both 'simple extension' and 'pure shear' tests produced sideways cracks (Figure 2.16), thereby indicating that sideways cracking can occur under a wide range of geometries.

2.6. Materials and experiment methods

Fabrication of test specimens involved mixing Smooth-On Ecoflex 00-30 in a 1:1 ratio (Part A: Part B), followed by stirring for 3 minutes. Casting into molds formed the shape of the test specimens, and placing in a vacuum for 10 minutes removed bubbles. Curing at room temperature for at least 4 hours produced the final specimens. Gluing the cured specimens directly to acrylic plates helped mitigated stresses induced by gripping and helped prevent slipping during mechanical testing. For pre-cut specimens, cutting with razor blades produced sharp tips in the specimens.

For all of the experiments, tensile tests used an Instron model 5943 with a 1 kN load cell. The stretch along the H direction was measured as $\lambda = (H+\Delta H)/H$, where ΔH is the cross-head displacement. We defined the stretch at rupture for pre-cut samples as the moment at which the crack started to propagate, as determined by corresponding video footage during the experiments. In the case of the samples without a pre-cut, fracture did not occur (failure occurred at very large stretches due to slipping between the sample and the grips).

To investigate the anisotropy of the fracture energy (Figure 7), we adopted three different pre-stretch values ($\lambda = 1$, 1.14, and 1.5) on ~3 mm thick specimens. The

direction of the pre-stretch is parallel to that of the initial crack. We subsequently applied loads in the direction perpendicular to initial crack at a stretch rate of 1/min.

We adopted tests in a pure shear geometry (43) (Figure 6 and Figure 9) to investigate the effect of sample geometry and loading rate on the propensity for 'sideways cracking'. The tensile tester stretched specimens in the vertical direction (along H) under a constant stretch-rate (0.1/min, 1/min, and 10/min) for samples of various thickness, B, (~1, 3, and 5 mm). For each testing condition, we tested three samples with a pre-cut as well as three samples without a pre-cut (as fabricated).

We performed x-ray diffraction (XRD) on cured (solid) Ecoflex 00-30. Ecoflex samples with different stretch levels of $\lambda = 1$ (initial state), 1.7, 3.7, and 1 (unstretched) were analyzed by a Bruker-AXS D8 advanced Bragg-Brentano x-ray diffractometer. XRD patterns were obtained using Cu radiation ($\lambda = 1.54$ Å) over 2θ from 5˚to 45˚at room temperature.

We also performed differential scanning calorimetry (DSC) and thermogravimetric analysis on cured (solid) Ecoflex. Heat flow and weight changes associated with material transitions were measured as function of time and temperature with a TA instruments Q2000 and SDT Q600 over a temperature range from -150℃ to 30℃.

The platinum catalyzed silicone elastomer used in this study (Smooth-on Ecoflex 00-30) consists of two precursors ('Part A' and 'Part B'). The mass to charge ratio of each precursor was measured by matrix-assisted laser desorption ionization time-of-

flight mass spectrometry (MALDI-TOF). This technique produced mass spectra of the precursors to determine the molecular weight of the repeat units.

2.7. Summary and conclusions

We have identified an intriguing form of fracture in a silicone elastomer in which the crack turns and propagates stably in a direction perpendicular to the initial precut. The length of the sideways crack slowly increases with increasing load, and the crack arrests if the loading stops. The crack never turns back to the standard direction or shows any bifurcation. We call this behavior sideways and stable cracking. As a result of sideways cracking, the material ahead of the crack tip can continue to sustain load, thereby enabling enormous stretchabilities. To explain this phenomenon, we performed finite-element simulations, which demonstrated that the crack driving force in the "forward" direction is not orders of magnitude larger than that of the sideways direction. Likewise, these simulations show that large crack-tip blunting increases the propensity for sideways cracking to occur. These simulations suggest that a moderate level of anisotropy in fracture energy may produce sideways cracking. To this end, we performed fracture testing of samples transversely prestretched to various extents, which indeed indicate a large anisotropy in the fracture energy upon stretching. We also performed microstructural characterization through photoelasticity, XRD, and DSC, which indicate that significant chain alignment and strain-induced crystallization indeed occur in this material upon stretching. Finally, we systematically characterized how a number of loading conditions (sample geometry and loading rate) affect this

phenomenon. Generally, the propensity for sideways cracking increases with sample thickness and decreases with loading rate. We hypothesize that these observations are related to microstructural features associated with fracture, including the distribution of defects and the rate dependence of varying microstructural processes. As such, we hope that this study will motivate future studies of how specific microstructural features contribute to peculiar fracture behavior in elastomers and soft materials in general.

3. MAKING SOMETHING OUT OF NOTHING: ENHANCED FLAW TOLERANCE AND RUPTURE RESISTANCE IN ELASTOMER-VOID "NEGATIVE" COMPOSITES

3.1. Introduction

Imbued with high reversible stretchability, soft elastomers have found a wide range applications from industrial sealing (58-61) and dielectric sensors/transducers (62-66) to biomedical implants (67-69) and soft robotics (70-72). Of particular note, the elastic compliance and large reversible stretchabilities of silicone-based elastomers render them as ideal candidates for a new generation of flexible, stretchable, and wearable electronics (6, 50, 73-75). Still, many of these applications require resilience to extreme mechanical loading, including large stretching, bending, and twisting without incurring damage, i.e., they require large fracture resilience. Additionally, large-scale applications have been proposed, e.g., in using dielectric elastomers to harvest energy from ocean waves (76). In large-scale applications, flaws from the manufacturing process tend to be larger than in producing smaller specimens. Likewise, 3D printing of elastomers is an emerging field but typically produces relatively large flaws during the printing process (77-81). With sufficiently large flaws or any other features that cause inhomogeneous deformation (e.g., clamped boundary conditions), elastomers are prone to rupture.

To achieve better mechanical performance in these applications, previous research has focused on making stronger and tougher elastomers through chemical

modifications (e.g., introducing double networks of crosslinked elastomers) (82, 83) and by adding reinforcing materials (84-88). Notably, previous studies in elastomers have demonstrated the potential of stiff reinforcing materials to improve mechanical performance (87, 89). One well known example of a particle-reinforced composite is carbon black filled rubber (44). In these systems, interfacial bonding between the particles and matrix, the shape and size of the filler, and the distribution of the particles all affect the mechanical behavior of the composite system (3). In specific regards to silicone-based elastomers, previous studies have utilized silica particles (90), liquid metals (87), and fibers (86, 89) to strengthen the material. From a fracture perspective, some of these studies have demonstrated crack-tip deflection during fracture due to interactions of the cracks with the reinforcing materials (87, 89). The deflection can produce longer crack paths during rupture or can even temporarily arrest the crack at certain positions, thereby increasing the overall toughness and allowing regions ahead of the crack to sustain more load prior to macroscopic failure (82, 87, 91). However, adding reinforcing materials to an elastomeric matrix usually engenders complex fabrication processes, additional cost, and increases in weight. Likewise, most of these composites are comprised of soft matrices and stiff filler; as such, the material stiffness increases, which typically decreases stretchability.

In this work, rather than adding a reinforcing material, we disperse voids into the silicone elastomer matrix, thereby creating a “negative composite.” These structures are somewhat similar to foams, which include open foams, closed foams, and syntactic foams, and widely used in polymeric matrices as core materials in sandwich structures

due to their excellent compressive strength and impact resistance (92-96). Mechanical behaviors of theses foam materials strongly depends on the foam density, solid polymer properties, macrostructures, size, and location of defects (e.g., center hole and edge crack) (92, 97). For example, in rigid polyurethane foams fracture toughness increases with density (98). Rigid closed-cell polyurethane foams can show multiple arrests and diversions during crack propagation due to the presence of microstructural features (99). Material strengths of foam materials are generally insensitive to the defects when the defects are smaller than the cell size of the foam. However, for defects larger than the foam cell size, the situation is complicated, sometimes with the effective strength increasing and other times with it decreasing (92). Furthermore, the elastic moduli of foam materials generally decrease with increasing void volume fraction due to the reduction of the total solid volume. However, syntactic foams, which are created by dispersing pre-formed spheres of relatively stiff materials, including glass, ceramic, and other polymers into a polymer matrix often increases modulus of the materials due to the strong interfacial adhesion between the microsphere and matrix, and thus transmission of force to the relatively stiff components (97). As a result, both the filler type as well as the filler-matrix interactions are additional factors that influence the mechanical behaviors of syntactic foams (100).

While previous studies have focused on the mechanical behavior of rigid polymeric foams and metallic foams with randomly distributed voids, herein we have investigated two different types of elastomer-void “negative composites”. One implements periodic interconnected rectangular prismatic voids, while the other

implements randomly distributed spherical voids for comparison. Similar structures are, in fact, commonly used in tissue scaffolding (101-105). The voids reduce the weight of the specimen, increase the compliance, and intuitively locally weaken the materials. As a result, the voids provide a means of crack-tip deflection, thereby guiding the crack along a more tortuous path and potentially into configurations less susceptible to subsequent propagation. To demonstrate these effects, we perform uniaxial tension tests of pre-cut specimens with two general void geometries (interconnected diamond patterns in section 3.2 and randomly-distributed spherical voids in section 3.3) and quantify their fracture resilience relative to that of the base elastomer (and each other). In section 3.2, we also perform fracture tests with single extended voids oriented at various angles relative to a pre-cut to provide insight into interactions between cracks and defects. Corresponding finite element simulations elucidate how stress/strain fields evolve as the crack approaches these defects, ultimately producing deflection. Overall, this chapter demonstrates that the introduction of voids can increase the effective fracture resistance and stretchability while simultaneously reducing weight in elastomers with flaws.

3.2. Effects of interconnected architected voids on the fracture behavior of silicone elastomer

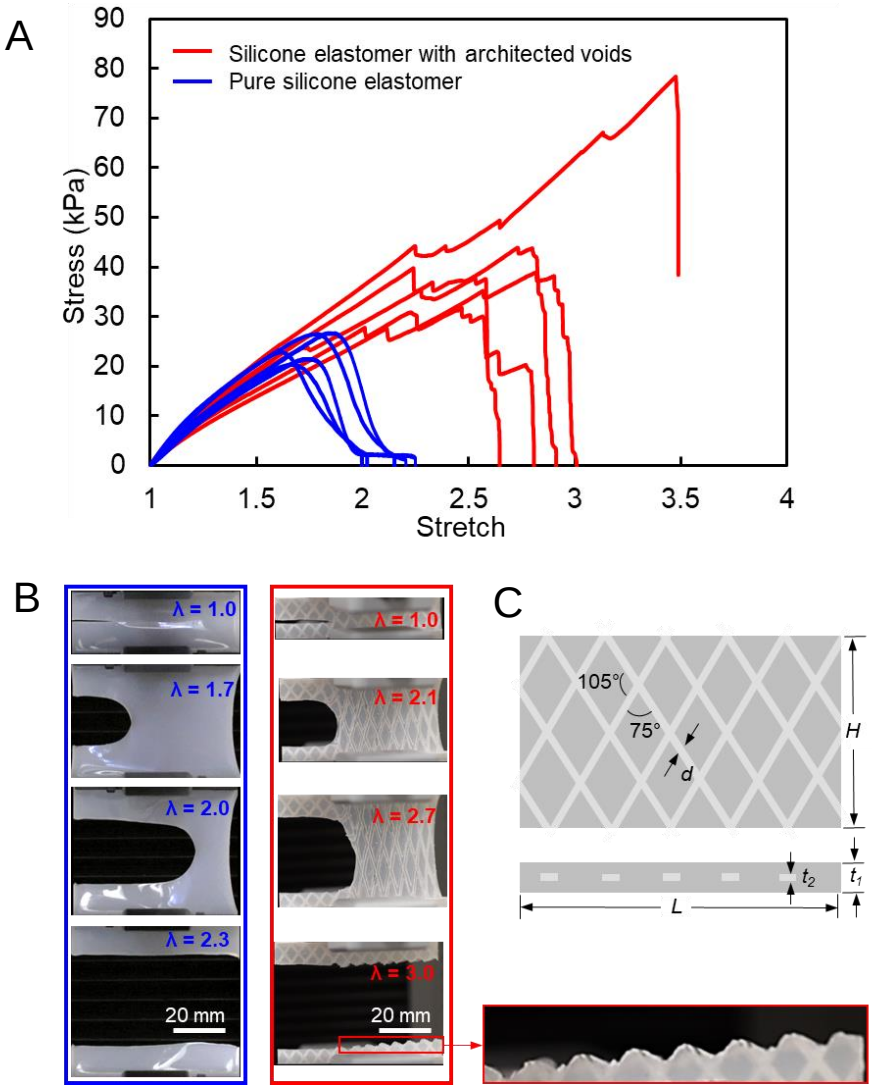

Figure 3.1 (A) stress-stretch curves of pure silicone elastomer and the same silicone elastomer with architected voids. Each specimens was precut and loaded under uniaxial tension at a stretch rate of 0.1/min. (B) Corresponding snapshots during fracture testing. λ = 1.7 is the stretch at the onset of crack propagation in the pure silicone elastomer and λ = 2.1 is the stretch at the onset of crack propagation in architected elastomer. (C) Schematics of silicone elastomer with architected voids.

We have investigated fracture behavior in a pre-cut silicone elastomer both with and without architected voids. The samples with architected voids consisted of interconnected voids of rectangular prisms in the elastomer (Figure 3.1). We designed this void pattern to deflect and "guide" the crack by generating locally weaker regions in the elastomer. A pre-cut was introduced into the samples prior to loading. Figure 3.1 shows the engineering stress-stretch response of pre-cut silicone elastomers (Ecoflex 00-30) with and without architected voids, along with representative photos during crack propagation.

We adopt the "pure shear" geometry of Rivlin and Thomas, (106) loaded in the vertical direction using displacement control at a constant stretch rate of 0.1 / min. For the pure (no void) silicone elastomer (blue curves in Figure 3.1A), the stress increases with increasing stretch until reaching a critical value (23 ± 2.7 kPa occurring at $\lambda = 1.7 \pm 0.1$), at which point the crack begins to propagate straight across the sample, as seen in the second image of the blue series in Figure 3.1B. A drop in load occurs during crack propagation, as the region behind the crack front has no (or little) load bearing capability. For the pure (no void) elastomers, during crack propagation, the stress decreases with stretch in a smooth and continuous fashion, as seen in Figure 3.1A.

For the architected void samples, the crack propagation initiates at a stress of 28 ± 1.9 kPa with a stretch of 2 ± 0.2, a larger stress and stretch compared to the pure samples, as seen in Figure 1a and in the second image of the red series in Figure 3.1B. Moreover, in the architected samples, the crack does not propagate forward quickly. Instead, as the crack begins to propagate forward, it turns to deflect along the locally-

weaker void pattern. In doing so, the crack orients itself more parallel to the loading direction, thereby reducing the stress ahead of the crack (in the "forward" direction). As a result, the strain energy release rate decreases, stopping the crack temporarily, and requiring that the external load increase prior to further propagation. As the load increases, the crack continues to propagate intermittently, frequently arresting before switching directions (leading to observable kinks in the stress-stretch curve). Overall, this tortuous path of the crack improves the samples' resistance to complete failure. Additionally, in one test, the crack deflected to a steep angle and stopped propagating almost completely until reaching a very high load, as seen in the uppermost curve of the red series in Figure 3.1A. As calculated by integrating the area under the stress-stretch curve, the total energy dissipated by the architected voids specimens is 43 ± 8 kJ / m^3 for the samples tested (54 ± 27 kJ / m^3 when including the extreme test in which the crack nearly completely arrested). These numbers are more than three times the energy dissipated by the pre-cut pure (no void) silicone elastomer samples (14.3 ± 3.4 kJ / m^3).

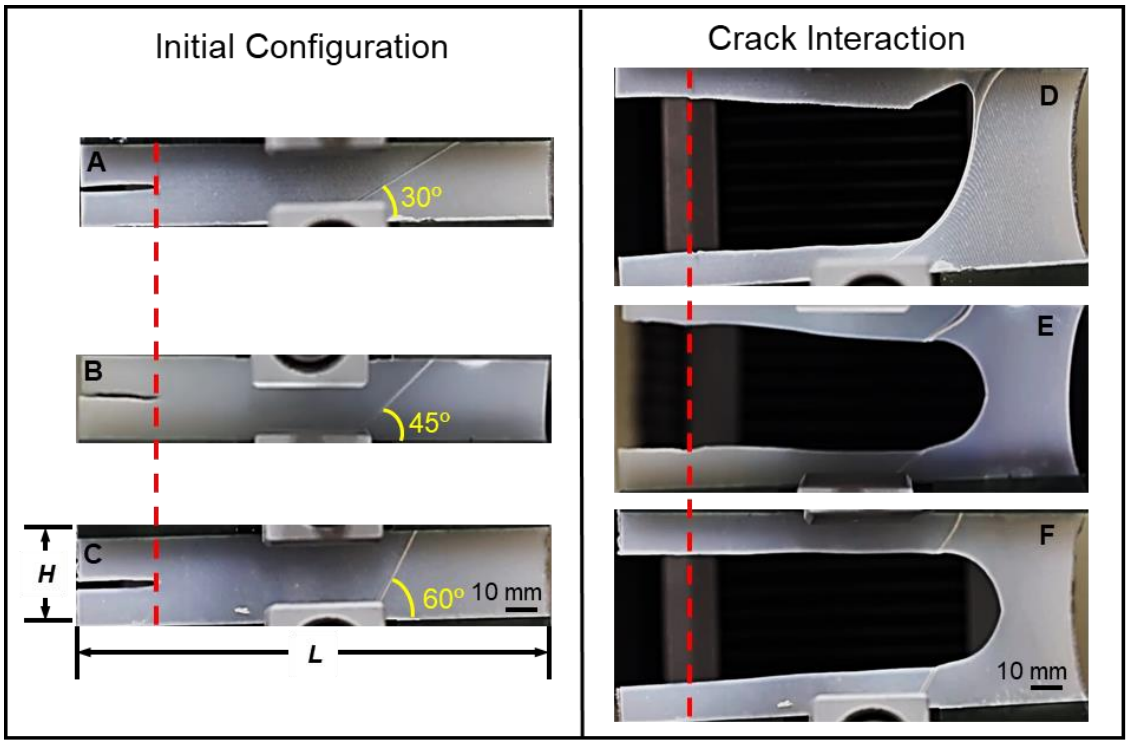

Figure 3.2 (A), (B), and (C) represent the initial configuration of precut specimens with single columnar voids initially at (A) 30°, (B) 45°, and (C) 60° to the precut (horizontal). (D), (E), and (F) represent the corresponding images as the crack interacts with the cylindrical void. Samples were tested at a stretch rate of 0.1/min.

We conducted additional experiments and ABAQUS simulations to provide further insight into the mechanism governing the crack path. Namely, we performed additional "pure shear" type tests on specimens with a single void at an oblique angle (at 30°, 45°, and 60° to the pre-cut at the beginning of the test), as seen in the left-most column of Figure 3.2. Upon reaching a critical load, the crack began to propagate in the direction of the initial pre-cut. As seen in the right column of Figure 3.2, for the 45° and 60° samples, the crack continues to propagate through the defect undeterred. However, for the 30° sample, the crack path clearly follows the angle of the void. This result

confirms the intuitive idea that a crack is more likely to follow a void that is closely aligned with the direction perpendicular to the largest component of stress, i.e., at a small angle relative to the pre-cut direction. Figure 3.3 displays finite element simulations in ABAQUS that support this intuition by showing the local deformation and stress fields as the crack approaches voids at various angles to the crack. The region in front of the crack appears similar for the pure and the 60° samples. However, for the sample with a void at 30°- 45° to the crack, the region near the void and ahead of the crack tip shows a high local stress. As a result, it is easy to see how a thin ligament of material along the void will rupture more readily than will the dense area directly in front of the crack.

These results suggest that the likelihood for the crack to propagate along a void depends on the angle between the crack and direction of maximum principal stress in regions ahead of the crack tip, i.e., the "direction" of the defect relative to the crack. As the crack deflects along an angled void, it aligns itself more with the applied load, which decreases the subsequent driving force for crack propagation, thereby potentially arresting the crack. Additionally, with increasing strain, the void further rotates relative to the initial pre-cut direction, which leads the crack to turn to an even higher angle that is even less favorable for propagation. Voids with larger dimensions relative to the thickness of the sample should also increase the likelihood of the crack to follow the void, as the ligament of solid material is thinner, further increasing the stresses in regions near the void.

Overall, Figures 3.1-3.3 show that the architected voids have important effects on the mechanical behavior of pre-cut silicone elastomers: 1) The voids weaken the material locally, increasing the favorability for the crack to propagate along the void, i.e., for the crack to deflect, 2) the effective strength and stretchability of pre-cut specimens increases in samples with voids, and 3) the overall energy dissipated during the fracture process increases in samples with voids. We should also mention that crack deflection and hence energy dissipation likely depends on the diameter of the void relative to the thickness of the sample, the spacing between the voids relative to the size of the voids, and the angle between the void and crack. In the scope of this manuscript, we have not attempted to optimize these parameters but these considerations warrant future studies.

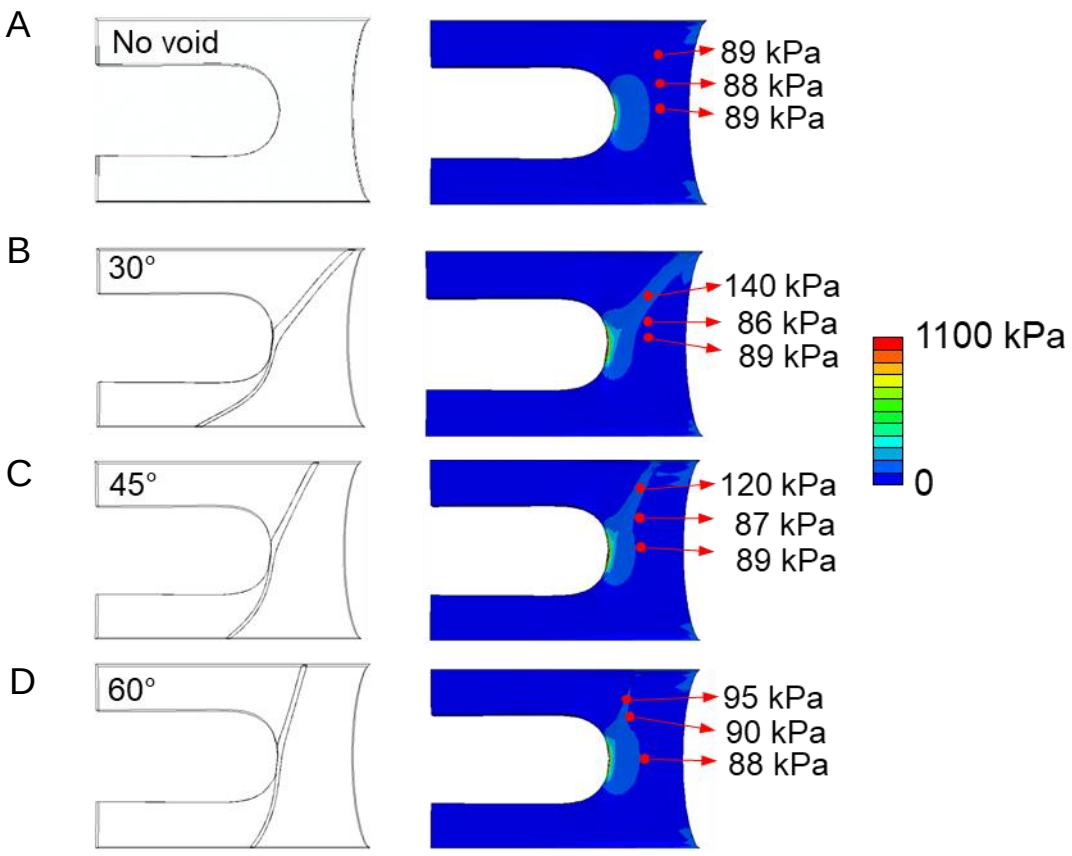

Figure 3.3 Deformed geometries and contour plots of the maximum principal stress for (A) a pristine specimens (no void), and for specimens with a single columnar void initially at (B) 30°, (C) 45°, and (D) 60° angles to the pre-cut direction (horizontal). Localized stresses occur near the void but this effect diminishes with increasing angle between the void and the horizontal.

3.3. Discontinuous voids and scaling of energy dissipation with void volume fraction

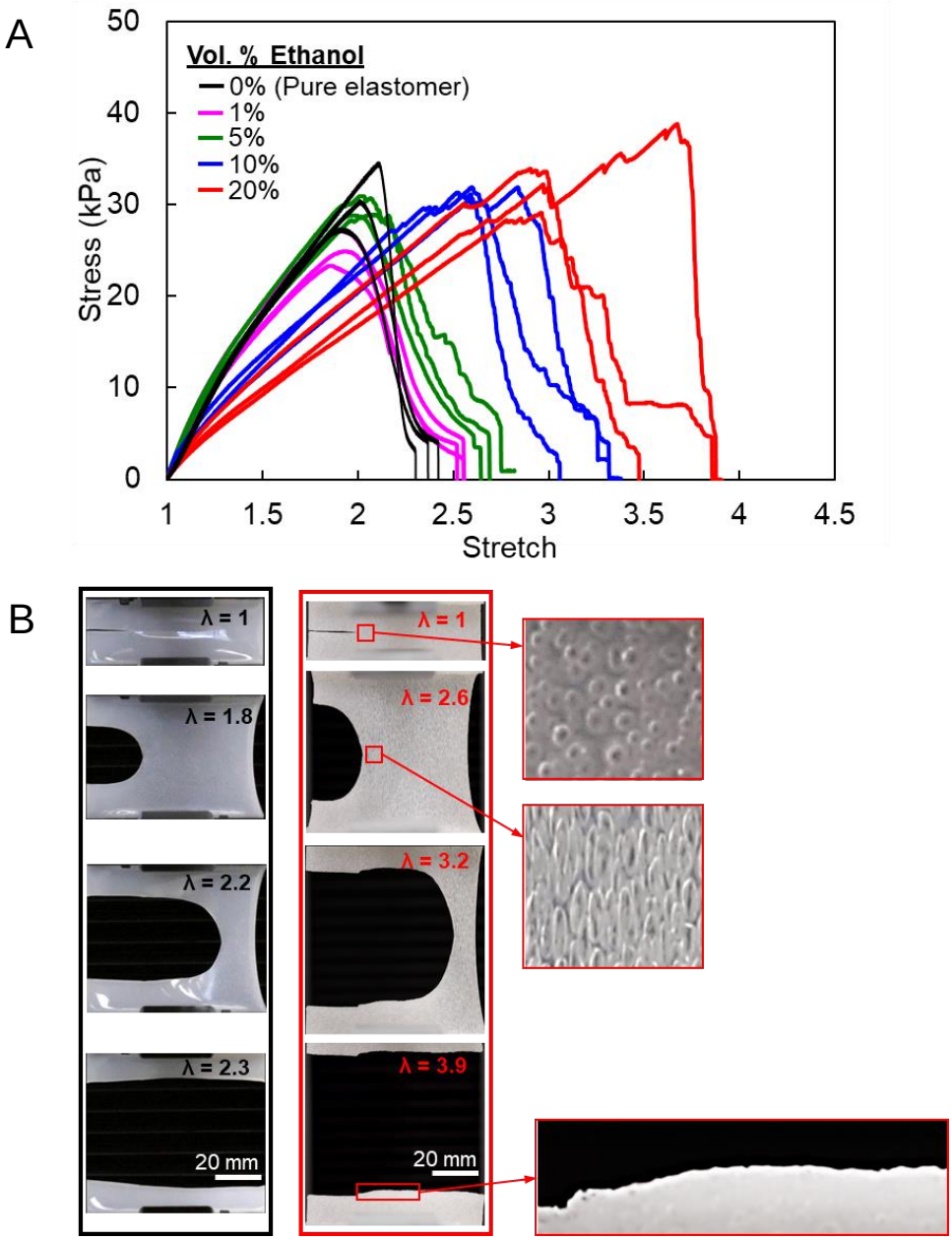

Figure 3.4 (A) Stress-stretch curves of pure silicone elastomers and elastomer-bubble composites of different volume ratios. The samples were pre-cut and loaded uniaxial tension at a stretch rate of 1 / min. (B) Corresponding snapshots of a pure specimen (no voids) and for 20% ethanol volume fraction. The second images in each column represent the time at which the crack began to propagate, while the bottom images represent the moment just after complete failure

While the experiments in Figure 3.1 use interconnected networks of voids, we also investigated discontinuous voids, as seen in Figure 3.4. These samples were produced by adding ethanol into the elastomer mixture, which leads to well-distributed bubble formation during curing (3). Controlling the relative amount of ethanol produced specimens with a similar distribution of bubble diameters (near 0.5 mm, as seen in Figure 3.8) but with a varied volume fraction of bubbles. The resulting specimen was then stretched at a stretch rate of 1/min. Similar to the architected void samples from Figure 3.1, the elastomer-bubble composites in Figure 3.4 display a perturbed crack path with intermittent crack propagation but seemingly to a somewhat lesser extent than in the architected void specimens. Furthermore, while the crack propagates at similar stress levels in each of the specimens, the stretch at propagation increased with bubble volume fraction, with averages stretches at propagation of 1.79, 1.91, 2.36, and 2.53 for 0.2, 8.9, 10.1, and 19.4 bubble volume %, respectively. Stretches at complete rupture also increased with increasing bubble volume fraction, with averages of 2.54, 2.69, 3.21, and 3.73 for 0.2, 8.9, 10.1, and 19.4 bubble volume %, respectively. Additionally, Figure 3.5 shows the total energy dissipation during crack propagation as calculated by the area under the stress-stretch curves. The dissipated energy appears to increase linearly with the volume percent of ethanol. Notably, the 20% volume fraction ethanol possesses an increase in dissipated energy by a factor of ~2.5 relative to the pure silicone specimens (the pure elastomer is tested at a strain rate of 1/min here).

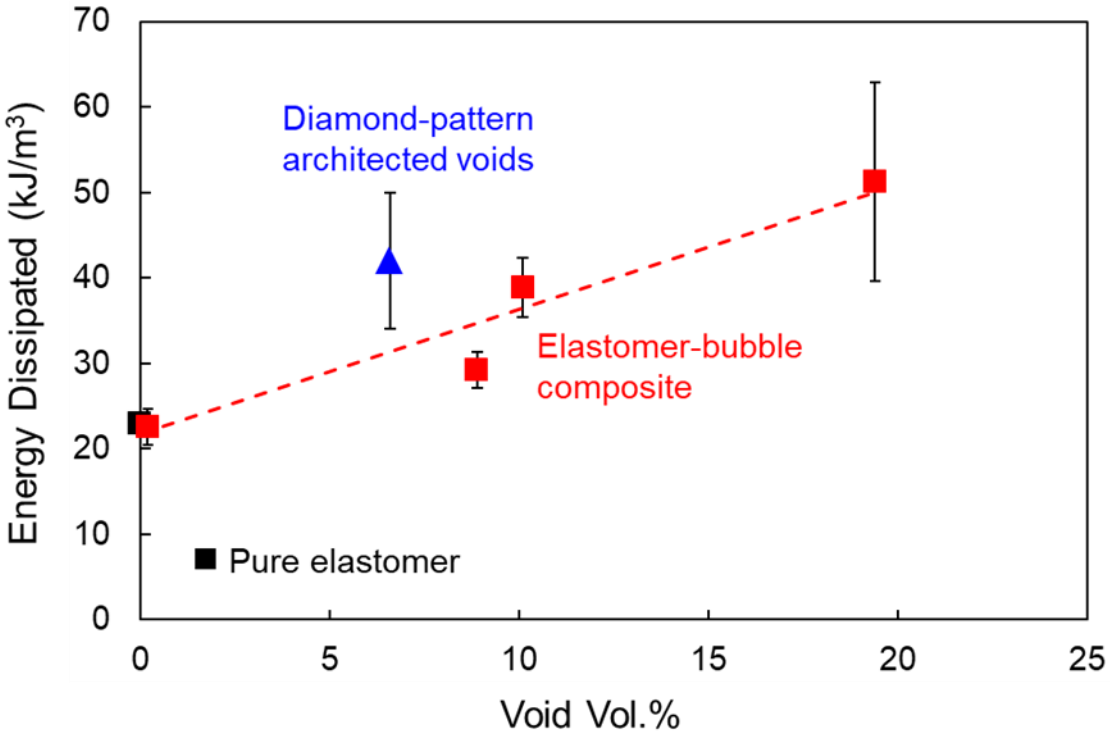

Figure 3.5 Energy dissipated by pre-cut specimens versus void volume fraction. The energy dissipated was calculated by integrating the area under the stress-stretch response until the specimen failed completely

Comparing the interconnected architected void samples with the elastomer-bubble composite samples provides insight into the geometric advantages offered by these void morphologies. Figure 3.5 displays symbols and error bars representing the average and standard deviation of the energy dissipated for the diamond-pattern architected voids (red series in Figure 3.1), as well as the elastomer-bubble composite and the pre-cut pure elastomer samples tested at a 1/min stretch rate. For the architected void samples, the volume occupied by the voids is 6.6% of the total volume. The inset in Figure 3.1B shows the failure surface (side view) for a representative architected void

sample, while the inset in the bottom right image of Figure 3.4B shows a failure surface (side view) for a bubble-elastomer composite sample. As seen in Figure 3.5, the architected void dissipates more energy than does the bubble-elastomer composite for the same volume fraction. This difference likely stems from the path that the crack follows for in each geometry. In the architected void samples, the crack is forced to follow a long path, occasionally kinking or switching direction when given the chance to propagate in a direction more aligned with the normal to the loading direction (as happens in the middle of the "X" in the patterned structure). Meanwhile, the crack deflections in the bubble-elastomer composites are much smaller due to the presence of many small bubbles, which provide more opportunities for the crack to travel in a direction more aligned with the normal to the loading direction. Since the crack path can more readily align with the normal to the loading direction, the stress component acting perpendicular to the path is larger for the bubble-elastomer composite, which causes the crack to propagate more readily under the same remote load, as compared to the architected voids. As a result, randomly distributed pores and voids in silicone elastomers, as seen in some previous applications (105, 107, 108), provide general improvement in energy dissipation for parts with flaws. However, geometries with extended defects, à la interconnected extended voids, may possess increased energy dissipation as compared to random voids: the extended defects "trick" the crack into following a longer and more tortuous path and even frequently leading to the crack getting "stuck" along the way. However, given that the crack's ability to deflect depends upon the angle between the void and the network (as indicated in Figures 3.2-3.3), more

work should be conducted to confirm that the architected void networks at various angles still continue to dissipate more energy than the discrete voids (bubble-elastomer composite). The authors do note that the comparison in Figure 3.5 is an imperfect one: the architected void specimens were tested at a rate of 0.1/min, while the elastomer-bubble composite specimens were tested at 1/min. However, pre-cut pure elastomer specimens at 0.1/minute stretch rate (not shown) dissipated less energy on average (16 kJ/m^3) than did the pre-cut pure elastomer specimens at 1/min stretch rate (23 kJ/m^3). Thus, while Figure 3.5 does not consider strain rate, any resulting error likely serves to understate the increased energy dissipated by the architected samples, as compared to the bubble elastomer composite.

We also note that the presence of voids and inclusions has previously been shown to decrease the strength of dogbone specimens of elastomers (80). In addressing this possibility, we tested dogbone specimens (without pre-cuts) for the pristine elastomer, as well as the bubble-elastomer composite and the architected elastomer samples (Figure 3.6). Indeed, the sample fails earlier in both the architected and bubble-elastomer composite samples, as compared to the pure elastomer, a finding consistent with previous studies. Thus, while the incorporation of voids may help improve the mechanical performance of flawed specimens, they do not necessarily improve the performance of specimens without flaws. However, we argue that while many parts used in practice do not have pre-cuts per se, many do have cracks, notches, or other features causing inhomogeneous deformation that act as flaws. For instance, the “flaw” may in fact be a rigid electronic component bonded to the elastomer, a sudden change in

geometry along the loading direction, or a sharp change in material type within a composite specimen. Thus, “negative composites” may prove useful for mitigating failure in such applications.

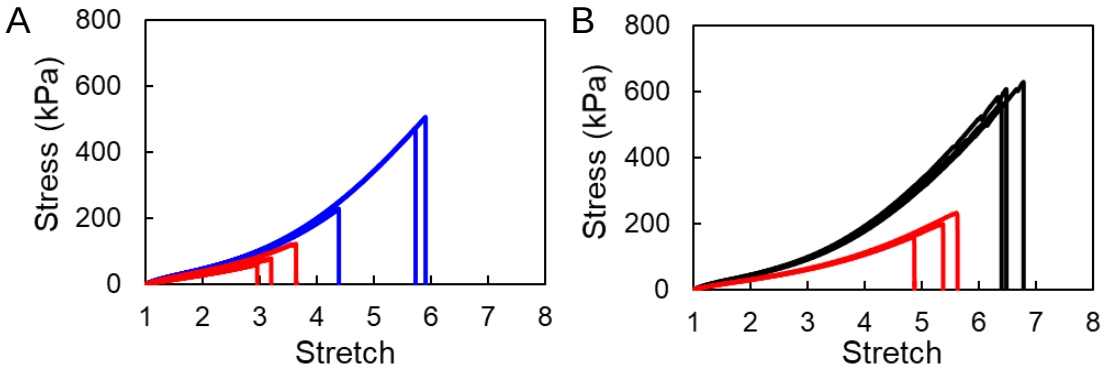

Figure 3.6 Stress-stretch curves of uniaxial tensile tests for dogbone specimens (with no pre-cut). (A) The red curves represent the architected void specimens, and the blue curves represent the pure elastomer (stretch rate of 0.1/min). (B) The red curves represent the elastomer-bubble composite specimens with 20 vol.% of ethanol at mixing, and the black curves represent pure elastomer specimens (stretch rate of 1/min). The gauge length and width of the dogbone were both 20 mm with a fillet radius of 15 mm. The grip width was 45 mm, and the total length was 104 mm. Both (A) and (B) demonstrate that the voids do not provide an advantage in the stretchability of the as-fabricated (no pre-cut) specimens.

3.4. Materials and methods

Architected void specimen preparation:

We use an approach similar to that of Mohanty et al.(109) to fabricated architected void specimens. Figure 3.7 shows the fabrication procedure step-by-step. First, polyvinyl alcohol (PVA) was 3-D printed in the desired pattern using eSUN brand 1.75 mm PVA filament (Figure 3.7A). Smooth-On Ecoflex 00-30 platinum catalyzed silicone elastomer was adopted as the matrix material. When pouring an elastomer

mixture over the printed PVA patterns, the PVA print tends to float to the top of the mixture. To ensure that the PVA was located in the center of the parts thickness, we poured the elastomer in two steps. First Parts A and B were mixed in a 1:1 ratio and poured into a mold up to two-thirds of mold thickness (Figure 3.7B). A printed PVA pattern was submerged in the solution, allowed to float to the top, and then cured at room temperature for 2 hours (Figure 3.7C). We then poured additional elastomer solution into the mold to fill the last third of the mold thickness, as to center the PVA structure through the thickness of the elastomer (Figure 3.7D). After the elastomer completely cured for 4 hours at room temperature, the lateral edges of the resulting specimen were trimmed with a razorblade to expose the PVA. The PVA, a water-soluble material, was then completely dissolved out of the specimen by placing the specimen in circulated water and on a hot plate for 48 hours at 80 °C (Figure 3.7E & 3.7F).

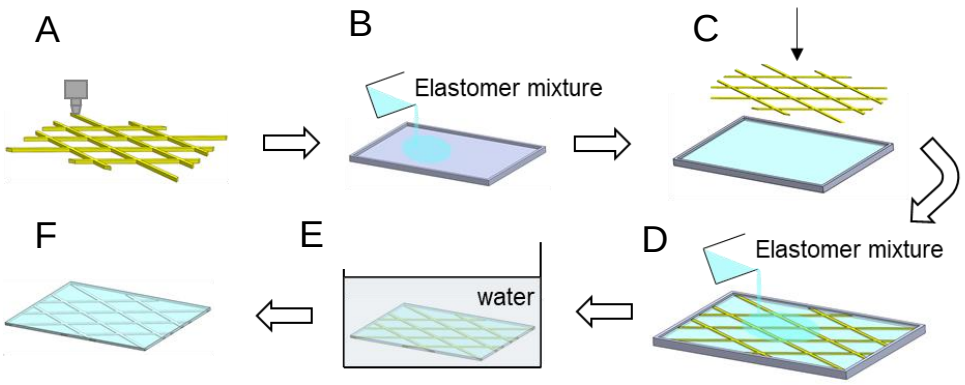

Figure 3.7 Fabrication process for architected void specimens. In (A), PVA filament is 3D printed into the desired pattern. In (B) and (C), a silicone elastomer is poured into a mold of the desired shape and put printed PVA pattern into the mold, then cured with the PVA structure embedded inside for 4 h at room temperature. (D) Elastomer mixture poured one more time on the top of cured PVA embedded elastomer. (E), the specimen is placed inside of the water to dissolve out the PVA structure for 48 h at 80 °C. (F) is the resulting architected void elastomer.

Elastomer-bubble composite preparation:

We have adopted a similar fabrication method for elastomer-bubble composites to that of Miiriyev et al. (108). Along with Smooth-On Ecoflex 00-30 Part A and B (1:1 mixing ratio), ethanol (KOPTEC, 200 proof) was mixed in at 1, 5, 10, and 20 percent volume fractions, followed by 24 hours of curing in a mold at room temperature. The volume fraction of bubbles generated during the curing time depended upon the volume the mixing ratio of ethanol. Cross-sectional images (seen in Figure 3.8) enabled the determination of the average bubble diameter and number in a given cross section, which were used in calculating the approximate bubble volume fraction (assuming spherical bubble geometries). 0.2, 8.9, 10.1, and 19.4 bubble volume % were obtained from the 1, 5, 10, and 20 percent volume fractions of ethanol, respectively.

Specimen geometries:

For the fracture tests of the pure elastomer, architected void composites, and elastomer-bubble composites, we implemented a “pure shear” type geometry (106) with a specimen thickness of t_1 = 3 mm, length L = 76.2 mm, and height H = 25.4 mm, as labelled in Figure 3.1C. For pre-cut specimens, a razor blade produced a 25.4 mm pre-cut at the left edge and mid-plane through the height. The architected void specimens implemented extended rectangular prisms in a diamond pattern with internal angles of 75º and 105º, thickness of voids t_2 = 1.2 mm, and width of voids d = 1 mm (Figure 3.1C). The dimensions of the single void with oblique angles specimens are specimen

thickness of t_1 = 3 mm, length L = 152.4 mm, height H = 25.4 mm, and a pre-cut of length 25.4 mm, as shown in Figure 3.2.

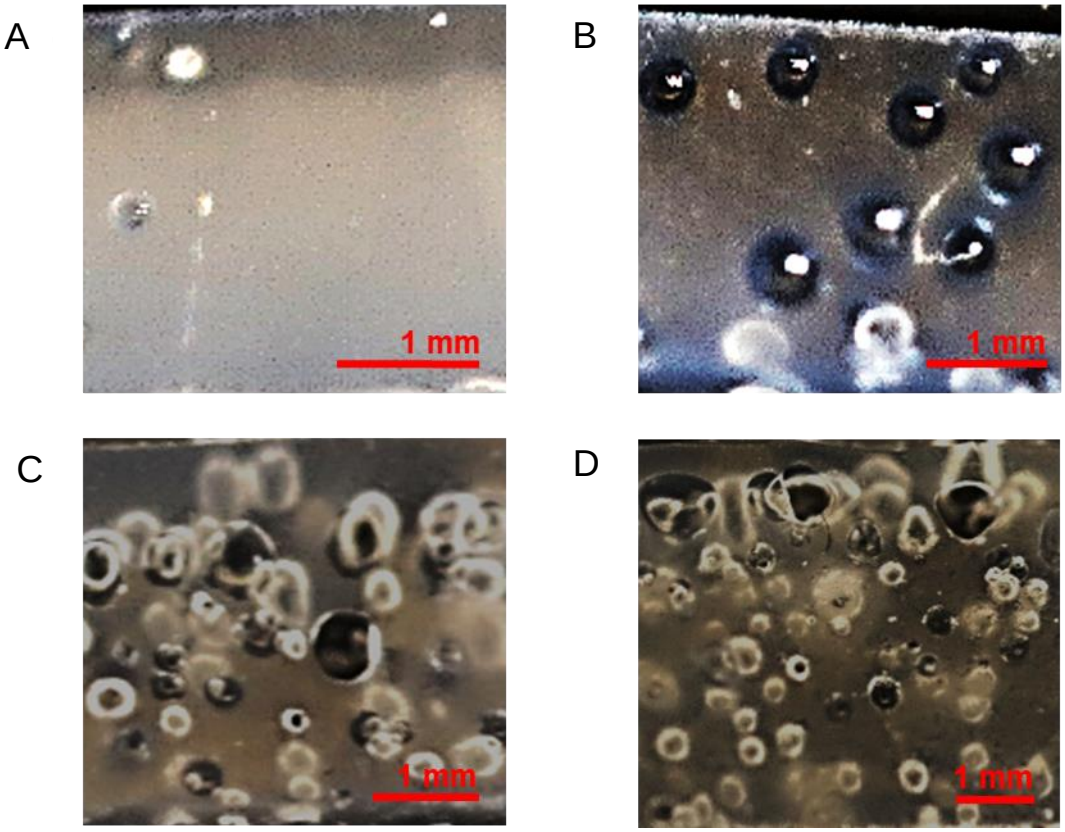

Figure 3.8 Images of cross section area of elastomer-bubble composites according to volume fractions of ethanol mixing: (A) 1vol.%, (B) 5 vol.%, (C) 10 vol.% and (D) 20 vol.% of ethanol. These ethanol mixing ratio generated 0.2, 8.9, 10.1, and 19.4 vol.% of bubble in elastomer-bubble composites respectively.

Finite element analysis:

ABAQUS finite element software was used to simulate specimens with a columnar void as seen in Figure 3.3. The dimensions of the model are 25.4 mm x 76.2 mm and 3 mm thickness. The simulations implemented a 20-node quadratic brick,

reduced integration, hybrid with linear pressure type element (C3D20RH). The lower face was given a fixed boundary condition. The upper face of the specimen was displaced to produce a stretch of $\lambda = 2$. The material properties were defined through hyperelastic behavior, inputting the stress-strain data from a uniaxial tension test of a pure (no voids) elastomer specimen (no pre-cut) to determine the coefficients for the incompressible Mooney-Rivlin constitutive model ($U = C_{10}(\overline{I_1} - 3) + C_{01}(\overline{I_2} - 3)$), which gave C10 = 0.01134, and C01 = 0.0001766.

Mechanical testing:

All testing was conducted on an Instron 5943 system using a displacement control loading mode. The specimens were glued into "pure-shear" geometry grips with Loctite gel superglue, and a 25.4 mm pre-cut was made at the mid-plane and left edge of the specimen with a fresh razorblade. Cross-head displacements were measured to calculate the stretch of the samples during testing. The videos indicated minimal slip between the grips and the specimens. The stretch at propagation was determined by time synchronizing the load-displacement and corresponding video footage during the experiments. Architected void specimens were tested at a stretch rate of 0.1 / minute, while the elastomer-bubble composite samples were tested at a stretch rate of 1 / minute.

3.5. Summary and conclusions

While Fracture resilience is a key characteristic in developing effective elastomer components in applications. While conventional composites employ hard and stiff inclusions to improve mechanical properties, we find that the opposite approach (introducing infinitely-compliant voids) leads to improvements in mechanical performance in "flawed" silicone elastomers, i.e., specimens with cracks, notches, or any other features that cause inhomogeneous deformation. Specifically, we demonstrate that voids introduced into pre-cut silicone elastomer specimens locally "weaken" the specimen, which intriguingly enhances its overall resistance to rupture. We detail two methods of introducing voids (producing extended interconnected architected voids and discrete spherical bubbles) that disrupt crack propagation, thereby increasing the effective strength, stretchability, and energy dissipation during fracture of pre-cut specimens. We also establish that the resistance to rupture (in terms of total energy dissipation) appears to scale linearly with the volume fraction of discontinuous voids. Our findings also suggest that the effectiveness of fracture resilience depends on void shape/connectivity. Future work should build upon these studies to model and develop various void geometries and layouts that optimize energy dissipation and effective fracture resistance of void-elastomer composites.

4. FINITE ELEMENT ANALYSIS OF FLEXIBLE AND STRETCHABLE ELECTRONICS*

4.1. Flexible, scalable, and bandgap-graded single crystalline perovskite photovoltaics

4.1.1. Introduction

With a set of unique optoelectronic properties (110-113), organic-inorganic halide perovskites (OIHPs) have become an important material family for photovoltaics. Compared to their well-studied polycrystalline (PC) counterpart (114), single crystal (SC) OIHPs have shown higher carrier transport efficiency and stability due to lower defect concentrations (115-117). However, challenges for SC OIHP photovoltaics remain in terms of material growth – no growth method has demonstrated simultaneous control over growth thickness and area, or growth of a SC with composition gradient (115, 118), yet these are closely tied to photovoltaic performance. For optimal charge

*Reprinted with permission from "Flexible and lightweight devices for wireless multi-color optogenetic experiments controllable via commercial cell phones" Philipp Mayer, Nandhini Sivakumar, Michael Pritz, Matjia Varga, Andreas Mehmann, Seunghyun Lee, Alfredo Salvatore, Michele Magno, Matt Pharr, Helge C. Johannssen, Gerhard Troester, Hanns Ulrich Zeihofer and Giovanni Antonio Salvatore, 2019. *Frontiers in Neuroscience*, Vol. 13, no. 819, Copyright 2019 by Mayer, Sivakumar, Pritz, Varga, Mehmann, Lee, Salvatore, Magno, Pharr, Johannssen, Troester, Zeilhofer and Salvatore.
*Reprinted with permission from "Stretchable ultrasonic transducer arrays for three-dimensional imaging on complex surfaces" by Hongjie Hu, Xuan Zhu, Chonghe Wang, Lin Zhang, Xiaoshi Li, Seunghyun Lee, Zhenlong Huang, Ruimin Chen, Zeyu Chen, Chunfeng Wang, Yue Gu, Yimu Chen, Yusheng Lei, Tianjiao Zhang, NamHeon Kim, Yuxuan Guo, Yue Teng, Wenbo Zhou, Yang Li, Akihiro Nomoto, Simone Sternini, Qifa Zhou, Matt Pharr, Francesco Lanza di Scalea, Sheng Xu, 2018. Science Advances,Vol.4, no.3, eaar3979, Copyright 2018 The Authors, some rights reserved; exclusive licensee American Association for the Advancement of Science.

carrier collection efficiency, a film needs to be sufficiently thin (119); for practical device integration, the thin film needs to be grown over a reasonably large area. So far, attempts to control the crystal dimensions, such as mechanical cutting (120), roll-imprinting (117), and space confinement (115, 121), either lack control in both the thickness and area, or have strict substrate condition requirements. More importantly, none of the current growth methods have achieved composition gradient, and therefore, graded bandgap in OIHP crystals, either SC or PC form (122), despite its potential advantage in maximizing light absorption and enhancing carrier collection efficiency.

In this section we report finite element analysis (FEA) of SC OIHPs with precise control over the film thickness, area, and composition gradient on arbitrary substrates. We also implemented a neutral mechanical plane (NMP) design to enhance the flexibility of SC-OIHPs. These results are compared to our collaborator's experimental studies of these systems.

4.1.2. Neutral mechanical plane (NMP) calculation

Controlling the SC OIHP thin film thickness can not only optimize the carrier collection efficiency, but also tailor the mechanical properties of OIHP materials. So far, there have been no reports on SC OIHP thin film based flexible devices because of the fragility of the material, despite the promise for integration with non-planar surfaces such as buildings, vehicles, and humans (123, 124). For a thin film of a general material:

$$\sigma_{st} = \frac{E \cdot h}{2R}$$

where σ_{st} is the mechanical strength of the material, E is the Young's modulus, h is the thickness, and R is the bending radius (125). The minimal bending radius achievable without mechanical failure is proportional to the film thickness. Thus, reducing the film thickness offers clear benefits in flexibility. Further enhancement in the device flexibility is achieved by placing the film on the neutral mechanical plane (NMP) of the device: we sandwich the SC $MAPbI_3$ thin film between two strain-relieving polymer layers. With such a design, the minimal bending radius for a 2 μm thick SC film is 2.5 mm (Figure 4.1B), which has never been achieved by any other means.

In mechanics, the NMP is defined as a conceptual plane within a beam or cantilever. When loaded by a bending force, the beam bends so that the inner surface is in compression and the outer surface is in tension. The neutral plane is the surface within the beam between these zones, where the material of the beam is not under stress, either compression or tension. Therefore, if a material can have a sufficiently thin thickness and can be balanced near the NMP, the generated strain in the material will be effectively released to close to zero, which provides a possible approach for rendering the brittle SC OIHP as flexible (Figure 4.1A left). In order to design such a structure, we use a standard 1D beam bending equation to provide guidelines for this system (Figure 4.1A right) (126):

$$h = \frac{d_1E_1A_1 + d_2E_2A_2 + d_3E_3A_3}{E_1A_1 + E_2A_2 + E_3A_3}$$

where h is the distance from the bottom side of the structure to the neutral plane, d is the distance from the bottom side to the middle plane of each individual layer, E is the

Young's Modulus, and A is the cross-sectional area. In this study, the modulus and thickness for the middle SC $MAPbI_3$ and bottom commercial ITO/PET are known: the thickness of the middle SC $MAPbI_3$ is 2 μm, and the modulus is 14 GPa; the thickness of the bottom ITO/PET is 70 μm and the modulus is 2 GPa. Therefore, the first thing is to design a top layer with suitable modulus and thickness to locate the neutral plane close to the middle of the perovskite layer. For flexible or wearable devices, an overall small thickness is preferred for better conformability with the nonplanar surfaces. Therefore, a thin top layer in the NMP structure is highly desired, which means a similar or larger modulus of the top layer than that of the PET/ITO is necessary. Here, we use the mixture of PDMS and SU8 to form such a top layer. The purpose of mixing SU8 is to largely enhance the PDMS modulus. The resultant modulus of the SU8/PDMS is around 2.5 GPa. Therefore, the calculated thickness for the top SU8/PDMS layer is around 62 μm. However, even though the thickness can be calculated from the above equation, there will sometimes be discrepancies between experiments and simulations from the 1D model, due to Poisson effects and the large deformations of the composite that are not accounted for in the simplified 1D bending equation. Therefore, a further 3-D mechanical response needs to be analyzed as well to study the design better.

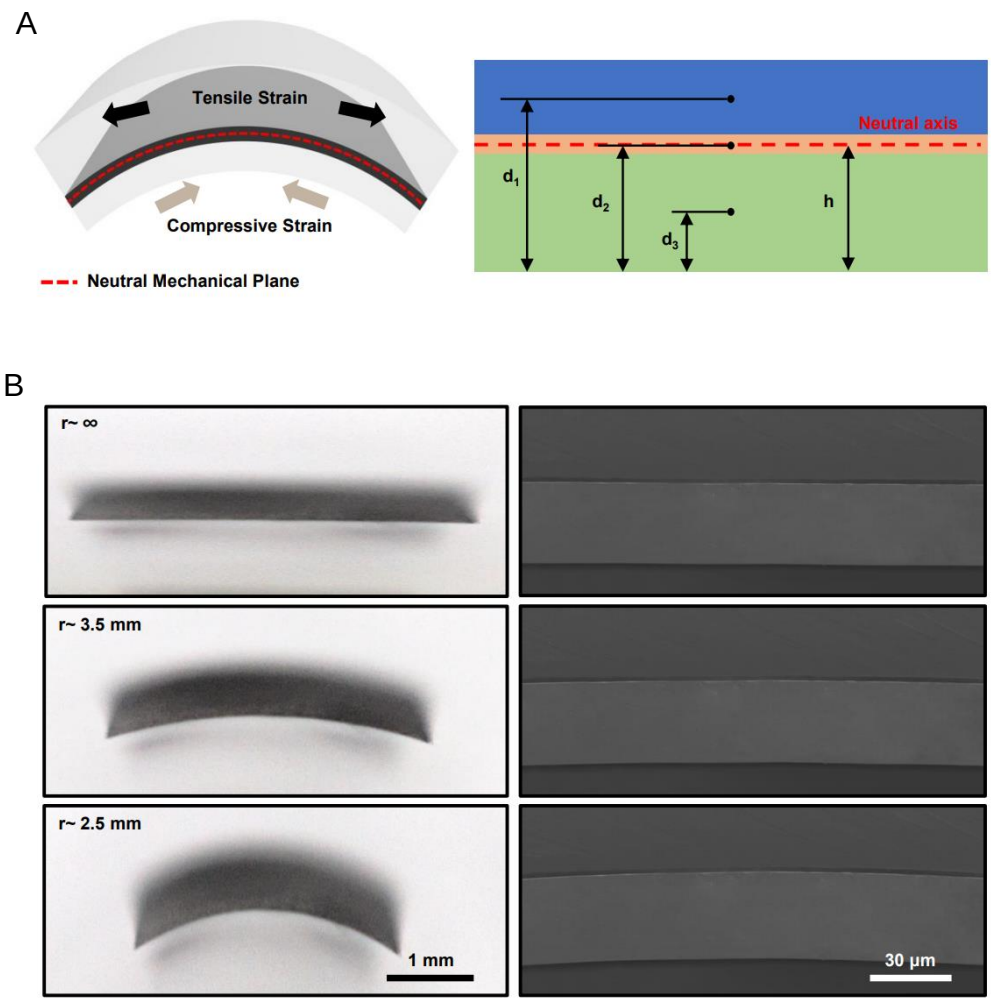

Figure 4.1 The neutral mechanical plane design. (A) Schematics for calculating the position of the neutral mechanical plane. The SU8/PDMS top layer is critical for minimizing the strain in the SC OIHP layer. (B) Optical (left) and SEM (right) images under different bending radii of curvature. The SC OIHP (thickness 2 µm) can be successfully bent to r ~ 2.5 mm without damage.

4.1.3. FEA modeling

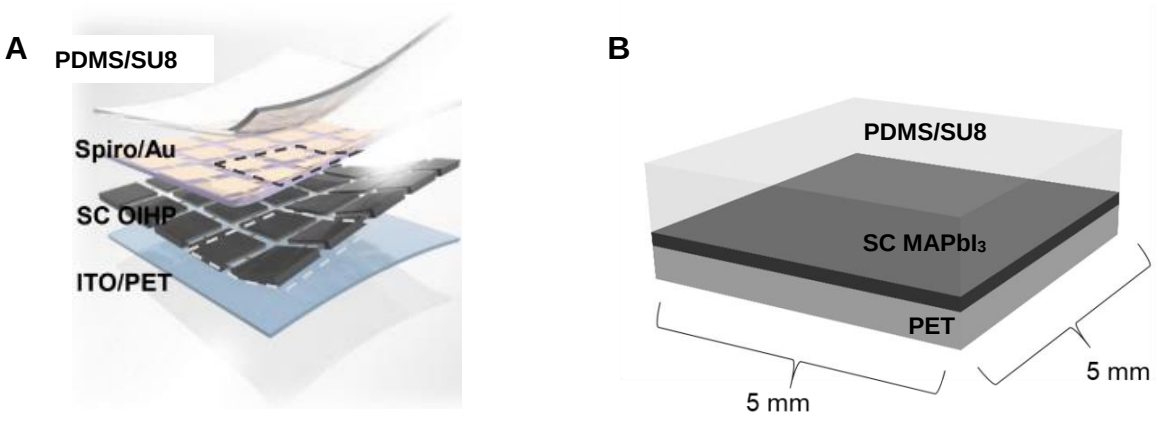

Figure 4.2 (A) Exploded view of the devices and (B) simplified model for ABAQUS simulation.

Mechanical simulations were performed by a commercial software package ABAQUS to model the mechanical response of the SC OIHP devices. The composite layer (PET-$MAPbI_3$-SU8/PDMS sandwich structure) consisted of an 8-node linear brick (C3D8H). The simulation implements values of the elastic modulus of SU8/PDMS, SC $MAPbI_3$, and PET of 2.5 GPa, 14 GPa, and 2 GPa, respectively. Other device component materials, including ITO, SnO_2, and Spiro-MeOTAD were neglected in the simulation due to their similar Young's moduli compared with $MAPbI_3$ and negligible thickness compared with the strain-relieving layers, as to simplify the model (Figure 4.2B). The simulation implements linear elastic constitutive models for each constituent but included non-linear geometric effects (finite deformation) to enable large out of plane deformation.

4.1.4. Results

We use finite element analysis to understand the mechanical behavior of the bent OIHP thin film. Figure 4.3 shows simulated strain distribution in the PET-$MAPbI_3$-SU8/PDMS sandwich structure (left) as well as the perovskite layer extracted from the structure (right) when they are bent to radii of 2.5 mm, 3mm, 3.5 mm, 4.0 mm, and infinity (no bending). The highest value of the maximum principal stress was found to exist near the edge of perovskite layer due to Poisson effects. When the radius of curvature of perovskite layer was ~2.5 mm (the critical radius of curvature to cause cracks observed in experiments), the maximum principal stress in tension is ~80 MPa. . The strain away from the edge of the SC $MAPbI_3$ is less than 0.25%; the edge is where the maximum strain occurs, at around ~0.36%, which is close to the fracture strain of the SC $MAPbI_3$ (118, 127).

We can compare these simulation results to experimental observations performed by our collaborators. Mechanical flexibility tests clearly show significant differences between the bare SC $MAPbI_3$ thin films and the sandwich structure with the NMP design (Figure 4.4). For both, a smaller thickness leads to a smaller achievable bending radius. Moreover, the NMP design enables significantly higher flexibility compared to the bare film. PL mapping images of a ~2 μm SC $MAPbI_3$ film with the NMP design under different bending radii show that cracks begin to appear when the bending radius reaches ~2.5 mm (Figure 4.4 right).

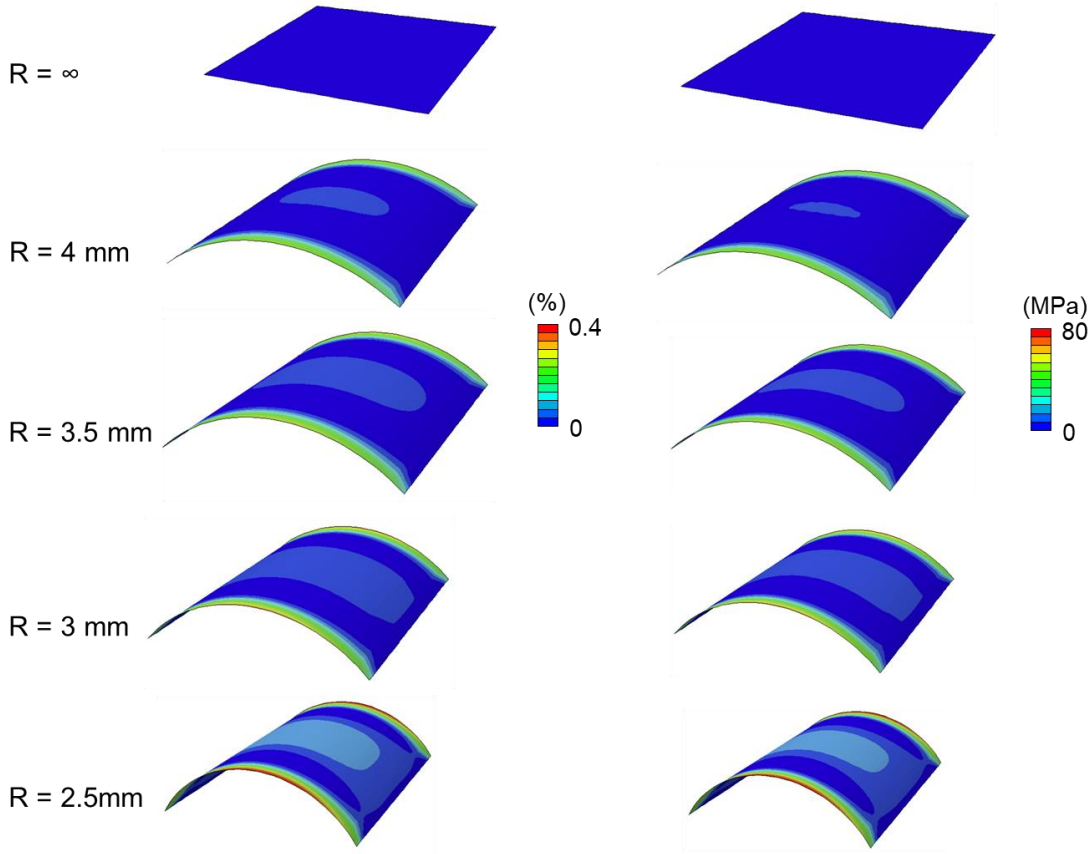

Figure 4.3 Stress and strain distribution from bending simulations of a flexible SC OIHP device under different bending radii. The results in the left panel show the strain distribution of the extracted perovskite layer only (with other layers hidden) and the right panel shows corresponding stress distribution. At a bending radius of 2.5 mm, most of the regions of the perovskite layer have a principal strain of less than 0.25%. The edge areas show a principal strain of around 0.36%, which is close to the failure strain of this material and a maximum principal stress of 80 MPa.

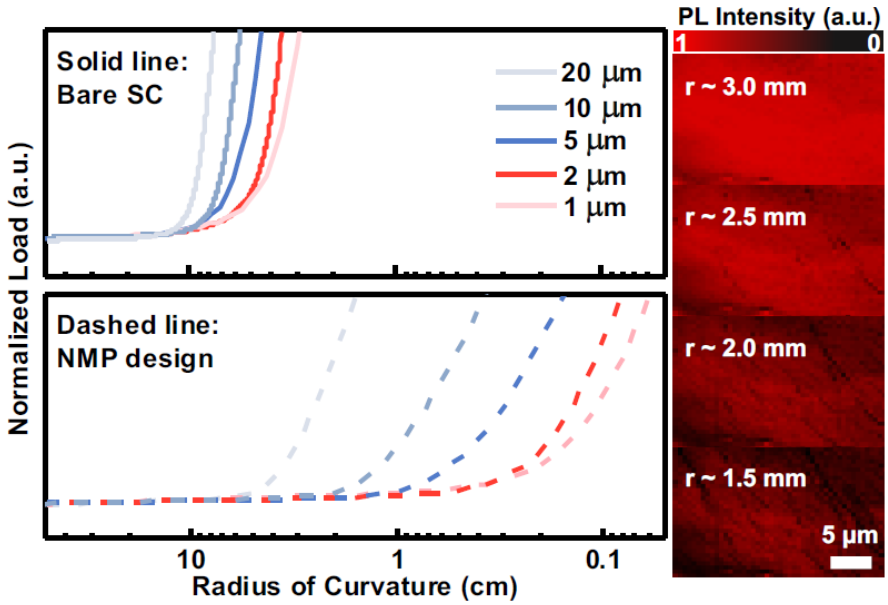

Figure 4.4 Flexibility test results of SC OIHP with different film thicknesses. A smaller thickness leads to a smaller bending radius. The NMP design results in a significant enhancement in flexibility compared with the bare film. PL images on the right show morphologies and cracks of the film at different bending radii.

The highest value of the strain in the simulations is found to be near the edge of SC OIHP layer due to the Poisson effect, which can provide an estimation of the failure strain of this kind of OIHP materials (Figure 4.1B). However, even though the simulation results show that the maximum bending curvature to keep that material safe is around 2.5 mm, experimental results indicate that the cracks just begin to appear at that bending level. Slight discrepancies are believed to be reasonable considering the difference between the experiment and the assumptions used in the simulations, which may stem from one or more of the following:

1. The boundary condition: in the 3-D simulation, all layers are ideally attached. There is no slip and no de-bonding during the simulation, which may occur in the

experiments.

2. Input force (moment): unlike in the experiments, a moment is applied to the device in the simulation (for simplicity). As such, the resulting deformation in the simulation does not have a constant radius of curvature along the θ direction.

3. Material parameters: may be different in the fabricated device (e.g., modulus of the perovskite), as compared to the values we used in the simulations. Likewise, the critical strain to cause fracture may be different from what is reported in literature and the actual material used in the experiments.

4.2. Flexible and lightweight devices for wireless multi-color optogenetic experiments

4.2.1. Introduction

Optogenetics provide a potential alternative approach to the treatment of chronic pain, in which complex pathology often hampers efficacy of standard pharmacological approaches. Optogenetic devices implanted on top of a peripheral nerve or on the dorsal surface of the spinal cord allow the manipulation of excitatory input from peripheral nociceptors, or of central neurons or fiber tracts located superficially in the spinal cord. Therapeutic application and use in sophisticated rodent behavioral paradigms of analgesia would benefit from fully implantable and durable wireless electronic systems, ideally carrying more than one light source for inhibition/excitation of neurons that can be individually controlled on an on demand basis (128-130). Conventional printed electronics boards are rigid and bulky and often protrude several millimeters under the skin. Their mechanical format hardly adapts to the soft mechanics of the tissues and can induce damage during prolonged use. Moreover, the aforementioned mismatch precludes device immobilization and, consequently, the efficient delivery of the optical stimuli in the region of interest. Recent advances in material science and micro-technology have enabled the integration of high performance and miniaturized electronic chips on soft polymeric substrates so as to confer physical properties, such as thickness and Young's

modulus, that resemble those of biotissues (131-133). Such devices can laminate onto the spinal cord, operate in wireless mode, and provide the desired optical power (1–20 mW/mm^2) for optogenetics (133, 134). In this section, we provide finite element analysis simulations of battery free, flexible, and lightweight devices, equipped with one or two miniaturized LEDs powered by resonant magnetic coupling that can be individually controlled in real time. FEA is essential to provide a practical design and to estimate the mechanical properties and durability of complex composite structures for biomedical applications.

4.2.2. Design of the optogenetic device

The device (of our collaborators) incorporates various functional layers (copper metallization of ~18 μm), barrier films [polyimide and poly(dimethylsiloxane)], and active components (surface-mounted chips and LEDs) fabricated on a substrate of polyimide (25 μm thickness) in a planar geometry to facilitate processing by conventional manufacturing techniques (Figure 4.5A). All metal traces include encapsulating layers of polyimide above and below to physically and electrically insulate the copper and to place it near the neutral mechanical plane (Figure 4.5B). The rectangular loop antenna (outer dimensions of 14 mm × 19 mm) exploits 5 turns of copper lines with a pitch of 250 μm and widths and thicknesses of ~250 μm and 18 μm, respectively.

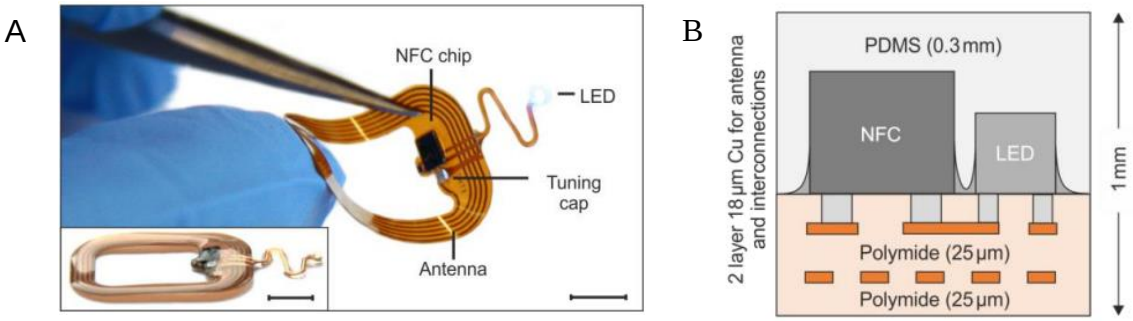

Figure 4.5 (A) Device operating during bending tests. The antenna is 1.9 cm × 1.4 cm large and it is formed by 5 Cu turns with a thickness of 18 µm and a pitch of 250 µm. The interconnection between the electronics and the LED has an open and S-shaped design which enables out-of-plane displacement during implantation (scale bar 5 mm). The inset shows a side-view of the device (scale bar 5 mm). (B) Schematic of the layout through the thickness.

4.2.3. FEA modeling

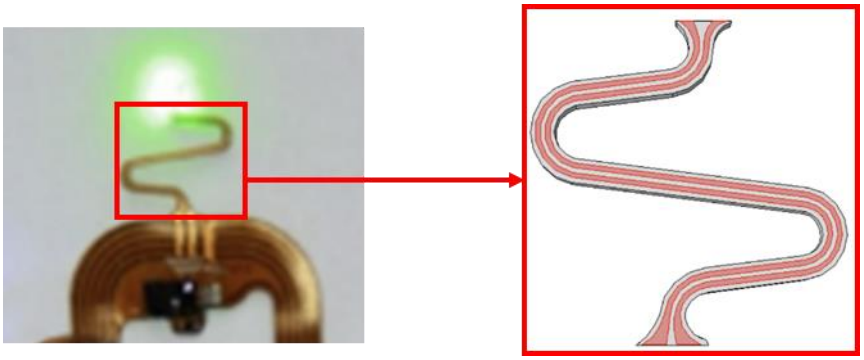

Figure 4.6 Simplified model for FEA simulation. The red region in the right image consists of PDMS, PI, and copper composites.

The S-shaped interconnection is vulnerable due to repeated tension, bending and twisting during implantation and operation. Large deformation results in permanent deformation of this interconnection. The commercial software package ABAQUS

allowed for simulating the mechanical response of interconnection of the device between the antenna and the LED. Figure 4.6 shows a simplified version of the region for simulation. The red region in the right image indicates a composite layer (PDMS, Cu, and PI), which was modeled with 6-node linear triangular prism (C3D6) elements. The simulations implemented values of the elastic modulus of PDMS, PI, and Cu of 0.5, 2300, and 130000 MPa, respectively. The simulations also implemented linear elastic constitutive models for each constituent but included non-linear geometric effects (finite deformation) to enable large out-of-plane deformation. Additionally, to find when plastic deformation occurred in the composite, a yield strength of Cu of 110 MPa was assumed, as a representative value that we have measured by tensile testing with a 1 kN load cell (Instron 5965) (results not included here).

4.2.4. Results

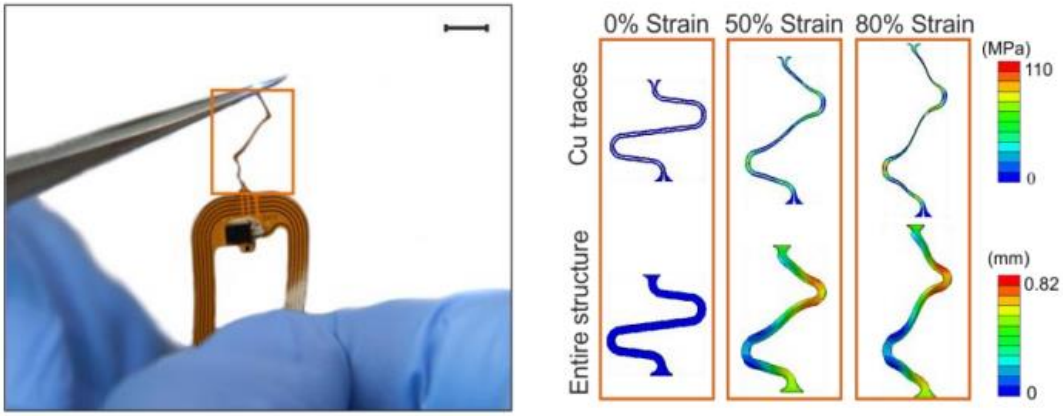

Figure 4.7 Stress-strain response of the interconnections between the LED and the antenna (scale bar 5 mm). In the right set of images, the top row shows the maximum principal in-plane stress in the Cu. The bottom row shows the out of plane displacement of the entire structure. The simulation results show that the Cu layer of the interconnect did not yield until a level of ~80% global strain (for a yield strength of Cu of 110 MPa).

Finite element simulations of the mechanical response during stretching of the interconnection between the antenna and the LED provide a quantitative analysis of the stress in the structure. The results, shown in Figure 4.7, indicate that stress-concentrating regions exist at the ends (i.e., near the antenna and LED) and at the bends (i.e., near the arcs). To improve this design, those regions should be addressed first. Generally, decreasing the in-plane width of the serpentine relative to the in-plane length and/or decreasing the thickness of the layers will improve stretchability by enabling more out-of-plane deformation at lower corresponding stresses. Additionally, to find when plastic deformation occurred in the composite, a yield strength of Cu of 110 MPa was considered as a representative value (135). Using this value, the finite element simulations show that the Cu layer of the interconnect will not yield until a level of ~80% global strain. As such, beyond its mere stretchability, we also expect that this design will enable repeated stretching, twisting, etc. without fatigue failure, since plastic deformation of the Cu traces will not occur unless global strains exceed 80% (according to the simulations). These miniaturized dimensions, the lightweight construction (~100 mg), and the mechanical flexibility represent attractive characteristics as a versatile platform for wireless delivery of light to organs and tissues in freely moving animals.

4.3. FEA simulation of stretchable ultrasonic transducer arrays

4.3.1. Introduction

Ultrasound imaging technologies have been widely used to visualize internal discontinuities in objects for nondestructive evaluation, structural health monitoring, and medical diagnosis because of their noninvasiveness, high accuracy, great sensitivity, and strong penetration capabilities (136, 137). Ultrasound probes with flat bases that have rigid probes cannot achieve a solid interfacial contact with irregular nonplanar surfaces. In addition, these rigid probes cannot be applied to hard-to-reach locations such as small cavities and slits. At the same time, the stress concentrations present at the geometrical discontinuities of load-bearing objects make these regions particularly prone to defects (138). In case of flexible probes, they can be applied only to developable surfaces (such as cylindrical surfaces), i.e., not to non-developable surfaces (such as spherical surfaces). In addition, the flexible conductive interconnections in flexible probes are subject to breaking or debonding when repeatedly used because being flexible is insufficient to accommodate the sophisticated and time-dynamic motion of the electrodes and the device during the measurements (139). To overcome these limitations, a low-profile membrane-based stretchable ultrasonic probe was fabricated by our collaborators. The probe exploits an array of thin and high-performance 1-3 piezoelectric composites as transducers, multilayered serpentine metal traces as electrical interconnects, and low-modulus elastomer membranes as encapsulation materials. We performed simulations of

the mechanical response of probe arrays to predict stretch limitations as to avoid material failure.

4.3.2. Design of the stretchable ultrasonic arrays

A schematic representation of the device structure is shown in Figure 4.8A. The piezoelectric transducers are arranged in a 10 × 10 array, connected by an island-bridge structured matrix. Each island hosts a rigid element. The wavy bridges can unfold to accommodate the externally applied strain, with limited strain in the components themselves. Therefore, the matrix is rigid locally but soft globally. Each element in the array is individually addressable. The soft probe can consequently reconstruct the target morphology in multi-section images. Figure 4.8B shows the exploded view of one element. Both the substrate and superstrate are silicone elastomer thin films, whose low modulus (~70 kPa) and large stretchability (~900%) offer an extremely compliant platform to accommodate a diverse class of building blocks, such as piezoelectric elements, metal interconnects, backing layers, and solder paste. The thickness of the elastomer substrate and superstrate is 15 mm to provide both high acoustic performance (140) and mechanical robustness of the device. The islands and bridges are patterned bilayers of Cu (20 mm)/polyimide (PI; 2 mm). The PI layer greatly enhances the bonding strength between the Cu and the elastomer.

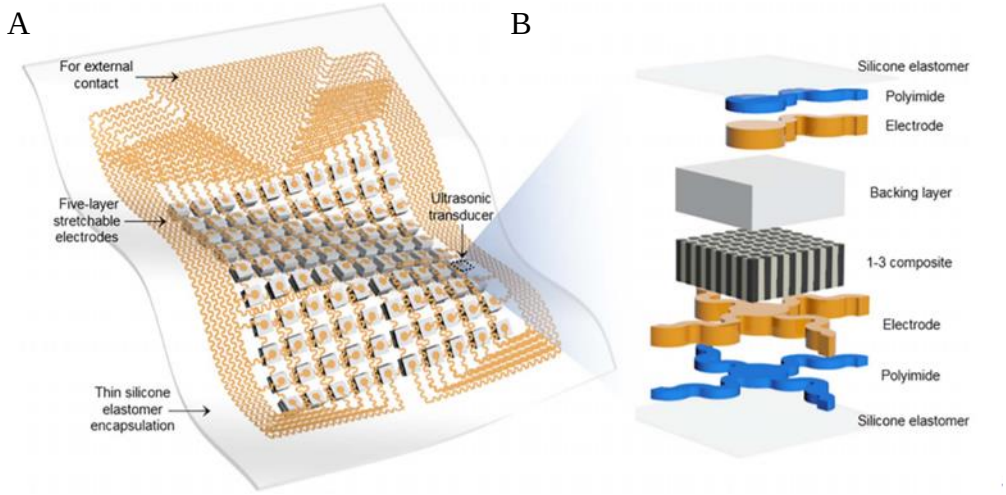

Figure 4.8 Schematics of the stretchable ultrasonic transducer array. (A) 10x10 ultrasound sensor array. (B) Composite structure of a sensor element.

4.3.3. FEA modeling

Finite element analysis (FEA) was performed to calculate the mechanical response of the ultrasonic transducer arrays using the commercial software ABAQUS. For 3D FEA, 2 x 2 sensor arrays in critical locations are selected. The main goal of the FEA is to predict mechanical failure of serpentine-structured copper layers under biaxial tension. Ultrasonic sensor array layers are simplified as a polyimide, copper, and Ecoflex composite for the simulation as shown in Figure 4.9. The composite layer (Ecoflex, Cu, and PI) consisted of hybrid hexahedral elements (C3D8H). The simulations used values of the elastic moduli of Ecoflex, PI, and Cu of 0.06, 2300, and 41,500 MPa, respectively. To obtain the yield strength value of the Cu, four pieces of Cu slides with a high aspect ratio (width, 4.18 mm; thickness, 0.02 mm; length, 18.78 mm) were measured by tensile

testing. The testing rate was 1% tensile strain per minute, and the load cell was 1 kN (Instron 5965). The stress-strain curves were obtained from which the yield strength value of Cu slides (187 MPa) was extracted and used in the simulations. To predict the stretch limitation of the device under biaxial tension, displacement boundary conditions were applied at the four edges of composite layer from 10% to 60% strain.

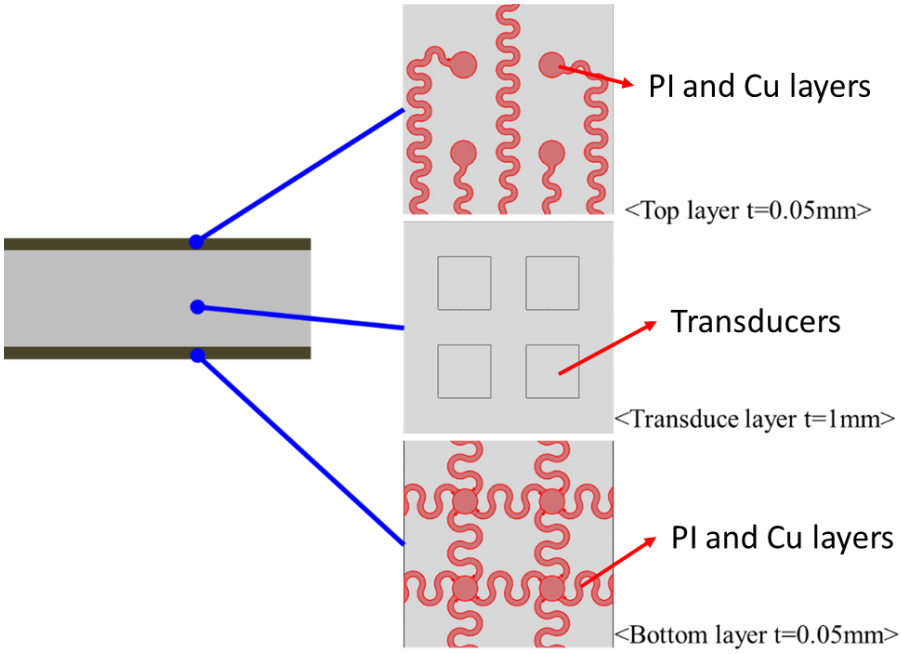

Figure 4.9 Simplified structure of 2x2 ultrasound transducer array for FEA simulation. The red region consists of a PI and Cu composite. Displacement boundary conditions are applied along all four lateral edges of the device.

4.3.4. Results

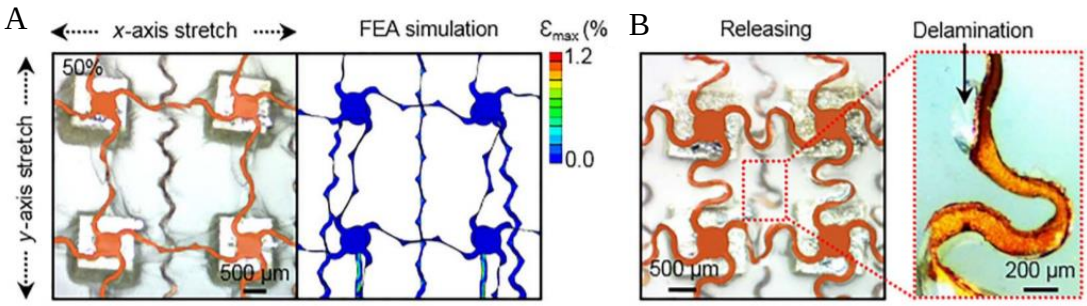

Figure 4.10 (A) Optical image (left) and corresponding finite element analysis (FEA) simulation (right) of a 2 × 2 array under 50% biaxial tensile strain, showing its excellent stretchability. The local strain level (maximum principal strain) in the interconnects is indicated by the color scale. (B) Optical image after releasing the biaxial strain of 50%. The zoomed-in image highlights plastic deformation and local delamination of the interconnects upon loading/unloading.

Mechanical properties of conductive interconnects are critical for flexible and stretchable devices (141-143). Experimental results from biaxial stretching of the layered structures of serpentines between 0 and 50% and corresponding 3D finite element analysis (FEA) are shown in Figure 4.10A and B. A 2 × 2 array of elements is selected for visualization of the key mechanics involved. Under tensile loading, the horseshoe serpentines undergo an in-plane unraveling process and out-of-plane rotation and twisting, both of which mitigate the level of strain in the islands themselves (47, 144). Specifically, in these ultrasound arrays, 50% biaxial stretching produces a maximum of only ~1.2% tensile strain in the Cu interconnects, as shown in the FEA image of Figure 4.10A. After the serpentines have fully unraveled (that is, finished rotating in-plane), the tensile strain in the Cu interconnects increases rapidly, thus defining the stretching limit of the serpentines (47, 145), which is between ~50 and 60% in this case. Going beyond

this limit will lead to fracture of the serpentines. In addition, for the reliability of these devices, they must be capable of sustaining mechanical integrity upon repetitive loading.

Figure 4.11 shows the stress distributions at 10% - 50% applied strain. Based on the yield strength of copper, the simulations show an elastic stretchability of around 30%. As a result, mechanical failure occurred at small strains compared to the intrinsic stretchability of as-fabricated silicone elastomer (~900%). After ~ 30% biaxial strain, the copper films start to deform plastically, and ~55% biaxial strain produces mechanical failure in the serpentine copper film layer.

In metals such as Cu, cycling into the plastic regime will cause permanent deformation of the interconnects, which may affect device performance or may eventually produce fatigue cracks (49). According to both the simulations and the experiments, ~30 to 40% biaxial stretching produces irreversible deformation in the serpentines upon releasing (Figure 4.11) and partial delamination between the serpentines and the silicone elastomer, as highlighted in Figure 4.10B. However, below 30 to 40% biaxial stretching, mechanical integrity is maintained.

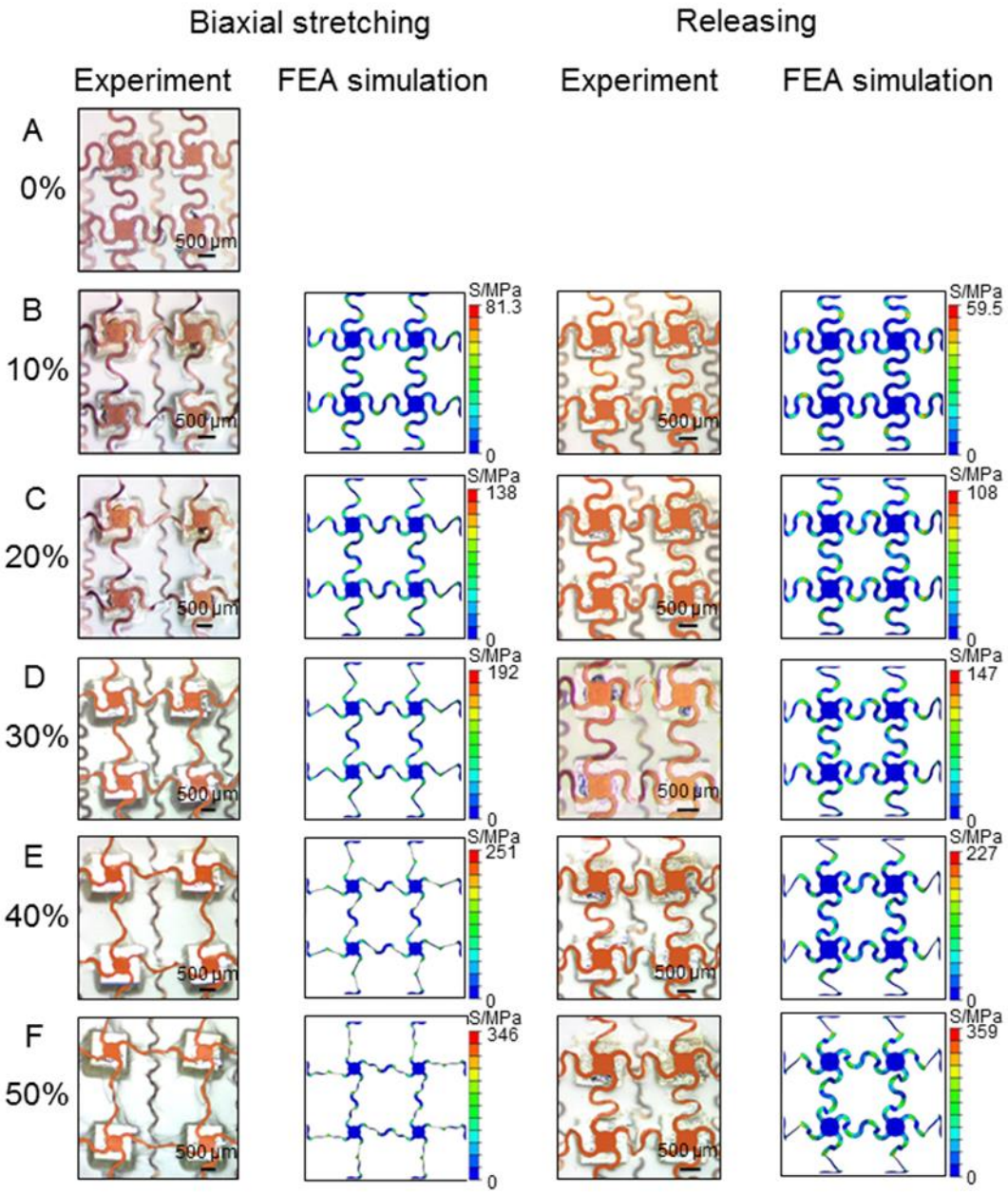

Figure 4.11 Experimental and simulation results of a small array under biaxial tensile strain. Good agreement exists between the experiments and simulations. The results show an elastic stretchability of ~30%.

4.4. Conclusion and summary

In this chapter, finite element analyses were performed to analyze mechanical behavior and to visualize stress and strain field of flexible and stretchable devices. In section 4.1 shows numerical analysis results of a photovoltaic device that consists of an organic photovoltaic perovskite layer. Neutral mechanical plane calculation and FEA results maximize the flexibility. The computed maximum bending curvature to keep the materials from mechanical degradation is around 2.5 mm, which is quite similar to the maximum bending curvature observed in experiments. In Section 4.2, we provide numerical simulations of thin, wireless, and mechanically flexible optoelectronic devices for biological implants capable of controlling the activity of subsets of neurons and nerve fibers in vivo. The finite element simulations demonstrate that the S-shaped Cu layer of the interconnect will not yield until a level of ~80% globally applied strain. Thus, unless global strains are expected to exceed 80% during implantation or operation, this device is suitable to implant into the freely moving animals.

Finally in Section 4.3, we provide finite element analysis (FEA) results of a simplified model of an ultrasound sensor array that consists of a piezoelectric material, polyimide (PI), and copper thin film serpentine structure, all encapsulated by a silicone elastomer. The simulations provide stretch limitations of serpentine structures of copper under biaxial loading and unloading conditions, as to provide guidance toward safe operation of the devices.

5. TIME-DEPENDENT MECHANICAL BEHAVIOR OF SWEET SORGHUM STEMS*

5.1. Introduction

Grasses represent the most productive and widely grown crop family across the globe but are susceptible to structural failure (lodging) under mechanical loading (146, 147). Stem lodging is a complex physical process that significantly reduces yield and quality in many of the cereal grasses (e.g., maize, rice, sorghum, wheat, etc.) (148). Despite the economic significance of stem lodging, the mechanisms that contribute to structural failure in grass stems remain poorly understood. Quantitative methods including histochemical approaches, crushing strength measurements, rind penetrometry, and bending tests (149-157) have been applied to understand stem mechanical behavior. However, these methods may be insufficient to fully understand the deformation processes of stem structures (158, 159). A better understanding of the parameters that produce the observed mechanical behavior of the cereal crops is critical to increase agricultural productivity as well as to provide fundamental knowledge of the mechanisms of stem lodging.

Sorghum (Sorghum bicolor (L.) Moench) is a useful model plant for studying stem structural failure because of its tremendous variation in height, stem thickness, tillering, stem composition, and end-use (food, forage, energy, fiber, building material,

*Reprinted with permission from "Time-dependent mechanical behavior of sweet sorghum stems" Seunghyun Lee, Omid Zargar, Carl Reiser, Qing Li, Anastasia Muliana, Scott A. Finlayson, Francisco E. Gomez, Matt Pharr, 2020. *Journal of the Mechanical Behavior of Biomedical Materials*, Vol. 106, 10373,

etc.), which is largely a result of disruptive selection (160-163). This diversity in attributes provides a key advantage in terms of probing which factors most affect mechanical stability and structural failure in the cereal grasses. Sorghum, like all cereal crops, often mechanically fails because of wind pressure on the stem. This failure is a consequence of weak stems, which are either genetically inherited or caused by other factors such as pathogens (155, 164-166). In response, plants have adapted unique stem anatomical, morphological, and mechanical properties to maintain structural integrity when subjected to dynamic loadings (167, 168). As such, a complete time-dependent understanding of stem biomechanical properties is necessary to explain how plants can withstand stresses from wind. In turn, such understanding can be used by modelers to determine the mechanical stability of stems under various conditions (e.g., wind speed) as well as by plant breeders to potentially select for traits that confer greater mechanical stability (lodging resistant variants).

Previous studies have uncovered both genetic and spatial variation of sorghum mechanical properties, e.g., among genotypes and among both nodes and internodes at different positions (21, 169-171). A recent study implemented a three-point bending test and found that sorghum stems exhibited a significantly lower elastic modulus, strength, and flexural rigidity at the internodes, as compared to the nodes (170). This spatial variation of properties may explain why sorghum stem lodging in the field nearly always occurs at the internodes, as has also been observed in other cereal crops (172, 173). More lodging-resistant sorghum genotypes demonstrated stronger and more flexible (low flexural rigidity) stems with a lower elastic modulus (170). Further investigation of

stem failure, beyond simply determining the elastic modulus and ultimate strength is required to develop a better understanding of the mechanical behavior of grass stems. In particular, all studies to date treat sorghum stems as linearly elastic, which does not represent a realistic mechanical response of the stems. Instead, plants are composite materials, consisting of various microstructural constituents at multiple length scales. At larger scales sorghum stems can be distinguished by their sclerenchymatous tissue (outer skin or epidermis and rind comprised of several sub-epidermal cell layers) and parenchymatous tissue (pith, consisting of vascular bundles and soft tissues). Green (living) sorghum has a high-water content, which may lead to pronounced time-dependent behavior associated with water viscosity. Mechanical pressures can cause water migration through the stem tissues, a time-dependent process known as poroelasticity. In addition to the high water content, the components of the plants themselves may exhibit viscoelastic behavior, a time-dependent response due to rearrangement of macromolecular networks, as they are based on polymeric building blocks (i.e. cellulose, hemicellulose, and lignin). Overall, the time-dependent behavior of sorghum stems can influence lodging and it is important to characterize this behavior to gain a comprehensive understanding of sorghum biomechanics. Thus, methods to quantify the mechanical behavior of stems requires tests that include a time component of testing (146).

The objective of this study was thus to uncover greater detail of the biomechanical behavior of sweet sorghum by investigating the full stress-strain behavior (i.e., beyond just the linear elastic regime) and time-dependent responses of stems and

pith under uniaxial loading. To do so, we selected the sweet sorghum Della cultivar, which was grown in a greenhouse in a controlled environment. In section 5.2 we conducted uniaxial compression tests under ramp loading on pith and stem internodes. Uniaxial compression creep tests of pith and stem were performed in section 5.3. The results demonstrate that all of the tested samples of sorghum exhibit pronounced time-dependent mechanical responses. We conclude by detailing the ramifications of such effects in the context of stem lodging.

5.2. Mechanical behavior under ramp compression tests

Uniaxial ramp compression tests at strain rates of 10%/min (slow) and 100%/min (fast) were performed to examine the mechanical behavior of the pith and stem of the Della genotype. Figure 5.2 shows the engineering stress-strain responses under these conditions, which indicate that the full intact stems are stiffer and stronger than their corresponding piths, as expected. For the pith specimens, the calculated initial slopes from these tests were 25.8 (±8.0) MPa for slow loading (10%/min) and 36.4 (±7.5) MPa for fast loading (100%/min). For the entire stems, the calculated initial slopes were 130.1 (±30.1) MPa for slow loading (10%/min) and 177.9 (±50.5) MPa for fast loading (100%/min). Unpaired t-tests were used to identify differences between the initial slopes at the two loading rates of the stems and piths separately with the significance level at $p \leq 0.05$. These results demonstrated a strong influence of loading rate on the biomechanical properties of Della sorghum ($p = 0.0176$ for the stem and $p = 0.0061$ for the pith), thereby demonstrating its pronounced rate/time-dependent effects.

As expected, the slower rate resulted in smaller slopes as more pronounced stress relaxation occurred due to the longer duration of loading. Deformation beyond the linear region further indicated strong rate effects. Under slow loading (10%/min), the pith showed a peak stress of 1.4 (±0.5) MPa at a strain of 14.1 (±6.7) %; under fast loading (100%/min), the pith showed a peak stress of 1.5 (±0.3) MPa at a strain of 6.2 (±1.4) %. The stress-strain responses of the pith specimens were highly nonlinear. Specifically, they demonstrated plateaus in stress between 14.1 (±6.7) - 67.1 (±5.9) % strain under slow loading (10%/min) and 6.2 (±1.4) - 66.9 (±6.6) % strain under fast loading (100%/min). These plateaus were followed by a rapid rise in stress at both loading rates. We surmise that this nonlinear deformation arose from continuous collapse of the cell walls (i.e., crushing), followed by densification at a relatively large strain. Evidence of water loss from the pith was observed near the sample on the compression platen after testing. Water drained from the pith specimens very soon after loading and continued as compressive loads increased.

Both the stem and pith of Della showed qualitatively similar mechanical behavior, but with the stems demonstrating higher strengths (Figure 5.2). Specifically, under slow loading (10%/min), the stems showed a peak stress of 3.3 (±0.3) MPa at a strain of 7.4 (±1.8) %; under fast loading (100%/min), the stems showed a peak stress 4.0 (±0.6) MPa at a strain of 5.9 (±1.4) %. The stress-strain responses of the stem specimens were again highly nonlinear. Specifically, they demonstrated plateaus in stress between 7.4 (±1.8) - 78.4 (±4.3) % strain under slow loading (10%/min) and 5.9

(±1.4) - 75.7 (±4.1) % strain under fast loading (100%/min). These plateaus were followed by a rapid rise in stress at both loading rates.

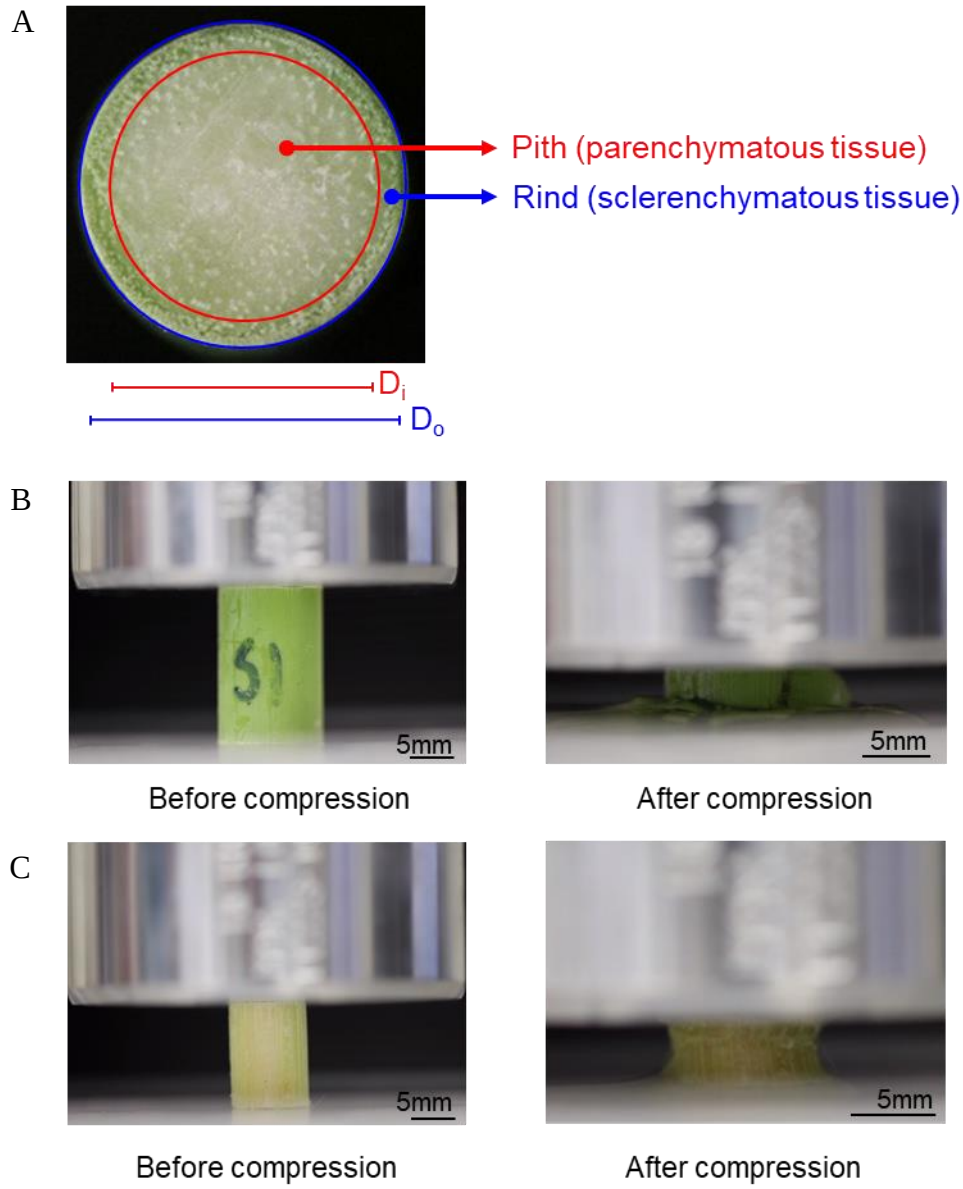

Figure 5.1 Representative photos of Della bioenergy sorghum. (A) Anatomical structure of a cross section of a Della stem. White dots correspond to vascular bundles. (B) Side view of a Della pith before and after compression testing. (C) Side view of a Della stem before and after compression testing.

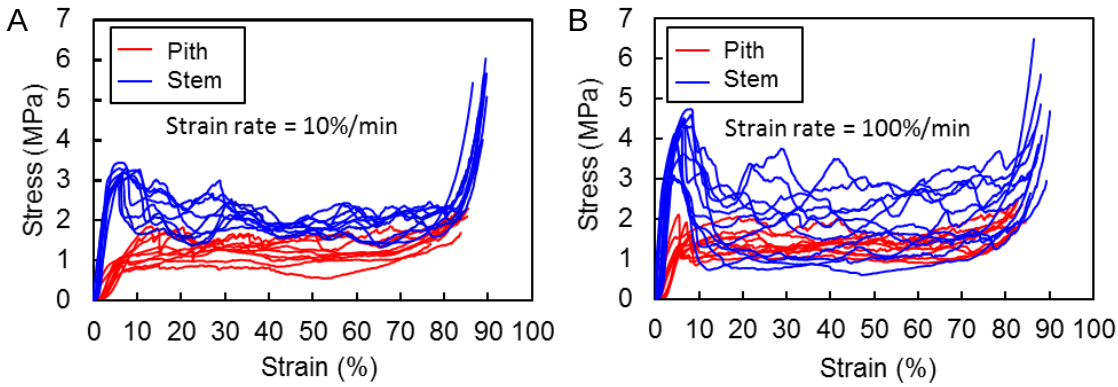

Figure 5.2 Stress-strain curves of uniaxial compression testing of Della pith and stems (A) at a strain rate of 10%/min; (B) at a strain rate of 100%/min.

The ultimate failure of the stems involved splitting between the rind and pith, followed by buckling and separation of the outer rind layer. For the pith specimen itself, failure likely involved breaking the vascular bundles and/or splitting the pith parenchyma accompanied by simultaneous water drainage of the sample (Figures 5.1B and 5.1C). Rind splitting and water drainage observed in experiments indicate that irreversible deformation occurs in the non-linear regime of the stress-strain response in both the pith and stem. This rind splitting is not recoverable and as such will produce irreversible deformation. Time correlating with the stress-strain response in Figure 5.2 indicates highly nonlinear behavior beyond this point.

5.3. Mechanical response under compression creep loading

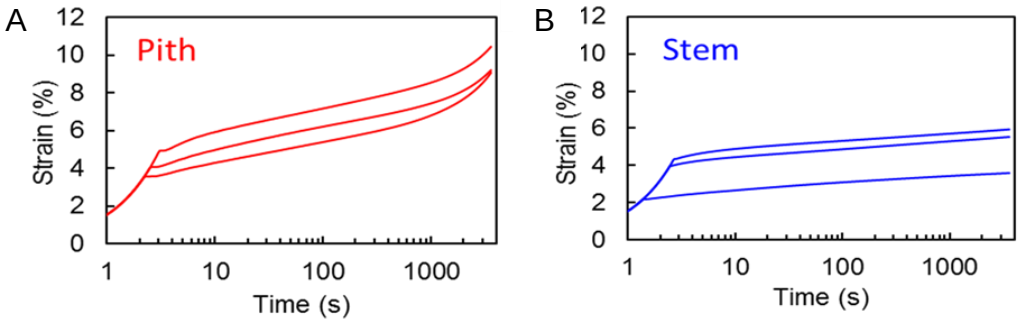

Figure 5.3 Creep tests: strain response during one hour under a static load. (a) Della stem; (b) Della pith

Stem failure in sorghum depends not only on the magnitude of loading but also on the rate and duration of loading (146). Variations in these parameters are typical of the way that the crop experiences wind loading in the field. Therefore, it is critical to determine both the quasi-static and dynamic mechanical properties of sorghum, which requires characterizing time-dependent properties. To this end, we have selected creep tests as they are particularly conducive to determining viscoelastic material parameters, e.g., for use in future modeling studies. Figure 5.3 shows representative plots from creep tests for pith and stem specimens under compression at ~50% of the strength as measured from compression ramp tests (i.e., from Figure 5.2). For the Della pith, the strain increased to 4.2 (±0.7) % during a ramp loading at strain rate of 100%/min, followed by a continuous evolution to 9.6 (±0.8) % after 1 hour under a constant load (Figure 5.3A). For the Della stem, the strain increased to 3.5 (±1.0) % from a ramp loading at strain rate of 100%/min, followed by a continuous slow evolution to 5.0 (±1.2) % after 1 hour under a constant load (Figure 3b). Although the specific values of

the strains in these tests varied, which may have depended on the characteristics of the specimens (e.g., number of vascular bundles, water content, etc.), all of the tested specimens demonstrated clear and significant time-dependent deformation under a constant load.

5.4. Discussion

This study used the sweet sorghum Della cultivar, which showed a minimal transition region between the rind and the pith and a relatively large region of pith (Figure 5.1). Its stems were significantly stiffer and stronger than the pith itself due to the presence of the rind (Figure 5.2). The rind is composed of high-density fiber bundles within the cell walls, which lead to stiffer and stronger tissues compared to the pith, which is composed of relatively weak thin-walled parenchyma cells and vascular bundles (174). The non-dense/fibrous nature of the pith, as well as loss of water during compression, appeared to produce its highly nonlinear mechanical response (Figure 5.2). This nonlinear response has implications in lodging, which involves large deformation beyond the linear elastic regime. We also surmise that the continuous straining (plateaus in stress in Figure 5.2) arose from morphological changes such as vascular bundle delamination from the parenchyma cells, and densification of parenchyma cells under mechanical loading. Compression of the specimens at high loads resulted in stiffening, likely due to densification of the cell walls at high strains, thereby requiring high loads to produce morphological changes upon further loading.

The compressive response of the Della stem indicated nonlinear behavior up to the peak stress, followed by softening, a large plateau in stress, and ultimately more stiffening toward the end of loading. The failure in the stem was associated with buckling and splitting of the rind layer from the pith and the softening was followed by water draining from the stem (Figure 5.1C). Splitting/buckling reduces the load carrying capability of the structures, particularly of the rind itself. Upon completion of buckling, further compressing the specimens stiffened the response, similar to that observed in the pith, and again likely resulted from densification of the cell walls. Different rates of uniaxial compression tests for both stem and pith showed the time-dependent nature of the sorghum structure (Figure 5.2). For both the pith and stem, the slower rate (10%/min) produced smaller peak stresses at larger corresponding strains due to more stress relaxation occurring during slower loading.

The effect of time-dependent behavior was further investigated by conducting creep tests on the Della pith and stem, which has further implications for rate dependent behavior. Della showed pronounced time-dependent behaviors during the creep tests. These responses indicated large permanent deformations which were likely associated with the morphological changes of pith tissues under mechanical loading, as evidenced by the pith itself exhibiting a more prevalent creep deformation than the full stem (rind and pith). Thereafter, holding the load constant for about one hour showed that the pith exhibited a pronounced time-dependent response without additional water flowing out of the specimens, suggesting a viscoelastic mechanism.

As mentioned above, the time-dependent response of the tested piths was likely associated with a combination of poroelasticity and viscoelasticity. We attribute the poroelastic effect to the migration of water through the specimen and even out of the specimens under compression. Viscoelasticity also likely occurred due to the plant's composition of cellulose microfibrils and lignin matrices. Cellulose and lignin are long chain polymers with complex network microstructures. Some of time-dependent responses likely occurred due to reorientation of the microfibrils and macromolecular networks of the cellulose and lignin during loading. Viscoelastic effects were evidenced by a continuous increase in the strain when the load was kept constant (Figure 5.3A), even though no additional water was flowing out of the pith. However, we should note that in general, the viscous fluid flow of water within and through the cell walls (but not entirely out of the plant) might also contribute to the time-dependent response of the pith. Based on the current experimental data, it is difficult to separate the poroelastic and viscoelastic effects and determine the corresponding material parameters. However, the present study highlights the prevalence and importance of the time-dependent responses of sorghum.

Given the observed time-dependent behavior, simply using the 'elastic modulus' and treating the stems as elastic materials, as has been done in previous studies, will not provide enough information to fully capture sorghum's mechanical behavior under realistic loading conditions. Instead, time-dependent biomechanical models should be developed. Likewise, when the 'elastic modulus' is determined by quantifying the initial slope of the stress-strain curve, different values will be measured under different loading

rates, as we have reported in comparing Figures 5.2A and 5.2B. Additionally, sorghum stems are naturally anisotropic, due to the axial orientation of fiber bundles. As such, different loading modes and directions, e.g., from complex loading from wind, will produce different mechanical responses. In specific, initial slopes of stem under compression in axial direction were 130.1 MPa and 177.9 MPa which are depend on strain rate and are lower than moduli calculated from bending tests (350 – 630 MPa) (21). Besides, Young's modulus of sorghum stem in transverse direction were reported as 4.62 – 13.15 MPa which is much lower than the modulus under axial compression (175). Future studies should consider detailed assessments of specific microstructural changes in sorghum that correspond to our macroscopically observed nonlinear time-dependent mechanical behavior. Finally, to our knowledge, time-dependent behaviors have not been explored in other grass stems, although several studies in other plants (176-179) seem to indicate that viscoelasticity occurs. We believe that other cereal grass stems, particularly fresh (not dry) samples, will also show pronounced time-dependent behaviors that may be attributed to both poroelasticity and viscoelasticity, thereby motivating future studies.

5.5. Materials and methods

5.5.1. Plant materials

The sorghum cultivar Della was used throughout. Della is a medium stature photoperiod insensitive sweet sorghum type with potential for use as a bioenergy feedstock due to its high sucrose content. Growth of the experimental material began

April 13, 2019 in a greenhouse located at 30.6o N. Plants were grown in 19 L pots containing a fine sandy loam soil amended with 14-14-14 slow-release fertilizer. The temperature was 26-30 ºC day/21-26 ºC night, and the photoperiod was 14 h day/10 h night, with supplemental light provided by high pressure sodium lamps. Plants were harvested for mechanical testing at grain maturity, approximately 13 weeks after planting.

5.5.2. Sample preparation

Plants were harvested for mechanical testing by cutting the stems at the soil level. All sorghum samples were collected in the morning before temperatures increased and they lost water by evapotranspiration, specifically between 8-10 AM. All tests were performed within 6 hours after cutting the internode from the plant. Samples from internodes 9 and 10 were used in all of the performed tests. For compression experiments, a precision saw (Buehler Isomet 1000 Precision saw) was used to cut the samples of pith and the entire stem to help ensure that their top and bottom surfaces were parallel (see the cross-section in Figure 5.1). Rigid test plates were used due to a lack of access to self-aligning platens (which would have been preferable). As such, some error may be introduced in the measurement, particularly at the very early stages of loading. However, our results do not indicate large fluctuations at small loads, and as such it appears that the use of the precision saw indeed helped mitigate these potential sources of error. The pith specimens were cut in a cylindrical shape from the center of the stem using steel tubes as the punch. The diameter of the pith and stem specimens was

evaluated by measuring at three locations and taking an average value. Figure 5.1 shows anatomical structures of Della sorghum. Differences in the structural morphology can influence the overall response of the stems. Measurements of the length/height (L) and diameter (D) were collected immediately after cutting using digital calipers. Tables 5.1-5.6 summarize the dimensions of the tested samples. In selecting the aspect ratio of the test specimens, no specific ASTM standard exists for most of herbaceous plant stems including sorghums(146), which are complicated composite structures. These materials are quite soft and compliant and as such are more susceptible to buckling than traditional engineering materials. To this end, we follow the sample preparation of Wright, Christopher T., et al. (2005)(180) who have suggested an experimental method for a compression test for cellulosic feedstocks. In their approach, they use a diameter:length ratio of 1:1 to increase resistance to buckling.

Table 5.1 Dimensions of Della piths tested under uniaxial compression with a strain rate of 10%/min. Each sample was taken randomly from a plant among 10 replicants.

Uniaxial Compression of Piths (Strain Rate = 10%/min)				
	Diameter (mm)	**Height (mm)**	**Area (mm^2)**	**Height/Diameter Ratio**
Pith 1	8.38	13.17	55.15	1.57
Pith 2	8.69	9.96	59.31	1.15
Pith 3	8.73	10.42	59.86	1.19
Pith 4	8.86	10.44	61.65	1.18
Pith 5	8.01	11.07	50.39	1.38
Pith 6	7.95	11.28	49.64	1.42
Pith 7	8.64	12.33	58.63	1.43
Pith 8	8.06	11.54	51.02	1.43
Pith 9	8.12	10.97	51.78	1.35
Pith 10	8.64	12.38	58.63	1.43
Pith 11	8.76	12.36	60.27	1.41
Pith 12	8.61	12.52	58.22	1.45
Average	8.45	11.54	56.21	1.37
Standard Dev	0.33	1.01	4.363	0.13

Table 5.2 Dimensions of Della piths tested under uniaxial compression with a strain rate of 100%/min. Each sample was taken randomly from a plant among 10 replicants.

Uniaxial Compression of Piths (Strain Rate = 100%/min)				
	Diameter (mm)	**Length (mm)**	**Area (mm^2)**	**Height/Diameter Ratio**
Pith 1	8.15	11.72	52.17	1.44
Pith 2	8.08	12.01	51.28	1.49
Pith 3	8.77	11.98	60.41	1.37
Pith 4	8.69	12.45	59.31	1.43
Pith 5	7.36	11.77	42.54	1.6
Pith 6	7.9	10.9	49.02	1.38
Pith 7	8.64	11.69	58.63	1.35
Pith 8	8.58	11.82	57.82	1.38
Pith 9	8.77	11	60.41	1.25
Average	8.33	11.7	54.62	1.41
Standard Dev	0.49	0.49	6.22	0.1

Table 5.3 Dimensions of Della stems tested under uniaxial compression with a strain rate of 10%/min. Each sample was taken randomly from a plant among 10 replicants.

Uniaxial Compression of Stems (Strain Rate = 10%/min)				
	Diameter (mm)	**Length (mm)**	**Area (mm^2)**	**Height/Diameter Ratio**
Stem 1	12.35	18.66	119.79	1.51
Stem 2	12.58	18.31	124.29	1.46
Stem 3	12.55	17.42	123.7	1.4
Stem 4	12.74	19.24	127.48	1.51
Stem 5	10.49	16.18	86.42	1.54
Stem 6	11.78	17.42	108.99	1.48
Stem 7	11.39	17.31	101.89	1.52
Stem 8	11.59	18.83	105.5	1.62
Stem 9	11.15	18.66	97.64	1.67
Stem 10	11.38	18.04	101.71	1.59
Average	11.8	18.01	109.74	1.53
Standard Dev	0.74	0.92	13.57	0.08

Table 5.4 Dimensions of Della stems tested under uniaxial compression with a strain rate of 100%/min. Each sample was taken randomly from a plant among 10 replicants.

Uniaxial Compression of Stems (Strain Rate = 100%/min)				
	Diameter (mm)	**Length (mm)**	**Area (mm^2)**	**Height/Diameter Ratio**
Stem 1	11.42	17.38	102.43	1.52
Stem 2	11.18	15.55	98.17	1.39
Stem 3	11.03	15.15	95.55	1.37
Stem 4	11.1	15.56	96.77	1.4
Stem 5	12.21	19.93	117.09	1.63
Stem 6	11.92	19.17	111.59	1.61
Stem 7	10.42	13.91	85.27	1.34
Stem 8	10.43	14.41	85.44	1.38
Stem 9	10.69	16.76	89.75	1.57
Stem 10	9.96	15.97	77.91	1.6
Stem 11	10.84	15.95	92.29	1.47
Average	11.02	16.34	95.66	1.48
Standard Dev	0.66	1.86	11.58	0.11

Table 5.5 Dimensions of Della piths tested under compressive creep. Each sample was taken randomly from a plant among 10 replicants.

Creep Tests of Piths				
	Diameter (mm)	**Length (mm)**	**Area (mm^2)**	**Height/Diameter Ratio**
Pith 1	10.53	14.1	87.09	1.34
Pith 2	10.72	14.54	90.26	1.36
Pith 3	10.74	13.15	90.59	1.22
Average	10.66	13.93	89.31	1.31
Standard Dev	0.12	0.71	1.93	0.07

Table 5.6 Dimensions of Della stems tested under compressive creep. Each sample was taken randomly from a plant among 10 replicants.

Creep Tests of Stems				
	Diameter (mm)	**Length (mm)**	**Area (mm^2)**	**Height/Diameter Ratio**
Stem 1	11.61	18.5	105.86	1.59
Stem 2	11.93	18.67	111.78	1.56
Stem 3	12.14	18.55	115.75	1.53
Average	11.89	18.57	111.13	1.56
Standard Dev	0.27	0.09	4.97	0.03

5.5.3. Compression tests

Uniaxial compression tests were conducted on pith and stem specimens at room temperature using an Instron 5943 with a 1 kN load cell at a strain rate of 10%/min and 100%/min. The stress was calculated by dividing the force by the initial cross-sectional area, and the strain was calculated by dividing the displacement (cross-head

displacement) by the initial length, i.e., all quantities represent nominal "engineering" values. The compression tests were performed up to failure of the specimens. All samples were oriented such that the axial direction of the plant was aligned to the direction of applied load. This orientation represents the primary direction of compression that would occur during bending of the plants. Due to their relatively small thickness, rind specimens were not suitable for compression tests and as such were not included in this study. In addition, compressive creep tests were conducted on pith and stem specimens to investigate time-dependent effects. Creep tests were performed for 1 hour at prescribed loads of 50% of strength as measured from the uniaxial compression tests of the piths and stems. The strength is defined by the peak in stress (before the specimens experienced densification, as shown in Figure 5.2). In these creep tests, the specimens were initially ramped to the prescribed loads at a strain rate of 100%/min prior to the load hold. In all results, engineering stresses and strains were reported to evaluate the mechanical behaviors of the specimens.

5.5.4. Data analysis

Data was acquired through the Instron software (Bluehill® Universal 4.01) and processed in Microsoft Excel thereafter. To calculate the 'elastic moduli' of the specimens, the initial slopes under compression ramp tests were calculated from 0 to 0.5% (linear range) after implementing a standard toe correction method (following the procedure in ASTM D695). In materials that exhibit time-dependent responses (viscoelastic materials) the moduli of the materials cannot be determined by only

measuring the slopes of the stress-strain curves, as these slopes change with the loading rates. Therefore, we will not refer to these slopes as elastic moduli of the specimens; instead, we will refer to them as the 'initial slope'.

5.6. Conclusion and summary

To investigate the nonlinear and time-dependent responses of sweet sorghum stems, uniaxial compression and creep tests were conducted on the pith and stem of Della sorghum grown in a controlled environment in a greenhouse. The calculated initial slopes of the Della pith under uniaxial compression were 25.8 (±8.0) MPa for slow loading (10%/min) and 36.4 (±7.5) MPa for fast loading (100%/min). The corresponding slope of Della stems under uniaxial compression were 130.1 (±30.1) MPa for slow loading (10%/min) and 177.9 (±50.5) MPa for fast loading (100%/min). Beyond the linear region, under slow loading (10%/min), the pith showed a peak stress of 1.4 (±0.5) MPa at a strain of 14.1 (±6.7) %; under fast loading (100%/min), the pith showed a peak stress of 1.5 (±0.3) MPa at a strain of 6.2 (±1.4) %. Likewise, under slow loading (10%/min), the full stems showed a peak stress of 3.3 (±0.3) MPa at a strain of 7.4 (±1.8) %; under fast loading (100%/min), the stems showed a peak stress 4.0 (±0.6) MPa at a strain of 5.9 (±1.4) %. Both the pith and the stem exhibited highly nonlinear responses at larger strains: plateaus in stress, followed by stiffening at high compressive strains. All of these results indicate that Della sorghum exhibits pronounced rate/time-dependent biomechanical behavior. Creep tests further corroborated its significant time-dependent mechanical behavior, which we surmise arises from effects of both

poroelasticity and viscoelasticity. Poroelastic effects were evidenced through the observed water loss in the sorghum pith during loading. Viscoelastic effects also likely arose due to the delayed responses of cellulose microfibrils and lignin matrices to mechanical loading, which lead to rearrangements of the macromolecular networks. Overall, this paper provides clear evidence of nonlinear and time-dependent biomechanical responses of sorghum piths and stems, which can guide more systematic studies aimed at understanding the mechanisms of the complex biomechanical responses of grass stems. Furthermore, this study provides several insights into the behavior of crops in the agricultural environment. It is possible that strong winds could result in creep responses and deformation of the stems of field grown plants, as a consequence of both poroelastic processes such as water migration and viscoelastic processes such as disruption of structural polymers. Such responses could contribute to stem failure (lodging) often observed in crops experiencing inclement weather.

6. SUMMARY

This dissertation investigated the mechanical and fracture behavior of soft materials: specifically a silicone elastomer, elastomer composites, and a biological composite.

First, we detailed a peculiar form of fracture that we discovered to occur in a highly stretchable silicone elastomer (Smooth-On Ecoflex 00–30). Under certain conditions, cracks propagate in a direction perpendicular to the initial precut and in the direction of the applied load. In other words, the crack deviates from the standard trajectory and instead propagates perpendicular to that trajectory. The crack arrests stably, and thus the material ahead of the crack front continues to sustain load, thereby enabling enormous stretchabilities. We call this phenomenon "sideways" and stable cracking. To explain this behavior, we performed finite-element simulations that demonstrated a propensity for sideways cracking, even in an isotropic material. The simulations also highlighted the importance of crack-tip blunting on the formation of sideways cracks. Next, we provided a hypothesis on the origin of sideways cracking that relates to microstructural anisotropy (in a nominally isotropic elastomer). To substantiate this hypothesis, we transversely pre-stretched samples to various extents before fracture testing, as to determine the influence of microstructural arrangement (chain alignment and strain-induced crystallization) on fracture energy. We also performed microstructural characterization that indicated that significant chain alignment and strain-induced crystallization indeed occur in this material upon stretching. We

concluded by characterizing how a number of loading conditions, such as sample geometry and strain rate, affect this phenomenon. Overall, this study provides fundamental mechanical insight into basic phenomena associated with fracture of elastomers.

Next, we have investigated a new type of elastomer "composite" that provides increased fracture resistance and stretchability while simultaneously decreasing the overall weight. Unlike in standard reinforced composite systems, we have dispersed voids into a silicone elastomer matrix, thereby creating a "negative" composite that provides increased fracture resistance and stretchability in pre-cut specimens while simultaneously decreasing the weight. Experiments and simulations show that the voids locally weaken the specimen, guiding the crack along a tortuous path that ultimately dissipates more energy. We investigate two geometries in pre-cut specimens (interconnected patterns of voids and randomly distributed discrete voids), each of which more than double the energy dissipated prior to complete rupture, as compared to that of the pristine elastomer. We also demonstrate that the energy dissipated during fracture increases with the volume fraction of the voids. Overall, this work demonstrates that voids can impart increased resistance to rupture in elastomers with flaws. Since additive manufacturing processes can readily introduce/pattern voids, we expect that applications of these void-elastomer "composites" will only increase going forward, as will the need to understand their mechanics.

This dissertation also detailed results of finite element analysis for three different types of flexible and stretchable electronic systems. First, we studied a stretchable

ultrasound probe that can conform to and detect nonplanar complex surfaces. The probe consists of a 10 x 10 array of piezoelectric transducers that exploit an “island-bridge” layout with multilayer electrodes, encapsulated by thin and compliant silicone elastomers. 2 x 2 simplified piezoelectric transducers were considered for numerical analysis. The stretchable probe demonstrated excellent electromechanical coupling, minimal cross-talk, and more than 50% stretchability under biaxial tension. Next, we studied single crystal perovskite photovoltaic devices. To maximize flexibility of this device, neutral mechanical plane designs were calculated and implemented. FEA analysis showed that the highest value of the maximum principal stress existed near the edge of perovskite layer due to Poisson effects. When the radius of curvature of perovskite layer was ~2.5 mm (the critical radius of curvature to cause cracks in the bending experiments), the maximum principal stress in tension is ~110 MPa. The corresponding strain is ~0.88%, which provides an estimate on the failure strain of this perovskite material. Finally, we performed numerical simulations for thin, wireless, and mechanically flexible optoelectronic for implanting to control the activity of subsets of neurons and nerve fibers in vivo. The finite element simulations showed that the Cu layer of the interconnect will not yield until a level of ~80% global strain. This mechanical flexibility is an attractive characteristic to enable a versatile platform for wireless delivery of light to organs and tissues in freely moving animals.

This dissertation also examined the biomechanical properties of bioenergy sweet sorghum (Sorghum bicolor (L.) Moench), focusing on the time-dependent behavior of the stems. Specifically, we conducted uniaxial compression tests under ramp and creep

loading on pith and stem specimens of the sorghum cultivar Della. The tests demonstrated significantly nonlinear and time-dependent stress-strain behavior in all samples. We surmised that this behavior arises from a combination of poroelasticity due to migration of water through the plant and viscoelasticity due to rearrangement of macromolecular networks, such as cellulose microfibrils and lignin matrices. Overall, these measurements demonstrate that sorghum is not a simple reversible elastic material. As such, a complete understanding of the conditions that lead to stem lodging will require knowledge of sorghum's time-dependent biomechanical properties. Of practical importance, the time-dependent biomechanical properties of the stem influence its mechanical stability under various loading conditions during growth in the field (e.g., different wind speeds).

REFERENCES

1. De D, Gent A (1996) Tear strength of carbon-black-filled compounds. *Rubber Chemistry Technology* 69(5):834-850.
2. Greensmith H (1956) Rupture of rubber. IV. Tear properties of vulcanizates containing carbon black. *Journal of Polymer Science* 21(98):175-187.
3. Ahmed S, Jones F (1990) A review of particulate reinforcement theories for polymer composites. *Journal of Materials Science* 25(12):4933-4942.
4. Valdastri P, Harada K, Menciassi A, Beccai L, Stefanini C, Fujie M, Dario P (2006) Integration of a miniaturised triaxial force sensor in a minimally invasive surgical tool. *IEEE Transactions on Biomedical Engineering* 53(11):2397-2400.
5. Schwartz G, Tee BC-K, Mei J, Appleton AL, Kim DH, Wang H, Bao Z (2013) Flexible polymer transistors with high pressure sensitivity for application in electronic skin and health monitoring. *Nature Communications* 4(1):1-8.
6. Kim D-H, Lu N, Ma R, Kim Y-S, Kim R-H, Wang S, Wu J, Won SM, Tao H, Islam A (2011) Epidermal electronics. *Science* 333(6044):838-843.
7. Takei K, Takahashi T, Ho JC, Ko H, Gillies AG, Leu PW, Fearing RS, Javey A (2010) Nanowire active-matrix circuitry for low-voltage macroscale artificial skin. *Nature Materials* 9(10):821-826.
8. Mannsfeld SC, Tee BC, Stoltenberg RM, Chen CVH, Barman S, Muir BV, Sokolov AN, Reese C, Bao Z (2010) Highly sensitive flexible pressure sensors with microstructured rubber dielectric layers. *Nature Materials* 9(10):859-864.

9. Sekitani T, Zschieschang U, Klauk H, Someya T (2010) Flexible organic transistors and circuits with extreme bending stability. *Nature Materials* 9(12):1015-1022.

10. Ramuz M, Tee BCK, Tok JBH, Bao Z (2012) Transparent, optical, pressure-sensitive artificial skin for large-area stretchable electronics. *Advanced Materials* 24(24):3223-3227.

11. Sokolov AN, Tee BC, Bettinger CJ, Tok JB-H, Bao Z (2012) Chemical and engineering approaches to enable organic field-effect transistors for electronic skin applications. *Accounts of Chemical Research* 45(3):361-371.

12. Maheshwari V, Saraf RF (2006) High-resolution thin-film device to sense texture by touch. *Science* 312(5779):1501-1504.

13. Wagner S, Lacour SP, Jones J, Pai-hui IH, Sturm JC, Li T, Suo Z (2004) Electronic skin: architecture and components. *Physica E: Low-dimensional Systems and Nanostructures* 25(2-3):326-334.

14. Lipomi DJ, Vosgueritchian M, Tee BC, Hellstrom SL, Lee JA, Fox CH, Bao Z (2011) Skin-like pressure and strain sensors based on transparent elastic films of carbon nanotubes. *Nature Nanotechnology* 6(12):788.

15. Viventi J, Kim D-H, Vigeland L, Frechette ES, Blanco JA, Kim Y-S, Avrin AE, Tiruvadi VR, Hwang S-W, Vanleer AC (2011) Flexible, foldable, actively multiplexed, high-density electrode array for mapping brain activity in vivo. *Nature Neuroscience* 14(12):1599.

16. Kim D-H, Lu N, Ghaffari R, Kim Y-S, Lee SP, Xu L, Wu J, Kim R-H, Song J, Liu Z (2011) Materials for multifunctional balloon catheters with capabilities in cardiac electrophysiological mapping and ablation therapy. *Nature Materials* 10(4):316-323.

17. Khang D-Y, Jiang H, Huang Y, Rogers JA (2006) A stretchable form of single-crystal silicon for high-performance electronics on rubber substrates. *Science* 311(5758):208-212.

18. Paterson AH, Bowers JE, Bruggmann R, Dubchak I, Grimwood J, Gundlach H, Haberer G, Hellsten U, Mitros T, Poliakov A (2009) The Sorghum bicolor genome and the diversification of grasses. *Nature* 457(7229):551-556.

19. Rooney LW, Waniska RD (2000) Sorghum food and industrial utilization. *Sorghum: Origin, History, Technology, and Production*:689-729.

20. Mathur S, Umakanth A, Tonapi V, Sharma R, Sharma MK (2017) Sweet sorghum as biofuel feedstock: recent advances and available resources. *Biotechnology for Biofuels* 10(1):146.

21. Lemloh M-L, Pohl A, Weber E, Zeiger M, Bauer P, Weiss IM, Schneider AS (2014) Structure-property relationships in mechanically stimulated Sorghum bicolor stalks. *Bioinspired Materials* 1(1).

22. Al-Zube LA, Robertson DJ, Edwards JN, Sun W, Cook DD (2017) Measuring the compressive modulus of elasticity of pith-filled plant stems. *Plant Methods* 13(1):99.

23. Al-Zube L, Sun W, Robertson D, Cook D (2018) The elastic modulus for maize stems. *Plant Methods* 14(1):11.

24. Takei K, Takahashi T, Ho JC, Ko H, Gillies AG, Leu PW, Fearing RS, Javey A (2010) Nanowire active-matrix circuitry for low-voltage macroscale artificial skin. *Nature Materials* 9(10):821.

25. Mannsfeld SC, Tee BC, Stoltenberg RM, Chen CVH, Barman S, Muir BV, Sokolov AN, Reese C, Bao Z (2010) Highly sensitive flexible pressure sensors with microstructured rubber dielectric layers. *Nature Materials* 9(10):859.

26. Sokolov AN, Tee BC, Bettinger CJ, Tok JB-H, Bao Z (2011) Chemical and engineering approaches to enable organic field-effect transistors for electronic skin applications. *Accounts of Chemical Research* 45(3):361-371.

27. Cai S, Lou Y, Ganguly P, Robisson A, Suo Z (2010) Force generated by a swelling elastomer subject to constraint. *Journal of Applied Physics* 107(10):103535.

28. Schwartz G, Tee BC-K, Mei J, Appleton AL, Kim DH, Wang H, Bao Z (2013) Flexible polymer transistors with high pressure sensitivity for application in electronic skin and health monitoring. *Nature Communications* 4:1859.

29. Sekitani T, Zschieschang U, Klauk H, Someya T (2010) Flexible organic transistors and circuits with extreme bending stability. *Nature Materials* 9(12):1015.

30. Dong L, Jiang H (2007) Autonomous microfluidics with stimuli-responsive hydrogels. *Soft Matter* 3(10):1223-1230.

31. Beebe DJ, Moore JS, Bauer JM, Yu Q, Liu RH, Devadoss C, Jo B-H (2000) Functional hydrogel structures for autonomous flow control inside microfluidic channels. *Nature* 404(6778):588.

32. Pang C, Lee G-Y, Kim T-i, Kim SM, Kim HN, Ahn S-H, Suh K-Y (2012) A flexible and highly sensitive strain-gauge sensor using reversible interlocking of nanofibres. *Nature Materials* 11(9):795.

33. Frogley MD, Ravich D, Wagner HD, technology (2003) Mechanical properties of carbon nanoparticle-reinforced elastomers. *Composites Science* 63(11):1647-1654.

34. Wang Y, Ameer GA, Sheppard BJ, Langer R (2002) A tough biodegradable elastomer. *Nature Biotechnology* 20(6):602.

35. Li C-H, Wang C, Keplinger C, Zuo J-L, Jin L, Sun Y, Zheng P, Cao Y, Lissel F, Linder C (2016) A highly stretchable autonomous self-healing elastomer. *Nature Chemistry* 8(6):618.

36. Liu M, Sun J, Sun Y, Bock C, Chen Q (2009) Thickness-dependent mechanical properties of polydimethylsiloxane membranes. *Journal of Micromechanics and Microengineering* 19(3):035028.

37. Creton C, Ciccotti M (2016) Fracture and adhesion of soft materials: a review. *Reports on Progress in Physics* 79(4):046601.

38. Beiermann BA, Kramer SL, May PA, Moore JS, White SR, Sottos NR (2014) The Effect of Polymer Chain Alignment and Relaxation on Force-Induced Chemical Reactions in an Elastomer. *Advanced Functional Materials* 24(11):1529-1537.

39. Hui C-Y, Jagota A, Bennison S, Londono J (2003) Crack blunting and the strength of soft elastic solids. *Proceedings of the Royal Society of London A: Mathematical, Physical and Engineering Sciences* 459(2034):1489-1516.

40. Pharr M, Sun J-Y, Suo Z (2012) Rupture of a highly stretchable acrylic dielectric elastomer. *Journal of Applied Physics* 111(10):104114.

41. Chen C, Wang Z, Suo Z (2017) Flaw sensitivity of highly stretchable materials. *Extreme Mechanics Letters* 10:50-57.

42. Feichter C, Major Z, Lang R (2006) Deformation analysis of notched rubber specimens. *Strain* 42(4):299-304.

43. Gent A, Razzaghi-Kashani M, Hamed G (2003) Why do cracks turn sideways? *Rubber chemistry Technology* 76(1):122-131.

44. Hamed G, Park B (1999) The mechanism of carbon black reinforcement of SBR and NR vulcanizates. *Rubber Chemistry Technology* 72(5):946-959.

45. Hu H, Zhu X, Wang C, Zhang L, Li X, Lee S, Huang Z, Chen R, Chen Z, Wang C (2018) Stretchable ultrasonic transducer arrays for three-dimensional imaging on complex surfaces. *Science Advances* 4(3):eaar3979.

46. Park M, Im J, Shin M, Min Y, Park J, Cho H, Park S, Shim M-B, Jeon S, Chung D-Y (2012) Highly stretchable electric circuits from a composite material of silver nanoparticles and elastomeric fibres. *Nature Nanotechnology* 7(12):803.

47. Xu S, Zhang Y, Cho J, Lee J, Huang X, Jia L, Fan JA, Su Y, Su J, Zhang H (2013) Stretchable batteries with self-similar serpentine interconnects and integrated wireless recharging systems. *Nature Communications* 4:1543.

48. Ying M, Bonifas AP, Lu N, Su Y, Li R, Cheng H, Ameen A, Huang Y, Rogers JA (2012) Silicon nanomembranes for fingertip electronics. *Nanotechnology* 23(34):344004.

49. Pan T, Pharr M, Ma Y, Ning R, Yan Z, Xu R, Feng X, Huang Y, Rogers JA (2017) Experimental and theoretical studies of serpentine interconnects on ultrathin elastomers for stretchable electronics. *Advanced Functional Materials* 27(37):1702589.

50. Liu Y, Pharr M, Salvatore GA (2017) Lab-on-skin: a review of flexible and stretchable electronics for wearable health monitoring. *ACS Nano* 11(10):9614-9635.

51. Busse W (1934) Tear resistance and structure of rubber. *Industrial Engineering Chemistry* 26(11):1194-1199.

52. Hamed G, Al-Sheneper (2003) Effect of carbon black concentration on cut growth in NR vulcanizates. *Rubber Chemistry Technology* 76(2):436-460.

53. Caimmi F, Calabrò R, Briatico-Vangosa F, Marano C, Rink M (2015) Toughness of natural rubber compounds under biaxial loading. *Engineering Fracture Mechanics* 149:250-261.

54. Marano C, Calabrò R, Rink M (2010) Effect of molecular orientation on the fracture behavior of carbon black-filled natural rubber compounds. *Journal of Polymer Science Part B: Polymer Physics* 48(13):1509-1515.

55. Hardin G, Zhang Y, Fincher C, Pharr M (2017) Interfacial Fracture of Nanowire Electrodes of Lithium-Ion Batteries. *JOM* 69(9):1519-1523.

56. Trabelsi S, Albouy P-A, Rault J (2002) Stress-induced crystallization around a crack tip in natural rubber. *Macromolecules* 35(27):10054-10061.

57. Tosaka M, Noda M, Ito K, Senoo K, Aoyama K, Ohta N (2013) Strain-and temperature-induced polymorphism of poly (dimethylsiloxane). *Colloid Polymer Science* 291(11):2719-2724.

58. Whanger JK, Harrall SJ (2004) Reinforced swelling elastomer seal element on expandable tubular. *U.S. Patent 6,834,725. Washington, DC: U.S. Patent and Tradmark Office.*

59. Brown DD (1977) Expansion joint with elastomer seal. *U.S. Patent 4,007,994. Washington DC: U.S. Patent and Tradmark Office.*

60. Lou Y, Robisson A, Cai S, Suo Z (2012) Swellable elastomers under constraint. *Journal of Applied Physics* 112(3):034906.

61. Wang Z, Chen C, Liu Q, Lou Y, Suo Z (2017) Extrusion, slide, and rupture of an elastomeric seal. *Journal of the Mechanics and Physics of Solids* 99:289-303.

62. Zhang H, Wang MY, Li J, Zhu J (2016) A soft compressive sensor using dielectric elastomers. *Smart Materials Structures* 25(3):035045.

63. Xu Z, Zheng S, Wu X, Liu Z, Bao R, Yang W, Yang MJCPAAS (2019) High actuated performance MWCNT/Ecoflex dielectric elastomer actuators based on layer-by-layer structure. *Composites Part A: Applied Science Manufacturing* 125:105527.

64. Wang Q, Suo Z, Zhao X (2012) Bursting drops in solid dielectrics caused by high voltages. *Nature Communications* 3:1157.

65. Kwon D, Lee T-I, Shim J, Ryu S, Kim MS, Kim S, Kim T-S, Park I (2016) Highly sensitive, flexible, and wearable pressure sensor based on a giant piezocapacitive effect of three-dimensional microporous elastomeric dielectric layer. *ACS Applied Materials Interfaces* 8(26):16922-16931.

66. Atalay O, Atalay A, Gafford J, Walsh C (2018) A highly sensitive capacitive-based soft pressure sensor based on a conductive fabric and a microporous dielectric layer. *Advanced Materials Technologies* 3(1):1700237.

67. Courtney J, Gilchrist T (1980) Silicone rubber and natural rubber as biomaterials. *Medical and Biological Engineering and Computing* 18(4):538-540.

68. Lee KY, Mooney DJ (2001) Hydrogels for tissue engineering. *Chemical Reviews* 101(7):1869-1880.

69. Marler JJ, Upton J, Langer R, Vacanti JP (1998) Transplantation of cells in matrices for tissue regeneration. *Advanced Drug Delivery Reviews* 33(1-2):165-182.

70. Pelrine R, Kornbluh R, Pei Q, Joseph J (2000) High-speed electrically actuated elastomers with strain greater than 100%. *Science* 287(5454):836-839.

71. Yang D, Mosadegh B, Ainla A, Lee B, Khashai F, Suo Z, Bertoldi K, Whitesides GM (2015) Buckling of elastomeric beams enables actuation of soft machines. *Advanced Materials* 27(41):6323-6327.

72. Anderson IA, Gisby TA, McKay TG, O'Brien BM, Calius EP (2012) Multi-functional dielectric elastomer artificial muscles for soft and smart machines. *Journal of Applied Physics* 112(4):041101.

73. Amjadi M, Yoon YJ, Park I (2015) Ultra-stretchable and skin-mountable strain sensors using carbon nanotubes–Ecoflex nanocomposites. *Nanotechnology* 26(37):375501.

74. Ma Y, Pharr M, Wang L, Kim J, Liu Y, Xue Y, Ning R, Wang X, Chung HU, Feng X (2017) Soft elastomers with ionic liquid-filled cavities as strain isolating substrates for wearable electronics. *Small* 13(9):1602954.

75. Yao S, Zhu Y (2014) Wearable multifunctional sensors using printed stretchable conductors made of silver nanowires. *Nanoscale* 6(4):2345-2352.

76. Pelrine R, Kornbluh RD, Eckerle J, Jeuck P, Oh S, Pei Q, Stanford S (2001) Dielectric elastomers: generator mode fundamentals and applications. *Smart Structures and Materials 2001: Electroactive Polymer Actuators and Devices*, (International Society for Optics and Photonics), pp 148-156.

77. Herzberger J, Sirrine JM, Williams CB, Long TE (2019) Polymer Design for 3D Printing Elastomers: Recent Advances in Structure, Properties, and Printing. *Progress in Polymer Science*:101144.

78. Rossiter J, Walters P, Stoimenov B (2009) Printing 3D dielectric elastomer actuators for soft robotics. *Electroactive Polymer Actuators and Devices (EAPAD) 2009*, (International Society for Optics and Photonics), p 72870H.

79. Patel DK, Sakhaei AH, Layani M, Zhang B, Ge Q, Magdassi S (2017) Highly stretchable and UV curable elastomers for digital light processing based 3D printing. *Advanced Materials* 29(15):1606000.

80. Plott J, Tian X, Shih AJ (2018) Voids and tensile properties in extrusion-based additive manufacturing of moisture-cured silicone elastomer. *Additive Manufacturing* 22:606-617.

81. Moore JP, Williams CB (2008) Fatigue characterization of 3D printed elastomer material. *19th Annual International Solid Freeform Fabrication Symposium (SFF), Austin, TX, Aug*, pp 4-6.

82. Bai R, Yang J, Morelle XP, Suo Z (2019) Flaw-Insensitive Hydrogels under Static and Cyclic Loads. *Macromolecular Rapid Communications* 40(8):1800883.

83. Wu J, Cai LH, Weitz DA (2017) Tough Self-Healing Elastomers by Molecular Enforced Integration of Covalent and Reversible Networks. *Advanced Materials* 29(38):1702616.

84. Illeperuma WR, Sun J-Y, Suo Z, Vlassak JJ (2014) Fiber-reinforced tough hydrogels. *Extreme Mechanics Letters* 1:90-96.

85. Lin S, Cao C, Wang Q, Gonzalez M, Dolbow JE, Zhao X (2014) Design of stiff, tough and stretchy hydrogel composites via nanoscale hybrid crosslinking and macroscale fiber reinforcement. *Soft Matter* 10(38):7519-7527.

86. He Q, Wang Z, Yan Y, Zheng J, Cai S (2016) Polymer nanofiber reinforced double network gel composite: Strong, tough and transparent. *Extreme Mechanics Letters* 9:165-170.

87. Kazem N, Bartlett MD, Majidi C (2018) Extreme toughening of soft materials with liquid metal. *Advanced Materials* 30(22):1706594.

88. Lin W-C, Fan W, Marcellan A, Hourdet D, Creton C (2010) Large strain and fracture properties of poly (dimethylacrylamide)/silica hybrid hydrogels. *Macromolecules* 43(5):2554-2563.

89. Wang Z, Xiang C, Yao X, Le Floch P, Mendez J, Suo Z (2019) Stretchable materials of high toughness and low hysteresis. *Proceedings of the National Academy of Sciences* 116(13):5967-5972.

90. Bokobza L (2004) Elastomeric composites. I. Silicone composites. *Journal of Applied Polymer Science* 93(5):2095-2104.

91. Lee S, Pharr M (2019) Sideways and stable crack propagation in a silicone elastomer. *Proceedings of the National Academy of Sciences* 116(19):9251-9256.

92. Kidane A (2013) On the failure and fracture of polymer foam containing discontinuities. *ISRN Materials Science* 2013.

93. Gupta N, Woldesenbet E, Sankaran S (2001) Studies on compressive failure features in syntactic foam material. *Journal of Materials Science* 36(18):4485-4491.

94. Kim HS, Oh HH (2000) Manufacturing and impact behavior of syntactic foam. *Journal of Applied Polymer Science* 76(8):1324-1328.

95. Bunn P, Mottram J (1993) Manufacture and compression properties of syntactic foams. *Composites* 24(7):565-571.

96. Gupta N, Woldesenbet E, Mensah P (2004) Compression properties of syntactic foams: effect of cenosphere radius ratio and specimen aspect ratio. *Composites Part A: Applied Science and Manufacturing* 35(1):103-111.

97. Wouterson EM, Boey FY, Hu X, Wong S-C (2005) Specific properties and fracture toughness of syntactic foam: Effect of foam microstructures. *Composites Science and Technology* 65(11-12):1840-1850.

98. McIntyre A, Anderton G (1979) Fracture properties of a rigid polyurethane foam over a range of densities. *Polymer* 20(2):247-253.

99. Cotgreave T, Shortall J (1978) The fracture toughness of reinforced polyurethane foam. *Journal of Materials Science* 13(4):722-730.

100. Benderly D, Rezek Y, Zafran J, Gorni D (2004) Effect of composition on the fracture toughness and flexural strength of syntactic foams. *Polymer Composites* 25(2):229-236.

101. Sarkar S, Dadhania M, Rourke P, Desai TA, Wong JY (2005) Vascular tissue engineering: microtextured scaffold templates to control organization of vascular smooth muscle cells and extracellular matrix. *Acta Biomaterialia* 1(1):93-100.

102. Hollister SJ (2005) Porous scaffold design for tissue engineering. *Nature Materials* 4(7):518.

103. Mi Y, Chan Y, Trau D, Huang P, Chen E (2006) Micromolding of PDMS scaffolds and microwells for tissue culture and cell patterning: A new method of microfabrication by the self-assembled micropatterns of diblock copolymer micelles. *Polymer* 47(14):5124-5130.

104. Pilla S (2011) *Handbook of Bioplastics and Biocomposites Engineering Applications* (John Wiley & Sons).

105. Mooney DJ, Baldwin DF, Suh NP, Vacanti JP, Langer R (1996) Novel approach to fabricate porous sponges of poly (D, L-lactic-co-glycolic acid) without the use of organic solvents. *Biomaterials* 17(14):1417-1422.

106. Rivlin R, Thomas AG (1953) Rupture of rubber. I. Characteristic energy for tearing. *Journal of Polymer Science* 10(3):291-318.

107. Li Y, Zhu D, Handschuh-Wang S, Lv G, Wang J, Li T, Chen C, He C, Zhang J, Liu Y (2017) Bioinspired, Mechano-Regulated Interfaces for Rationally Designed, Dynamically Controlled Collection of Oil Spills from Water. *Global Challenges* 1(3):1600014.

108. Miriyev A, Stack K, Lipson H (2017) Soft material for soft actuators. *Nature Communications* 8(1):596.

109. Mohanty S, Larsen LB, Trifol J, Szabo P, Burri HVR, Canali C, Dufva M, Emnéus J, Wolff A (2015) Fabrication of scalable and structured tissue engineering scaffolds using water dissolvable sacrificial 3D printed moulds. *Materials Science and Engineering: C* 55:569-578.

110. Yang WS, Park B-W, Jung EH, Jeon NJ, Kim YC, Lee DU, Shin SS, Seo J, Kim EK, Noh JH (2017) Iodide management in formamidinium-lead-halide-based perovskite layers for efficient solar cells. *Science* 356(6345):1376-1379.

111. Lin K, Xing J, Quan LN, de Arquer FPG, Gong X, Lu J, Xie L, Zhao W, Zhang D, Yan C (2018) Perovskite light-emitting diodes with external quantum efficiency exceeding 20 percent. *Nature* 562(7726):245.

112. Feng J, Gong C, Gao H, Wen W, Gong Y, Jiang X, Zhang B, Wu Y, Wu Y, Fu H (2018) Single-crystalline layered metal-halide perovskite nanowires for ultrasensitive photodetectors. *Nature Electronics* 1(7):404.

113. NREL (2019) Best Research-Cell Efficiencies. *National Renewable Energy Laboratory: Golden, Colorado*

114. Wang Q, Shao Y, Dong Q, Xiao Z, Yuan Y, Huang J (2014) Large fill-factor bilayer iodine perovskite solar cells fabricated by a low-temperature solution-process. *Energy & Environmental Science* 7(7):2359-2365.

115. Chen Z, Dong Q, Liu Y, Bao C, Fang Y, Lin Y, Tang S, Wang Q, Xiao X, Bai Y, Deng Y, Huang J (2017) Thin single crystal perovskite solar cells to harvest below-bandgap light absorption. *Nature Communications* 8(1):1890.

116. Huang Y, Zhang Y, Sun J, Wang X, Sun J, Chen Q, Pan C, Zhou H (2018) The Exploration of Carrier Behavior in the Inverted Mixed Perovskite Single-Crystal Solar Cells. *Advanced Materials Interfaces* 5(14).

117. Lee L, Baek J, Park KS, Lee Y-E, Shrestha NK, Sung MM (2017) Wafer-scale single-crystal perovskite patterned thin films based on geometrically-confined lateral crystal growth. *Nature Communications* 8:15882.

118. Saidaminov MI, Abdelhady AL, Murali B, Alarousu E, Burlakov VM, Peng W, Dursun I, Wang L, He Y, Maculan G (2015) High-quality bulk hybrid perovskite single crystals within minutes by inverse temperature crystallization. *Nature Communications* 6:7586.

119. Liu M, Johnston MB, Snaith HJ (2013) Efficient planar heterojunction perovskite solar cells by vapour deposition. *Nature* 501(7467):395.

120. Lv Q, Lian Z, He W, Sun J-L, Li Q, Yan Q (2018) A universal top-down approach toward thickness-controllable perovskite single-crystalline thin films. *Journal of Materials Chemistry C* 6(16):4464-4470.

121. Gu Z, Huang Z, Li C, Li M, Song Y (2018) A general printing approach for scalable growth of perovskite single-crystal films. *Science Advances* 4(6):2390.

122. Anonymous (2019) A decade of perovskite photovoltaics. *Nature Energy* 4(1):1-1.

123. Reese MO, Glynn S, Kempe MD, McGott DL, Dabney MS, Barnes TM, Booth S, Feldman D, Haegel NM (2018) Increasing markets and decreasing package weight for high-specific-power photovoltaics. *Nature Energy* 3(11):1002-1012.

124. Cheng Y-B, Pascoe A, Huang F, Peng Y (2016) Print flexible solar cells. *Nature News* 539(7630):488.

125. Gupta S, Navaraj WT, Lorenzelli L, Dahiya R (2018) Ultra-thin chips for high-performance flexible electronics. *NPJ Flexible Electronics* 2(1):8.

126. Liu D, Kelly TL (2014) Perovskite solar cells with a planar heterojunction structure prepared using room-temperature solution processing techniques. *Nature Photonics* 8(2):133.

127. Ćirić L, Ashby K, Abadie T, Spina M, Duchamp M, Náfrádi B, Kollár M, Forró L, Horváth E (2018) Mechanical response of $CH_3NH_3PbI_3$ nanowires.*Applied Physics Letters* 112(11):111901.

128. Kwon KY, Lee H-M, Ghovanloo M, Weber A, Li W (2015) Design, fabrication, and packaging of an integrated, wirelessly-powered optrode array for optogenetics application. *Frontiers in Systems Neuroscience* 9:69.

129. Montgomery KL, Yeh AJ, Ho JS, Tsao V, Iyer SM, Grosenick L, Ferenczi EA, Tanabe Y, Deisseroth K, Delp SL (2015) Wirelessly powered, fully internal optogenetics for brain, spinal and peripheral circuits in mice. *Nature Methods* 12(10):969-974.

130. Rossi MA, Go V, Murphy T, Fu Q, Morizio J, Yin HH (2015) A wirelessly controlled implantable LED system for deep brain optogenetic stimulation. *Frontiers in Integrative Neuroscience* 9:8.

131. Salimpoor VN, van den Bosch I, Kovacevic N, McIntosh AR, Dagher A, Zatorre RJ (2013) Interactions between the nucleus accumbens and auditory cortices predict music reward value. *Science* 340(6129):216-219.

132. Park SI, Brenner DS, Shin G, Morgan CD, Copits BA, Chung HU, Pullen MY, Noh KN, Davidson S, Oh SJ (2015) Soft, stretchable, fully implantable miniaturized optoelectronic systems for wireless optogenetics. *Nature Biotechnology* 33(12):1280.

133. Gutruf P, Rogers JA (2018) Implantable, wireless device platforms for neuroscience research. *Current Opinion in Neurobiology* 50:42-49.

134. Shin G, Gomez AM, Al-Hasani R, Jeong YR, Kim J, Xie Z, Banks A, Lee SM, Han SY, Yoo CJ (2017) Flexible near-field wireless optoelectronics as subdermal implants for broad applications in optogenetics. *Neuron* 93(3):509-521. e503.

135. Zhang Z, Lin G, Zhang S, Zhou J (2007) Effects of Ce on microstructure and mechanical properties of pure copper. *Materials Science Engineering: A* 457(1-2):313-318.

136. Lowe MJ, Alleyne DN, Cawley P (1998) Defect detection in pipes using guided waves. *Ultrasonics* 36(1-5):147-154.

137. Drinkwater BW, Wilcox PD (2006) Ultrasonic arrays for non-destructive evaluation: A review. *Ndt&E Int.* 39(7):525-541.

138. Bi Z, Pilkey WD, Pilkey DF (2020) *Peterson's Stress Concentration Factors* (John Wiley & Sons).

139. Bowen C, Bradley L, Almond D, Wilcox P (2008) Flexible piezoelectric transducer for ultrasonic inspection of non-planar components. *Ultrasonics* 48(5):367-375.

140. Ceh D, Peters TM, Chen EC (2015) Acoustic characterization of polyvinyl chloride and self-healing silicone as phantom materials. *Medical Imaging 2015: Physics of Medical Imaging*, (International Society for Optics and Photonics), p 94123G.

141. Secor EB, Prabhumirashi PL, Puntambekar K, Geier ML, Hersam MC (2013) Inkjet printing of high conductivity, flexible graphene patterns. *The Journal of Physical Chemistry Letters* 4(8):1347-1351.

142. Rotenberg MY, Tian B (2017) Bioelectronic devices: Long-lived recordings. *Nature Biomedical Engineering* 1(3):0048.

143. Kaltenbrunner M, Sekitani T, Reeder J, Yokota T, Kuribara K, Tokuhara T, Drack M, Schwödiauer R, Graz I, Bauer-Gogonea S (2013) An ultra-lightweight design for imperceptible plastic electronics. *Nature* 499(7459):458.

144. Huang X, Liu Y, Kong GW, Seo JH, Ma Y, Jang K-I, Fan JA, Mao S, Chen Q, Li D (2016) Epidermal radio frequency electronics for wireless power transfer. *Microsystems Nanoengineering* 2:16052.

145. Hussain AM, Ghaffar FA, Park SI, Rogers JA, Shamim A, Hussain MM (2015) Metal/polymer based stretchable antenna for constant frequency far-field communication in wearable electronics. *Advanced Functional Materials* 25(42):6565-6575.

146. Shah DU, Reynolds TP, Ramage MH (2017) The strength of plants: theory and experimental methods to measure the mechanical properties of stems. *Journal of Experimental Botany* 68(16):4497-4516.

147. Slewinski TL (2012) Non-structural carbohydrate partitioning in grass stems: a target to increase yield stability, stress tolerance, and biofuel production. *Journal of Experimental Botany* 63(13):4647-4670.

148. Berry P, Sterling M, Spink J, Baker C, Sylvester-Bradley R, Mooney S, Tams A, Ennos A (2004) Understanding and reducing lodging in cereals. *Advances in Agronomy* 84(04):215-269.

149. Bashford L, Maranville J, Weeks S, Campbell R (1976) Mechanical properties affecting lodging of sorghum. *Transactions of the ASAE* 19(5):962-966.

150. Flint-Garcia SA, Jampatong C, Darrah LL, McMullen MD (2003b) Quantitative trait locus analysis of stalk strength in four maize populations. *Crop Science* 43(1):13-22.

151. Hu H, Liu W, Fu Z, Homann L, Technow F, Wang H, Song C, Li S, Melchinger AE, Chen S (2013) QTL mapping of stalk bending strength in a recombinant inbred line maize population. *Theoretical Applied Genetics* 126(9):2257-2266.

152. Li K, Yan J, Li J, Yang X (2014) Genetic architecture of rind penetrometer resistance in two maize recombinant inbred line populations. *BMC Plant Biology* 14(1):152.

153. Mullet J, Morishige D, McCormick R, Truong S, Hilley J, McKinley B, Anderson R, Olson SN, Rooney W (2014) Energy sorghum—a genetic model for the design of C4 grass bioenergy crops. *Journal of Experimental Botany* 65(13):3479-3489.

154. Pedersen JF, Toy J (1999) Measurement of sorghum stalk strength using the Missouri-Modified Electronic Rind Penetrometer. *Maydica* 44:155-158.

155. Peiffer JA, Flint-Garcia SA, De Leon N, McMullen MD, Kaeppler SM, Buckler ES (2013) The genetic architecture of maize stalk strength. *Plos One* 8(6):e67066.

156. Robertson D, Smith S, Gardunia B, Cook D (2014) An improved method for accurate phenotyping of corn stalk strength. *Crop Science* 54(5):2038-2044.

157. Zuber M, Grogan C (1961) A New Technique for Measuring Stalk Strength in Corn 1. *Crop Science* 1(5):378-380.

158. Robertson DJ, Julias M, Gardunia BW, Barten T, Cook DD (2015a) Corn stalk lodging: a forensic engineering approach provides insights into failure patterns and mechanisms. *Crop Science* 55(6):2833-2841.

159. Robertson DJ, Smith SL, Cook DD (2015b) On measuring the bending strength of septate grass stems. *American Journal of Botany* 102(1):5-11.

160. Dillon SL, Shapter FM, Henry RJ, Cordeiro G, Izquierdo L, Lee LS (2007) Domestication to crop improvement: genetic resources for Sorghum and S accharum (Andropogoneae). *Annals of Botany* 100(5):975-989.

161. Doggett H (1988) Sorghum. *Harlow, Essex, England New York: Longman Scientific & Technical. Wiley* 18:512

162. Doggett H, Majisu B (1968) Disruptive selection in crop development. *Heredity* 23(1):1.

163. Harlan J, De Wet J (1972) A Simplified Classification of Cultivated Sorghum 1. *Crop Science* 12(2):172-176.

164. Flint-Garcia SA, Darrah LL, McMullen MD, Hibbard BE (2003a) Phenotypic versus marker-assisted selection for stalk strength and second-generation European corn borer resistance in maize. *Theoretical Applied Genetics* 107(7):1331-1336.

165. Niklas KJ (1992) *Plant Biomechanics: an Engineering Approach to Plant Form and Function* (University of Chicago press).

166. Pinthus MJ (1973) Estimate of genotypic value: A proposed method. *Euphytica* 22(1):121-123.

167. Gardiner B, Berry P, Moulia B (2016) Wind impacts on plant growth, mechanics and damage. *Plant Science* 245:94-118.

168. Speck T, Burgert I (2011) Plant stems: functional design and mechanics. *Annual Review of Materials Research* 41:169-193.

169. Gomez FE, Carvalho G, Shi F, Muliana AH, Rooney WL (2018) High throughput phenotyping of morpho-anatomical stem properties using X-ray computed tomography in sorghum. *Plant Methods* 14(1):59.

170. Gomez FE, Muliana AH, Niklas KJ, Rooney WL (2017) Identifying morphological and mechanical traits associated with stem lodging in bioenergy sorghum (Sorghum bicolor). *BioEnergy Research* 10(3):635-647.

171. Gomez FE, Muliana AH, Rooney WL (2018) Predicting stem strength in diverse bioenergy sorghum genotypes. *Crop Science* 58(2):739-751.

172. Berry P, Sylvester-Bradley R, Berry S (2007) Ideotype design for lodging-resistant wheat. *Euphytica* 154(1-2):165-179.

173. Kashiwagi T, Togawa E, Hirotsu N, Ishimaru K (2008) Improvement of lodging resistance with QTLs for stem diameter in rice (Oryza sativa L.). *Theoretical and Applied Genetics* 117(5):749-757.

174. Li M, Yan G, Bhalla A, Maldonado-Pereira L, Russell PR, Ding S-Y, Mullet JE, Hodge DB, products (2018) Physical fractionation of sweet sorghum and forage/energy sorghum for optimal processing in a biorefinery. *Industrial Crops* 124:607-616.

175. Chattopadhyay P, Pandey K (1999) Mechanical properties of sorghum stalk in relation to quasi-static deformation. *Journal of Agricultural Engineering Research* 73(2):199-206.

176. Brüchert F, Speck O, Spatz HC (2003) Oscillations of plants' stems and their damping: theory and experimentation. *Philosophical Transactions of the Royal Society of London. Series B: Biological Sciences* 358(1437):1487-1492.

177. Hansen SL, Ray PM, Karlsson AO, Jørgensen B, Borkhardt B, Petersen BL, Ulvskov P (2011) Mechanical properties of plant cell walls probed by relaxation spectra. *Plant Physiology* 155(1):246-258.

178. Hayot CM, Forouzesh E, Goel A, Avramova Z, Turner JA (2012) Viscoelastic properties of cell walls of single living plant cells determined by dynamic nanoindentation. *Journal of Experimental Botany* 63(7):2525-2540.

179. Spatz H, Kohler L, Niklas K (1999) Mechanical behaviour of plant tissues: composite materials or structures? *Journal of Experimental Biology* 202(23):3269-3272.

180. Wright CT, Pryfogle PA, Stevens NA, Steffler ED, Hess JR, Ulrich TH (2005) Biomechanics of wheat/barley straw and corn stover. *Applied Biochemistry and Biotechnology* 121(1-3):5-19.